Synthesis of copper oxide electrocatalysts for the conversion of CO2.

Fábio Ferreira Vieira

THESIS

UNIVERSITE DE PAU ET DES PAYS DE L'ADOUR

École doctorale sciences exactes et leurs applications

Présentée et soutenue le (date)

par **Fábio VIEIRA**

pour obtenir le grade de docteur
de l'Université de Pau et des Pays de l'Adour
Spécialité : Chimie

Synthesis of copper oxyde electrocatalysts for the conversion of CO_2

MEMBRES DU JURY

RAPPORTEURS

• Dr. Elena MAS MARZA	Associate Professor / INAM-Universitat Jaume I
• Dr. Pau FARRAS	Lecturer Above the Bar / NUIG

EXAMINATEURS

• Dr. Victor MOUGEL	Assistant Professor / ETH Zürich
• Dr. Aurelien VITERISI	Research Associate / IPREM-UPPA

DIRECTEURS

• Dr. Laurent BILLON	Professor / IPREM-UPPA
• Dr. Emilio PALOMARES	Professor / ICIQ-URV

UNIVERSITÉ DE PAU ET DES PAYS DE L'ADOUR

Acknowledgments

I would like to first and foremost express my gratitude to my thesis supervisors, Dr. Laurent Billon and Dr. Emilio Palomares for their help and guidance during the PhD, without which I would not have achieved nearly as much. I am also thankful for the help of Dr. Julio Lloret for opening his lab for me when I still did not a functional one.

Throughout the PhD, I had the greatest pleasure and I am very proud of helping start and being a part of a group like InterMat alongside Dr. Aurelien Viterisi and my fellow PhD colleague Léonard Curet. They were a integral part of this work and without their assistance I would have been lost many times. Dr. Aurelien Viterisi did an outstanding job as a lab technician, scientific advisor/writer and helped me at every step of the project. Léonard was a great mind to bounce ideas with and a beacon of friendship which was fundamental in keeping my stress at bay. I hope they as a group continue strong after my absence and continue to grow as a scientific group.

Thanks to the many people at IPREM which helped me throughout the PhD as research and/or technical staff, their hard work was very appreciated. Special thanks to Dr. Pierre Marcasuzaa, who was always available to help with polymer synthesis and characterization, a subject which was completely new to me. My gratitude for everybody that took time from their schedules to teach and support me with the use of analytical equipment. I am also thankful for all the PhDs around me for being friendly and for being open to help and being helped, creating a cooperative environment in the labs. A big thank you also to everybody in Palomares group in Tarragona for the warm reception and acceptance during my short stay with them. And of course, a big thank you to Dr. Geyla Carydad for teaching everything I needed to know to work on Dr. Julio Lloret's lab.

I can never be thankful enough to all my friends which supported be from day one of this crazy adventure. Being away from home for the first time, even more so during a global pandemic, I could not have survived without the multiple video calls, the long hours gaming sessions and the start of the tradition of trying to watch a

movie together every weekend. In special, I have an enormous debt of gratitude to Débora and Chapa who truly became a second family for me.

And last but not least, an enormous thank you to my family, who always supported and encouraged me to follow my dreams.

Table of Contents

List of figures

Abstract

In this work, a convenient method for preparing cupric and cuprous oxide thin films from a common sol-gel approach is described. The method consists in depositing a thin film of a copper nitrate precursor embedded in a hydroxypropyl cellulose matrix followed by calcination at 500°C. It was found that cupric oxide (CuO) thin films were produced if the calcination step was carried in air, while cuprous oxide (Cu_2O) thin films were predominantly produced if the calcination was carried under a constant-flow rate nitrogen stream. Interestingly, the Cu_2O films were shown to be doped with carbon and nitrogen atoms, with the dopant concentration being related to the nitrogen flow rate used during the calcination step. Importantly, the doping induces a decrease in band gap to lower values than the 2.2 eV benchmark for intrinsic Cu_2O. The conductive properties of the doped Cu_2O remained in line with literature values as long as doping was kept minimal. The deposition method of such films is compatible with conductive transparent oxide for application to photo-electroreduction of CO_2. These thins films were shown to be unstable in electrocatalytic conditions, so a mesoporous gas diffusion polymeric membrane was design to serve as a stabilizing layer. This membrane was self-assembled in to a porous "honeycomb" shape utilizing the breath figure method and is made of a copolymer blend of polymethylmethacrylate (PMMA) and poly-4-vinylpyridine (P4VP) in a ratio of 80:20 between the two polymers. The P4VP present on the polymer grants hydrophobicity to the membrane when unprotonated and hydrophilicity when protonated. With this membrane, not only we stabilised our thin film electrodes but also shifted the selectivity towards carbon monoxide (~80%) and supress the hydrogen evolution reaction (HER). This copolymer was further tested as a surface modifier by being applied as a mesoporous membrane and as a thin film to known copper and silver foils electrodes, causing greater hydrogen suppression as a thin film and greatly increasing the production of C_{2+} products in copper foil, with a selectivity change towards ethylene.

Résumé

Dans cette thèse, une méthode pratique pour préparer des films minces d'oxyde cuivrique et cuivreux à partir d'une approche sol-gel est décrite. Le procédé consiste à déposer un film mince d'un précurseur de nitrate de cuivre incorporé dans une matrice d'hydroxypropylcellulose suivi d'une calcination à 500°C. Il a été constaté que la composition des couches minces était principalement d'origine cuivrique si l'étape de calcination était effectuée dans l'air, tandis que des couches minces étaient principalement d'origine cuivreux (Cu_2O) si la calcination était effectuée sous un flux d'azote à débit constant. Fait intéressant, il a été démontré que les films de Cu_2O étaient dopés avec des atomes de carbone et d'azote, la concentration de dopant étant liée au débit d'azote utilisé pendant l'étape de calcination. Il est important de noter que le dopage induit une diminution de l'énergie de bande interdite, "band gap", à des valeurs inférieures à la littérature de 2,2 eV pour le Cu_2O intrinsèque. L'impact du dopage sur les propriétés conductrices des couches de Cu_2O) est peu significatif. La résistivité des films reste similaire aux valeurs reportées dans la littérature tant que le dopage est léger. La méthode de dépôt de tels films est compatible avec certains oxydes transparents conducteurs, particulièrement l'oxide d'étain dope a l'indium (ITO) pour application à la photo-électroréduction du CO_2. Ces films minces se sont révélés instables dans des conditions électrocatalytiques, de sorte qu'une membrane polymère mésoporeuse de diffusion de gaz a été conçue pour servir de couche stabilisatrice. Cette membrane a été auto-assemblée en une forme poreuse en "honeycomb" en utilisant le "Breath Figure method" et est faite d'un mélange de copolymères de polyméthacrylate de méthyle (PMMA) et de poly-4-vinylpyridine (P4VP) dans un rapport de 80:20 entre les deux polymères. Le P4VP présent sur le polymère accorde de l'hydrophobicité à la membrane lorsqu'elle n'est pas protonée et de l'hydrophilie lorsqu'elle est protonée. Avec cette membrane, nous avons non seulement stabilisé nos électrodes à couche mince, mais nous avons également déplacé la sélectivité vers le monoxyde de carbone (~80%) et supprimé la réaction de dégagement de l'hydrogène (HER). Ce copolymère a ensuite été testé comme modificateur de surface en étant appliqué comme membrane mésoporeuse et comme film mince sur des électrodes connues de feuilles de cuivre et d'argent, provoquant une plus grande suppression de

l'hydrogène en tant que film mince et augmentant considérablement la production de produits C_{2+} dans les feuilles de cuivre, avec un changement de sélectivité vers l'éthylène.

Motivation

The continuous use of fossil fuels is causing rampant emissions of greenhouse gases to the atmosphere, threatening earth's ecosystems by changing the global climate. Whilst clean fuel alternatives such as solar, wind and hydro are being studied, the atmosphere contains serious concentration levels of greenhouse gases. Amongst these gases, the biggest issue is carbon dioxide (CO_2).

In order to reduce the levels of CO_2 in the atmosphere, there are several possible pathways:

- The use of clean energy, such as solar, wind or nuclear instead of depending on the burning of fossil fuels;
- The development of CO_2 capture technologies to capture it from the atmosphere or in factory chimneys;
- Converting CO_2 to other value added chemicals, that can then be used as fuels or as feedstock for the chemical industry.

This work focus on the understanding of CO_2 electroreduction and the creation of a simple, low cost and scalable electrode easily fabricated at an industrial scale. Such an electrode can be fabricated and implemented quickly and would be a great asset in the fight against global warming.

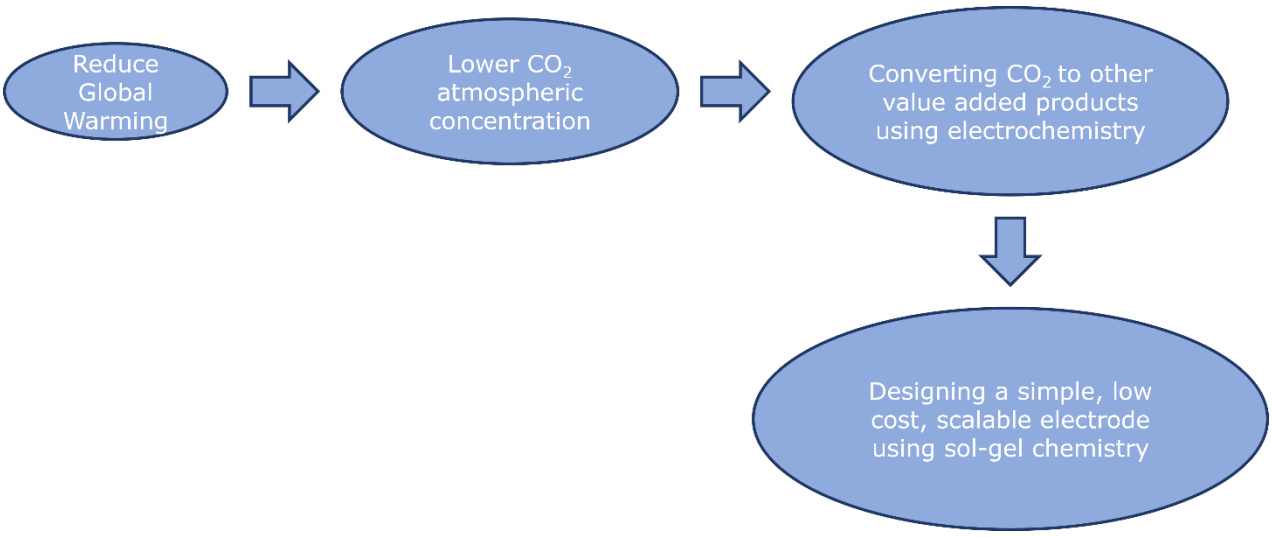

Figure I. *Diagram representing the motivation behind the work.*

List of acronyms and chemical formulas

AFM	Atomic force microscopy
AES	Auger electron spectroscopy
C_1	Single carbon products
C_{2+}	Multiple carbon products
CA	Chronoamperometry
CO2RR	CO_2 reduction reaction
CV	Cyclic voltammetry
DCM	Dichloromethane
DMF	Dimethylformamide
e^-	Electron
Eg	Band gap
ETPT	Electron transfer and proton transfer
FE	Faradaic efficiency
GC-MS	Gas chromatographer and mass spectrometer
h	Planck's constant
HER	Hydrogen evolution reaction
J	Current Density
LSV	Linear sweep voltammetry
NMR	Nuclear magnetic resonance
P4VP	Poly (4-vinylpyridine)
PCET	Proton-coupled electron transfer
PEC	Photoelectrochemical

PMMA	Poly (methyl methacrylate)
PTET	Proton transfer and electron transfer
SEC	Size exclusion chromatography
SEM	Scanning electron microscopy
UV	Ultraviolet
XPS	X-ray photoelectron spectroscopy
XRD	X-ray diffraction
α	Absorption coefficient
η	Overpotential
ν	Frequency (Hz)

1 - Introduction

The current energy situation has been, for several years now, a source of constant and growing discussions, conflicts, questions and concerns. A question that arises is "how to meet a growing energy demand, while limiting the environmental impact of the production and use of this energy, without reducing our standard of living (or even improving that of the inhabitants of developing countries)?" and the scientific community could help with the answer.

The continuous use of fossil fuels is causing rampant emissions of greenhouse gases to the atmosphere, threatening earth's ecosystems by changing the global climate. Stopping this change and stabilizing the climate is critical for the future of humanity, as Rockström et al. already alerted for in 2009[1]. Whilst clean fuel alternatives such as solar, wind and hydro are being studied, these technologies suffer from issues of intermittency and baseload power[2] and, in the meantime, the atmosphere has still serious concentration levels of greenhouse gases, being carbon dioxide (CO_2) a large part of it, as seen in Figure 1-1[2]. This is a matter of great concern as CO_2 emissions have continuously increased over the last century and nowadays are reaching unsustainable levels[3].

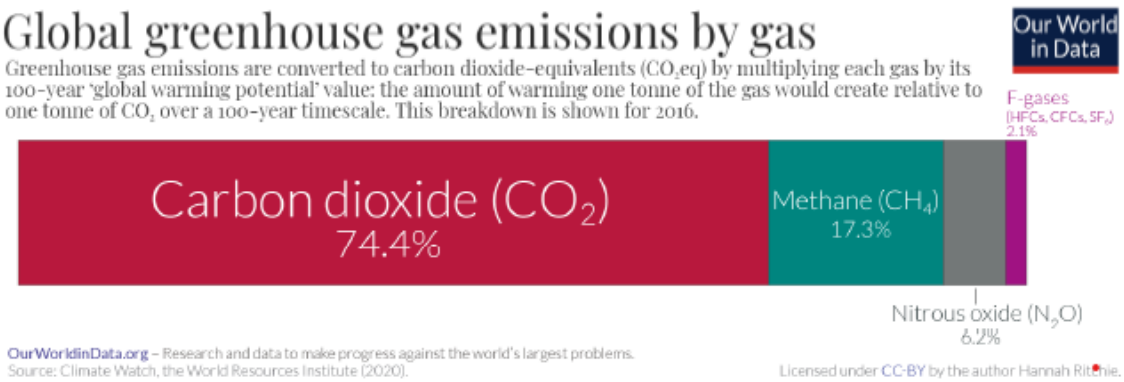

***Figure 1-1**. Share of gases involve in greenhouse emissions. From Climate Watch, the World Resources Institute (2016).*

Therefore, a swift conversion from a carbon-intense society to a carbon-free society is a must. To achieve such as goal, a series of social and regulatory changes need to occur simultaneously with large technological improvements. One of those technological improvements could be artificial photosynthesis. Artificial

photosynthesis is a man-made attempt at replicating the natural process of the same name, entailing the harvest of solar energy and the application of that energy in the electrochemical catalysis of CO_2 to value added hydrocarbons in an aqueous medium. Moreover, these hydrocarbons being formed from CO_2 would be the equal to the ones manufactured from fossil fuels, an overhaul of the storage and transport infrastructure would not be necessary. Concluding, artificial photosynthesis produces clean fuels while reducing the atmospheric concentration of greenhouse gases, becoming a very attractive technology for the future, making extensive research necessary to understand this technology and adapt it to everyday life[4–6].

Through the work described in this manuscript, we will seek to find a simple and low-cost synthesis of copper oxide-based electrodes for the electro- and photoelectroreduction of CO_2. First, after an introduction to the topic and an overview of the methodologies used in this work, the synthesis of CuO and Cu_2O thin films via blade coating and annealing techniques for the electroreduction of CO_2 is presented. Thereafter, a mesoporous hydrophobic membrane acting as a protecting and selectivity changing layer for the electrode is analysed. Lastly, an overall evaluation of the work is provided and the future uses of this technology is discussed.

1.1 (Photo)Electrocatalysis

A catalyst is a material that intervenes in a chemical reaction and changes the reaction rate without being chemically changed or consumed. Electrocatalysts, in particular, are catalysts that enhanced the rate of electrochemical reactions occurring on its surface. They are classified in two categories: homogenous, when catalyst and reactants share the same phase, and heterogeneous, when catalyst and reactant are in distinct phases, making the reaction take place in the interface between the two. The electrocatalytic reactions manage the interaction amongst chemical change and electrical energy. Electrochemical reactions are always divided in two half reactions, one at the anode where a species donates electrons and oxidizes and one at the cathode where a species accepts electrons and reduces [4,7].

An electrocatalyst behaviour towards certain reactions is influenced by a myriad of parameters, such as surface roughness, electrode morphology, adsorption sites, pH of the solution, oxidation state, etc. Figuring out how all of these parameters affect the reaction is therefore a very important step in order to create an effective and efficient catalyst[7–10].

Photocatalysis of CO_2 reduction to liquid fuels is a fundamental aspect of artificial photosynthesis, making the harvest of solar energy part of the same process as the catalysis of the molecule. Photocatalysis is analogous to electrocatalysis, with the variance that while in electrocatalysis the reaction is driven by applying a voltage bias between the cathode and the anode, in photocatalysis a semiconducting photocathode drives the chemical reaction by generating electron-holes pairs when expose to light[7,10–12]. For heterogeneous photocatalysis, the usual catalysts are semiconductors and transition metal oxides which, unlike metals that possess continuous electronic states, have a disparity between the energy levels of the valence band and the energy levels of the conduction band. This disparity in energy is known has bandgap and for an electron to pass from the valence band to the conduction band the bandgap has to be overcome via the absorption of incident high-energy photons with energy larger than the band gap. These excited electrons in the conduction band are then able to migrate to the surface and take part in reduction reactions[7,13].

A photoelectrochemical (PEC) catalytic system integrates both photo and electroreduction, allowing the use of external voltage that optimizes the migration and aggregation of the photogenerated electron-hole pairs, suppressing their recombination rate [5,7,10–16].

1.2 CO_2 Electrocatalysis

CO_2 is a highly stable molecule and is usually inert in most conditions[7,9,17]. Yet, by applying a potential difference between two electrodes in a device known as electrolyzer, water oxidation occurs at the anode releasing protons and electrons that are consumed in the cathode, resulting in the reduction of CO_2 through the CO_2 reduction reaction (CO2RR) to different products, as shown below[7].

- $CO_2 + 2H^+ + 2e^- \rightarrow CO + H_2O$ E° = -0.10 V vs. RHE
- $CO_2 + 2H^+ + 2e^- \rightarrow HCO_2H$ E° = -0.20 V vs. RHE
- $CO_2 + 4H^+ + 4e^- \rightarrow H_2CO + H_2O$ E° = -0.07 V vs. RHE
- $CO_2 + 6H^+ + 6e^- \rightarrow CH_3OH + H_2O$ E° = 0.02 V vs. RHE
- $CO_2 + 8H^+ + 8e^- \rightarrow CH_4 + 2H_2O$ E° = 0.17 V vs. RHE
- $2CO_2 + 12H^+ + 12e^- \rightarrow CH_3CH_2OH + 3H_2O$ E° = 0.09 V vs. RHE
- $2CO_2 + 12H^+ + 12e^- \rightarrow C_2H_4 + 4H_2O$ E° = 0.08 V vs. RHE

While at the anode water is being oxidize to produce protons and oxygen:

- $2H_2O \rightarrow O_2 + 4H^+ + 4e^-$

The electron and proton can be transferred to the same acceptor or can go to two distinct ones and the transfer can occur in one or two successive steps, with the help of a reaction intermediate. When we have a two steps transfers, the mechanism is denoted as sequential. There are two types of sequential mechanism: electron then proton transfer (ETPT) or proton then electron transfer (PTET). When the two transfers occur simultaneously the mechanism is known as coupled and the reaction is known as proton-coupled electron transfer (PCET)[7]. In Figure 1-2 all this transfer mechanisms are on display.

***Figure 1-2**. Diagram of the three possible pathways for a electron-proton transfer, with the PTEP pathway in purple, the ETPT pathway in orange and the PCET pathway in red.*

From a thermodynamic point of view, reactions involving the transfer of several electrons and protons are more favourable (i.e. occur at less negative potentials). In contrast, the transfer of a large number of these particles is unfavourable from a kinetics point of view [7,18,19], and may actually turn out to be limiting. In a homogeneous medium, a reaction is described as having a low kinetic constant. This signifies that if the reaction takes place at one electrode, when we

apply a potential that is equal to the standard potential of the reaction we would observe a current density of zero. This is due to the fact that the reaction includes intermediary steps or transition states that are highly energetic and involve significant geometry changes, despite the reaction as a whole being thermodynamically "more favourable" than the single-electron reduction. Henceforth, to conduct the reaction the applied potential has to be higher (in absolute value) than the standard potential of the reaction. This excess potential is known as overpotential, η[8–10,12,19].

Let's now consider using a catalyst for the reaction. The catalyst does not have an impact on the balance equation and, thus, the equilibrium constant is left unchanged. However, it influences the kinetics of the reaction by stabilizing transition states, coordinating CO_2 and helping geometry changes, which in turn causes a drop on overpotential and makes the reaction more energetically efficient. Therefore, the catalyst choice is crucial for CO_2 electroreduction.

1.3 Choosing a catalyst

A variety of electrocatalysts for the CO2RR have been discovered, each producing distinct reduction products[20–24]. Transition metals are frequently utilised in CO2RR and are grouped according to their product selectivity. The selectivity is primarily determined by the initial method in which CO_2 is reduced on the metal surface[25–27]. The initial method of CO_2 reduction on the metal surface is the primary factor that determines selectivity. The first group contains metals that selectively form formic acid, such as Hg, Pb, In and Sn. These metals facilitate the formation of formic acid since they show very poor binding with both hydrogen and CO, making the intermediates having a weak adsorption on the surface and, consequently, causing them to be unable to break the C-O bond of the CO_2, facilitating the formation of formic acid.

The second group pertains to the CO-producing metals, with Au, Ag and Zn as the major metals. These metals are selective for CO_2 conversion to CO due to their weak binding energies for CO, which prevents the further reduction of the CO to hydrocarbons, aldehydes and alcohols. Hansel et al.[28] proposed a model that

proposes how the binding energies of the reaction intermediates can be used to describe the trends in catalytic activity. Using this model, considering that the pathway for CO is through the adsorbed intermediates *COOH and *CO, we see that these metals are able to stabilize *COOH in their surface without overstabilizing *CO.

In the third group metals such as Pd, Ni, Pt, Ti Rh, Ir, Fe and Ru, capable of reducing H_2 at low potentials. The high selectivity towards H_2 is due to the very high bonding energy that these metals have, which results in reduction of CO_2 to CO on their surface and the subsequent poisoning of the surface with the newly formed CO, that blocks further reductions and makes the H_2 the main product of the reaction.

Outside of these groups, Cu is a unique metal. Since Hori's work in 1989 and 1994[29,30], copper (Cu) became a very attractive material for electrodes. Cu is the only metal capable of reaching complex reduction products, as hydrocarbons and alcohols while maintaining satisfactory activity and efficiency during the reaction[30–32]. Jaramillo et al.[33] has observed the production of 16 distinct products: besides the common ones such as CO, methane, ethylene, formate, ethanol and propanol, minor products as allyl alcohol, acetaldehyde, propionaldehyde, methanol, glycolaldehyde, ethylene glycol, acetone, acetate and hydroxy acetone were also detected with low efficiencies, as shown in Figure 1-3. Cu has these capabilities due, in part, to the suitable binding energy to both *H and *CO, resulting in sufficient resident time for the *CO intermediate to couple with other nearby intermediates, leading to the further dimerization or protonation of *CO to produce hydrocarbons and alcohols. Although this binding with *H is crucial in the protonation of the intermediates, it also makes the suppression of H_2 evolution in monometallic Cu extremely difficult. Nevertheless, Cu's ability to form complex CO_2 reduction products has brought forth an academic effort to fully understand it[34–39]. Various experimental and theoretical studies have proposed mechanisms for Cu's catalytic performance for CO_2 reduction. Yet, a comprehensive mechanism is still under great discussion[9,35,40–42]. For instance, Literature describes that ethylene and methanol follow two distinct pathways[43] while both having CO has the key intermediate in the reaction[29–31]. The production of ethylene was found to be pH independent, inferring that the rate-determining step does not involve a proton transfer[29,31,44]. Yet, since the reaction shows dependency on potential, an electron transfer must be occurring. A C-C coupling of two adsorbed CO molecules through a reductive dimerization has been suggested as the rate-

determining step for the reaction conversion into valuable molecules has emerged as a field of intensive investigation, with the aim of ultimately developing scalable technologies for making fuels using renewable sources of energy[40,41]. Contrastingly, on the case of methane production, pH has been found to be a factor, implying that a proton and electron transfer must occur in the rate-determining step[31,44]. The pathway for this reaction was suggested by Hori, which put forward that the methane formation is due to adsorbed COH[31]. This example shows that, although in a first view two reaction have the same key intermediate, with a more in-depth analysis we see that the reaction mechanisms for both are distinct.

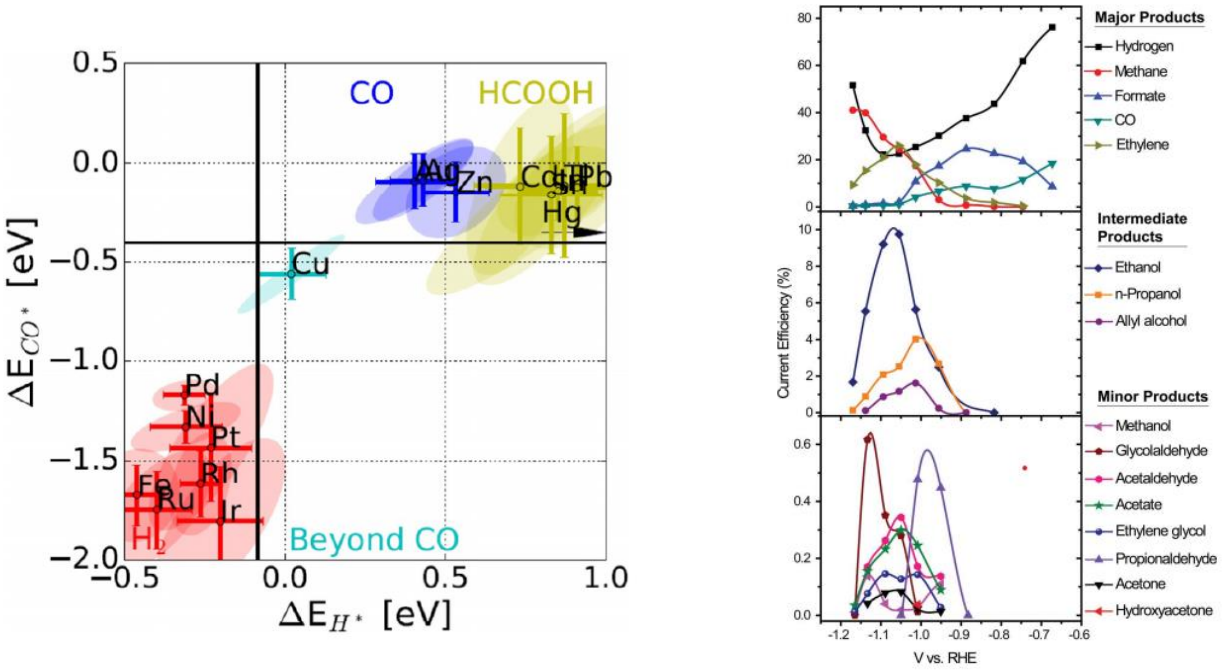

***Figure 1-3**.-Binding energies of the intermediates (H* and CO*) for different metal catalysts (left). Reproduced from Bagger et al.[22]. Current efficiency in function of potential for each reaction product of a copper catalyst. Reproduced from Jaramillo et al.[33].*

1.4 Copper, a very prolific catalyst

Copper has been popular since thousands of years ago. At first, it was alluring due to the ability to use its metallic form directly, without requiring extraction from an ore. Copper is also an element that is in high abundance in the surface of the earth's crust, making it easy to mine and very inexpensive. Other metals, like Au, cost more than 10000 times the cost of copper. This high abundance and low price

gives copper a very attractive aura, generating interest on its use in many scientific fields. One of those fields with a big interest in copper is the electrochemical, that has been using copper as a catalyst for electrochemical reduction of gases, mainly CO_2[45]. In the last decade, copper catalysts in many forms (metallic, bimetallic, oxide-derived) have shown great catalytic performance in a diverse range of selectivity [7,9,12,16–18,20,25–27,31,36,41,46–50]. This selectivity range can be explained in diverse manners, as experimental conditions or material specific conditions, like synthesis of the material, dimensional structure, surface roughness and the oxidation state of the Cu all have an impact in the final products of catalysis. Consequently, all these results need to be compared under certain experimental conditions to be able to determine which factors truly influence the Cu-based electrodes selectivity[27].

1.5 Single metal-phase copper

Looking back at the previous section, we noted that single metal-phase copper differs from other elemental metals in the catalytic products. As other metals such as Ag, Au, Ni, Zn, etc. mostly form hydrogen, carbon monoxide, formic acid and other two electron transfer products in normal electrocatalytic conditions, metallic Cu has shown his ability to produce more complex products, like hydrocarbons, due to its surface having a suitable CO* adsorption energy[24]. Consequently, single metal-phase copper is of great interest to be used as catalyst. However, its poor selectivity towards a single product becomes a huge hurdle to overcome. To better understand the behaviour of the single metal-phase copper we will take a look at nanostructures.

One of the most common strategies to improve the activity of an electrocatalyst is changing its morphology. There are various nanostructures of interest separated by their dimensions, there is zero-dimensional (0D), one-dimensional (1D), two-dimensional (2D) and three-dimensional nanostructures (3D)[26,51,52]. The variation of dimensions of the catalyst has been shown to greatly impact the catalytic process, with Loiudice et al.[53] studying copper nanocrystals with sizes of 24, 44 and 63 nm. They found that the electrode with 44 nm exhibits the best CO_2 reduction activity and has more selectivity towards products with two or more carbon atoms (C_{2+}). Many other such studies have been performed in recent

years[26,27,54–56]. However, this approach doesn't come without its own drawback, which is a reduction of the overall overpotential for the CO_2 electroreduction[18,26,41,57].

Another strategy that is currently under study in the electrocatalytic community is phase engineering. By controlling the crystalline structure of the copper, changes in the catalytic activity of the materials are detected[7,26,58,59]. In 2011, Durant et al[60] applied DFT calculations to determine that Cu(211) has lower theoretical overpotential for the reduction of CO_2 to methane and carbon monoxide than Cu(100). Thus, it seems that undercoordinated sites perform better for this reaction. Continuing in DFT calculations, Liu et al.[61] have calculated the barriers between intermediates for CO reduction, adding microkinetic calculations for the reaction rate. They chose CO instead of CO_2 due to CO being a key intermediate in CO_2 reduction to complex products. According to these calculations, Cu(211) presents an activity several orders of magnitude higher than that of Cu(100), which in turn presents an activity several orders higher than Cu(111). Nevertheless, when comparing these calculations with experimental data a disparity between the two appear. Hori et al.[62,63] used a series of Cu single crystals to reduce CO_2, only observing a difference in activity between Cu(111) and Cu(100) and little to no difference between Cu(100) and many other different facets. Hahn et al.[64] also compared the activity of Cu(111), Cu(100) and Cu(751) and the activity of the three were similar. A possible explanation for the disparity between theory and experimental data could be the quality of the electrodes used experimentally. Even though single crystals are accurately cut to represent a chosen surface orientation. Some degree of imperfection is unavoidable[65,66]. Even if experimentally there is no significant difference between planar and stepped surfaces, we can draw some deductions about product distribution. Oxygenates seem to be connected to many of the stepped surfaces while certain orientations show suppression of single carbon products (C_1) and higher selectivity for C_{2+}[62–64].

1.6 Cu-based catalysts

We just saw that metallic Cu, despite its uniqueness regarding other metals, still have a lot of drawbacks to overcome. It has the ability to further reduce CO_2 past HCOO and CO but does so with high overpotential and very poor selectivity.

Two other key strategies to improve the activity of Cu are the use of bimetallic alloys and the use of oxide-derived Cu catalysts.

1.6.1 Bimetallic Cu catalysts

When other guest elements are added to a copper catalyst, it can have a significant impact on the electronic structure of the material. This is a concept that has been proposed through theoretical analysis of the d-band center. This analysis suggests that these changes in the electronic structure can lead to variations in the binding strength of intermediates that are adsorbed on the surface of the catalyst[20,25,26,67–71]. This means that the chemical reactions taking place on the surface of the catalyst can be affected by the presence of these guest elements, and can result in different outcomes. Overall, it is important to consider the potential effects of incorporating additional elements into a copper catalyst when developing or optimizing catalytic processes. Copper-based bimetallic catalysts are then of great interest, as the combinations between Cu and different elements can greatly influence the catalytic activity via modification of the structure of the catalyst, the existence of different active sites active for distinct intermediates and causing a strain effect on the Cu[17,20,25,26].

Combining Cu with a metal that mostly produces H_2, like Pd, Pt, Fe or Ni, seems to facilitate the protonation process, boosting the reduction of CO to CH_4 and of C_2H_4 to C_2H_6. The combination of Cu with this group of metals also affect the catalytic performance positively[25,26,72,73].

Combining Cu and formate-producing metals, such as In and Sn, results in a bimetallic catalyst with selectivity towards CO and $HCOO^-$, suppressing both the hydrogen evolution and the formation of products requiring more than a 2 electron transfer[25,26,52,74,75].

Combining Cu with metals specialised in CO, as Au, Ag and Zn, show mostly enhanced CO production when compared to Cu alone. Nevertheless, with these bimetallic catalysts, activity towards C_{2+} products is also present[25,26,28,39,50,76,77].

To finish, with a few notable exceptions, most bimetallic materials cause an increase in selectivity towards H_2 or 2 electron transfer products, when directly

compared to copper. A better understanding of Cu electrodes is crucial in designing bimetallic catalysts for the formation of products involving more than two electron transfers[58,78–80].

1.6.2 Cu oxide catalysts

One of the most popular methods to improve the activity and selectivity of copper is by manipulating its oxidation state. Literature shows that the modification of oxidation states is extremely beneficial to the production of C_{2+} products[16,34,58,80–89]. The addition of oxygen atoms to a copper catalyst can have a notable impact on its electronic structure and, as a result, enhance its catalytic performance. This was first discovered by Hori et al.[31], who found that copper oxide materials have a larger surface area than pure copper. They proposed that the removal of oxygen molecules during the catalytic reduction of CO_2 creates a porous and inhomogeneous structure on the surface of the electrode, which is responsible for the improvement in catalytic activity. As more research has been conducted on copper and its oxides, it has been revealed that this rough topographic surface can also lead to an increase in defect density and pH changes on the surface. Additionally, the formation of low-coordination edges, steps, and active grain boundaries has been observed, further contributing to the enhancement of catalytic performance[34,90].

The synthesis of these electrodes also has a critical impact on their performance. The electrodes grown from anodically oxidised foils and Cu_2O films show better selectivity towards C_{2+}. Contrarily, the bulk of the studies on copper oxide grown by annealing reveal very little C_{2+} formation[91]. This behaviour can be explained by the different electrochemical surface areas of the electrodes synthesised by the two methodologies. Due to the low solubility of CO_2 in water, CO_2 reduction in aqueous electrolytes is extremely dependent on the mass transport of CO_2 to the catalyst surface[7]. This means that materials with higher electrochemical surface areas are more limited by the CO_2 mass transport than planar catalysts, because the CO_2 is depleted faster due to the higher activity per geometric surface area. As annealed copper oxides show generally more roughness at their surface, they will reach mass transport limitations faster, shifting their selectivity towards H_2 due to the scarcity of CO_2, explaining their low selectivity towards C_{2+} products.

1.7 Surface Modification

Whilst these copper oxide catalysts show great performance in terms of activity and selectivity, their stability under electrochemical conditions is a cause of concern and their controlled synthesis remains an issue to this day[92]. The use of polymeric protective layers on top of the catalyst surface is a possible solution for the stability issue and, at the same time, improving the selectivity and catalytic performance of the catalyst by using hydrophobicity to supress the hydrogen evolution reaction (HER)[93–103].

Surface modification plays a crucial role in adjusting the electronic structure of metal atoms on the surface of materials, resulting in changes in the adsorption and desorption energies of CO2RR intermediates. This, in turn, can significantly enhance catalytic performance, including catalytic activity, selectivity, and stability. Therefore, rational surface modification strategies can be employed to improve the overall catalytic performance of both homo and heterogeneous catalysts for CO_2 reduction reactions[94,99,100,104–122]. For example, Wakerley et al.[103] have shown how controlling the hydrophobicity of the catalyst leads to a drastic increase in selectivity towards CO2RR. They achieve these results by coating their dendritic copper electrode with long-chain alkanethiols, which have very high hydrophobicity. This coating results in a decrease of water/electrolyte reaching the active surface, causing more CO_2 concentration and thus, an increase on the activity towards CO_2 reduction.

Self-assembled polymers with a hydrophobic honeycomb structure, i.e. micron-sized porosity, are a new and exciting category of materials that have been gaining a lot of attention in recent years[123–132]. These materials are made up of (co)polymer chains that have the ability to spontaneously self-assemble into a unique honeycomb-like structure. Structural[133] and chemical[124] bio-inspired honeycomb films can be created by combination of the directed self-assembly of block copolymers in “breath figure” BF templating. The breath figure method is well known as a versatile and fast, i.e. less than a minute, self-assembly process to hierarchically structured film as synthetic bio-inspired diatom frustules[124].

The breath figure method involves applying a solution of polymer onto a substrate, such as a glass or silicon wafer. The substrate is then exposed to a humid environment, which causes water droplets to form on the surface of the polymer film. These water droplets act as a template for the formation of air-filled pores in the polymer film, resulting in a regular honeycomb-like structure.

This concept was developed to enhance the intrinsic hydrophobicity of polymer films. Indeed, by reducing the surface of film contact with water, a Cassie-Baxter regime appears, like a fakir effect, where the water droplet keeps on top of the film without wettability of the pores[131]. By using a pH sensitive block copolymer, a hydrophobic/hydrophilic transition can be addressed also called Cassie-Baxter/Wenzel transtion[131,133]. Thus, this transition allows the water droplet to wet through the film until the substrate as the pores are interconnected[134].

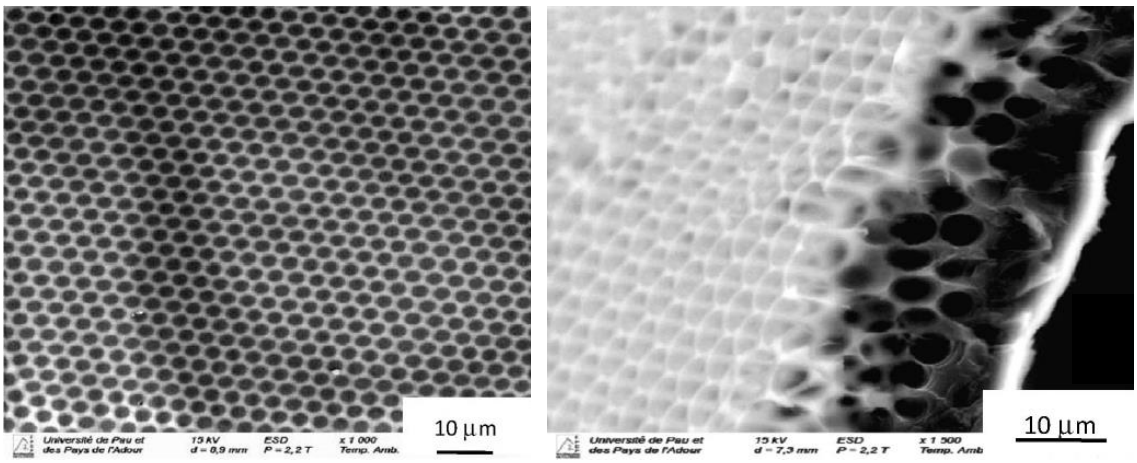

Figure 1-4. *SEM images of PolyStyrene PS film: top view (left) and cross-section (right). Reproduced from Billon et al.[134].*

Then, the hydrophobic/hydrophilic properties of the polymer film could be used to create a unique environment that can further trigger the efficiency and selectivity of catalytic reactions. Indeed, the hydrophobic nature of the film can help to exclude water and other polar molecules from the catalytic site, leading to improved selectivity and catalytic efficiency[94,96,100–102,111,135–137].

In this document, we will focus on the development of a stabilizing mesoporous hydrophobic polymeric membrane grown via the breath figure method[123–126] as a stabilizer for thin film CuO and Cu_2O catalysts on a transparent glass/ITO substrate for (photo)electrochemical applications.

2 - Experimental Techniques

This Chapter describes the experimental procedures and the characterisation techniques utilised for the synthesis and characterization of copper-based thin film electrodes for the electrochemical reduction of CO_2. First and foremost, the characterization techniques (optical, structural, electrical, etc) are briefly explained, followed by a description of all the synthetics methodologies which were performed during the PhD and finally the experimental setup for performing electrocatalysis is described.

2.1 Characterisation Techniques

2.1.1 Atomic force microscopy

Atomic force microscopy (AFM) is a high-resolution imaging technique that is used to obtain detailed images of surfaces at the atomic and molecular scales. AFM works by scanning a small probe across the surface of a sample, measuring the forces between the probe and the sample.

The probe used in AFM is typically a small cantilever with a sharp tip at one end. As the tip is scanned across the surface of the sample, it moves up and down in response to the forces between the tip and the atoms or molecules on the sample's surface. These movements are detected by a laser beam that is reflected off the back of the cantilever and onto a detector[138].

This technique can be used in various modes depending on the properties of the sample and the characterisation that the user wants. AFM can be used to measure the flatness/roughness of a surface, can be used to measure mechanical properties, such as the Young's modulus, can be used to see phase distribution of the sample or can measure electronic properties. This makes AFM a very versatile and useful characterization technique. We utilized AFM to analyse the phase distribution of a copolymer.

In this work, AFM characterization was achieved using a MultiMode 8 Atomic Force Microscope from Bruker.

2.1.2 UV-visible spectroscopy

UV-visible spectroscopy is a technique that is used to study the absorption of ultraviolet (UV) and visible light by molecules. It is based on the principle that molecules can absorb specific wavelengths of light, and that this absorption is characteristic of the particular molecule being studied.

In UV-visible spectroscopy, a sample is irradiated with a beam of UV or visible light, and the amount of light absorbed at each wavelength is measured. The resulting absorption spectrum is a plot of absorption (as a percentage of the incident light) versus wavelength[139].

There are two main types of UV-visible spectroscopy: absorption spectroscopy and transmission spectroscopy. In absorption spectroscopy, the light is passed through the sample and the amount of light absorbed is measured. In transmission spectroscopy, the light is transmitted through the sample and the amount of light transmitted is measured.

UV-visible spectroscopy is a widely used technique in many fields, including chemistry, biology, and material science. It is particularly useful for studying the electronic structure of molecules and for identifying unknown compounds. We used it for characterising the change in light absorption of copper oxide thin films prepared in different conditions.

The UV-Vis-NIR absorption spectra presented in this work were recorded with a double-beam Cary 5000 UV-Vis-NIR spectrophotometer in steps of 2 nm in the range 300–1500 nm using a 1 mm thick quartz substrate.

2.1.3 Calculation of the optical bandgap via the Tauc plot

The Tauc plot is a graphical representation of the absorption coefficient (α) of a material as a function of the energy of the absorbed photon. The absorption coefficient is a measure of the ability of a material to absorb light, and is related to the density of electronic states in the material[140,141].

The Tauc plot is used to determine the optical bandgap of a material, which is the energy range in a material's electronic band structure in which no electronic

states are available for occupation. In other words, the optical bandgap is the energy required to excite an electron from the valence band to the conduction band, where it can participate in electrical conduction[140,141]. In this work, the use of the Tauc plot allowed us to calculated the bandgaps of several copper oxide thin films.

To create a Tauc plot, the absorption coefficient of a material is plotted on the y-axis and the energy of the absorbed photon is plotted on the x-axis, using the Tauc equation shown in Equation 2-1. The slope of the plot in the high-absorption region is proportional to the square of the bandgap. This allows the bandgap to be determined by measuring the slope of the Tauc plot at a particular absorption coefficient.

$$(\alpha h\nu)^2 = A(h\nu - E_g)$$

Equation 2-1 – Tauc Equation

2.1.4 Contact angle measurements

The contact angle is a measure of the wetting properties of a liquid on a solid surface. It is the angle formed between the liquid-solid interface and the liquid-vapor interface.

The contact angle is determined by the balance of forces at the three-phase contact line where the liquid, solid, and vapour meet. These forces include the surface tension of the liquid and the solid-liquid and solid-vapour interfacial energies.

The hydrophilicity/hydrophobicity of a material's surface can be characterised via the measurement of the contact angle between a droplet (of a given solvent) and the surface, as shown in **Figure 2-1**[142].

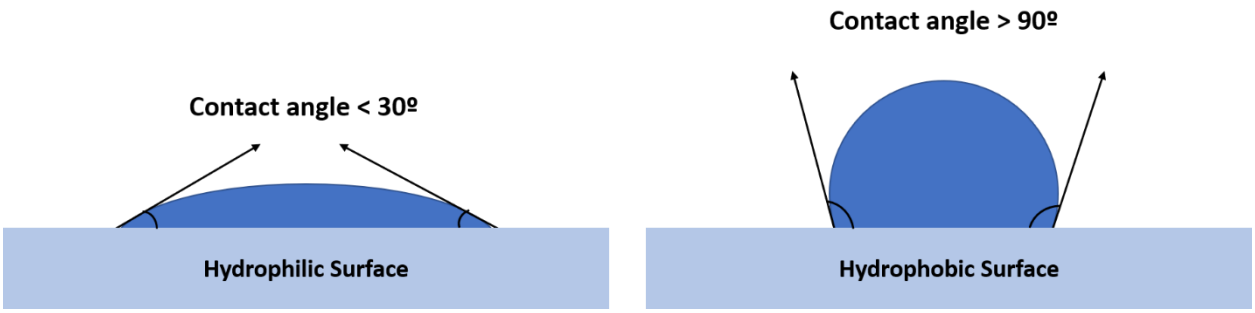

***Figure 2-1**. Behaviour of a water droplet on top of a hydrophilic (left) and hydrophobic (right) surface.*

When the surface is strongly hydrophilic, the liquid (considering water) is strongly attracted to it, causing the droplet to spread out and lower its contact angle (usually lower than 30º). A surface showing contact angles from 30º to 89º are still classified as hydrophilic, with their hydrophilicity weakening with the increase of the angle. A hydrophobic surface is classified as having a contact angle of 90º or above.

The contact angle is an important property in many practical applications, such as in the design of microfluidic devices and in the development of coatings and surface treatments. It is also a useful measure of the wettability of a solid surface and can be used to predict the behaviour of liquids on that surface.

In this work, contact angle measurements were performed using an optical device which allowed the determination of the contact angle of a water or electrolyte droplet with the surface. Each measurement was repeated three times to lessen the error of the measurement. Using this methodology, we were able to characterize the hydrophobicity of a copolymer at different pH conditions.

2.1.5 Nuclear Magnetic Resonance (^{1}H) Spectroscopy

NMR stands for Nuclear Magnetic Resonance. It is a powerful spectroscopic technique that is used to study the structure and dynamics of molecules. In NMR, the magnetic properties of atomic nuclei are used to study the molecular structure and dynamics of a substance[143].

The technique is based on the fact that certain atomic nuclei, such as those of hydrogen, have a magnetic moment and are therefore sensitive to magnetic fields. When these nuclei are placed in a strong magnetic field, they align with the field, just like a compass needle aligns itself with the Earth's magnetic field.

When the sample is exposed to a specific type of radio frequency (RF) radiation, the nuclei absorb energy and flip their alignment from being parallel to the magnetic field to being anti-parallel. This process, called resonance, is associated with a specific frequency that is characteristic of the particular type of nucleus being studied.

By measuring the absorption of RF energy, it is possible to determine the chemical shifts of the various types of nuclei present in the sample, which can be

used to deduce the structure of the molecule. NMR is a non-invasive technique and can be used to study a wide range of substances, including liquids, solids, and gases. With NMR, it is possible to determine the structure of a compound and, with the use of a known molar amount of an easily identifying standard as comparison, it is possible to quantify the samples measured. In this work, NMR was utilized for the characterization of a copolymer, allowing for the distribution of the monomers in the structure.

^{1}H (400 MHz) NMR spectra were recorded using a Bruker Ascend 400 at ambient temperature using deuterated solvents.

2.1.6 X-ray diffraction

X-ray diffraction (XRD) is a technique used to determine the atomic and molecular structure of a material. It is based on the diffraction of X-rays by the atoms in a sample, which produces a pattern of peaks in the diffracted X-ray intensity as a function of diffraction angle. The positions and intensities of these peaks can be used to identify the phases present in the sample, as well as their relative proportions, crystal structure, and other physical properties.

Bragg's law is a principle in X-ray crystallography that explains how X-rays interact with the atoms in a crystal lattice to produce a pattern of diffracted X-rays. According to Bragg's law, when a beam of X-rays is directed at a crystal lattice, the X-rays will be scattered by the atoms in the lattice in such a way that they will interfere with each other. The intensity of the diffracted X-rays will depend on the angle of incidence of the X-rays and the spacing between the atoms in the lattice[144].

The law can be expressed mathematically as:

$$n\lambda = 2d \sin\theta$$

Equation 2-2 – Bragg's law.

where n is an integer representing the diffraction order, λ is the wavelength of the X-rays, d is the distance between the planes of atoms in the crystal lattice and θ is the angle between the incident X-ray beam and the plane of the crystal lattice[144].

This equation shows that only certain wavelengths of X-rays will be diffracted by the crystal lattice at a particular angle. By analysing the pattern of diffracted X-rays, it is possible to determine the arrangement of atoms in the crystal lattice and thereby obtain information about the structure of the crystal[144].

XRD is a non-destructive technique, which means that it can be used to analyze samples without damaging them. It is widely used in a variety of fields, including materials science, geology, and chemistry, to study the structural properties of solids, powders, thin films, and other materials.

To perform XRD characterization, a sample is typically placed in a specialised instrument called an X-ray diffractometer, which generates a beam of X-rays and measures the diffracted intensity as a function of angle. The sample is typically rotated in order to measure the diffraction pattern at a range of angles. The diffraction pattern is then analysed using software to determine the phases present in the sample and other structural information[144].

XRD characterization was executed on a Bruker D2 Phaser powder diffractometer with a Cu Kα radiation source with a wavelength of 1.5406 Å. XRD patterns were recorded in a 10° to 80° 2θ with a 0.021 step and a 0.05 s counting time per step. DIFFRAC.EVA software was used to identify the phases and crystallite sizes of copper oxide thin films.

2.1.7 Scanning electron microscopy

Scanning electron microscopy (SEM) is a technique used to visualize the surface of a sample at high magnification. It works by scanning the surface of the sample with a beam of electrons and measuring the electrons that are emitted from the surface.

In a scanning electron microscope, a focused beam of high-energy electrons is scanned over the surface of a sample. The electrons in the beam interact with the atoms in the sample, causing some of them to be emitted from the surface (secondary electrons). These emitted electrons can be detected and used to build up an image of the surface of the sample[145].

SEM allows for high-resolution imaging of the surface of a sample and can be used to obtain detailed information about the topography, composition, and morphology of the sample. It is often used in a variety of fields, including materials science, biology, and geology, to study the microstructure of samples.

In addition to imaging, SEM can also be used for analytical purposes. By measuring the energy of the emitted electrons, it is possible to determine the elemental composition of the sample. This is known as energy-dispersive x-ray spectroscopy (EDS) or energy-dispersive x-ray microanalysis (EDX) or Auger electron spectroscopy (AES).

SEM was conducted with a Hirox SH-3000 microscope with an accelerated voltage of 25kV. A thin layer of gold was deposited on top of the samples to ensure conductivity.

2.1.8 Auger electron spectroscopy

Auger electron spectroscopy (AES) is a technique used to analyse the chemical composition of a sample at the surface. It works by measuring the energy of the electrons emitted from the surface of the sample when it is bombarded with a beam of high-energy electrons.

The process begins when a beam of high-energy electrons is directed at the surface of the sample. When an electron in the sample is hit by one of these high-energy electrons, it can be ejected from the surface. As the ejected electron leaves the sample, it may collide with another atom in the sample. This collision can transfer energy to the second atom, causing it to be excited to a higher energy state. When this second atom returns to its ground state, it can emit an electron with a characteristic energy. This emitted electron is known as an Auger electron. The energy of the Auger electron is specific to the element that emitted it, so by measuring the energy of the Auger electrons, it is possible to determine the elemental composition of the surface of the sample[146].

In this work, AES was employed to evaluate the oxidation state of copper oxide thin films. In order to analyse if the oxidation state was constant through the film, after analysing the surface, the film was subjected to a few minutes of low

energy ion etching and subsequently characterised. This was repeated until silicon from the substrate was detected.

AES analysis was done using a JEOL JAMP 9500 F Auger spectrometer (JEOL Ltd, Tokyo, Japan) equipped with a Schottky Field Emission gun and a hemi-spherical analyser coupled with a high dynamic multichannel detector.

2.1.9 X-ray photoelectron spectroscopy

X-ray Photoelectron Spectroscopy (XPS) is a scientific technique used to analyse the chemical composition and electronic structure of materials. It is a type of spectroscopy, which allows studying of the interaction between matter and electromagnetic radiation.

In XPS, a material is irradiated with a beam of X-rays, and the energy of the X-rays is used to excite the electrons in the material. The excited electrons are then emitted from the surface of the material and are detected by a spectrometer. The energy of the emitted electrons is measured, and this information is used to determine the elemental composition and electronic structure of the material[146].

XPS is a widely used analytical technique in the fields of materials science, chemistry, and physics. It is often used to study the surface of materials, and it is particularly useful for analysing thin films and coatings. This technique was applied in this work to determine the atomic surface distribution and the surface oxidation state of copper oxide thin films.

XPS analysis was performed on a Thermo K-alpha spectrometer with a 120 mm mean radius Hemispherical Analyzer (HAS) and a microfocussed monochromated radiation (Al Ka,1486.6 eV, microspot continuously variable from 30 to 400 μm diameter) operating under UHV conditions (residual pressure of 1×10^{-9} mbar).

2.1.10 Conductivity measurements

The 4-probe technique is a method for measuring the electrical conductivity of a material that involves using four electrodes to pass a current through the material and measuring the voltage drop across it.

The material to be measured is placed between two pairs of electrodes, which one pair (the "drive" electrodes) has a current passing through it and the other pair (the "sense" electrodes) record the voltage drop across the material. Using Ohm's law (V=RI), the resistance of the material can be calculated, which in turn can be converted to conductivity (conductivity is the inverse of resistance).

The 4-probe technique is commonly used to measure the conductivity of materials that have a low resistivity, such as metals and alloys. It is more accurate than other methods, such as the 2-probe technique, because it eliminates the effects of contact resistance between the electrodes and the material being tested.

2.1.11 Size exclusion chromatography

Size exclusion chromatography (SEC) is a characterization technique that separates molecules by size as they pass through a resin-packed column. This resin is composed by porous beads that can selectivity exclude molecules based on their size (hydrodynamic radius) when a mobile phase transports the molecules through the column. The molecules with a larger hydrodynamic radius travel through the column quicker than the small ones, which are slowed down by the beads[147]. Using an external calibration with known molecular weight standards, the retention time can be related to the molecular weight of the analyte.

SEC characterization was performed with THF as eluent (flow rate 1.0 mL min−1) at 30°C. The SEC has a Viscotek VE 5200 automatic injector, a precolumn, two columns (Styragels HR 5E and 4E (7.8 ft, 300 mm)) and 4 detectors: UV−visible spectrophotometer (Viscotek VE 3210), a Multiangle Light Scattering detector (Wyatt Heleos II), a viscosimeter (Wyatt Viscostar II) and a refractive index detector (Viscotek VE 3580). Polystyrene standards were used to determine the dispersity of

the polymers. Polymer samples were prepared at 5 g/L and filtered through 0.45 µm PTFE filters.

2.1.12 Electrochemical characterizations

All electrochemical characterizations were performed on an "homemade" electrochemical setup. This setup consists of a three-electrode electrochemical glass cell, using a working electrode, a platinum wire as a counter electrode and an Ag/AgCl electrode as reference. The counter electrode is placed in a bridge tube to separate the products produced in its surface from the products produced by the working electrode. The electrolyte used was potassium bicarbonate with a molar concentration of 0.5M and the same volume of electrolyte was used in every experiment (40 ml). The gases used in the experiments (N_2, CO_2) are bubbled into the cell through a solenoid valve, which allows precise control of the start and stop of the bubbling and the flow of gas is controlled by a mass flow controller. At the cell's outlet, a pressure gauge is mounted in order to provide for precise monitoring (and regulation) of the cell's inner pressure. This pressure gauge is then connected to two solenoid valves, one that serves as an evacuation valve and opens to the outside of the system, used when purging the system with a large volume of gas and as a failsafe if the pressure reaches a threshold. The second solenoid valve opens to a gas chromatographer (GC) (GCMS-QP2010-plus, Shimadzu) sample gas loop maintained under constant vacuum. The valves, potentiostat, and gas-sampling events are controlled *via* a proprietary automated system that ensures that a sample of the gas in the headspace of the cell is transferred to the GC-sample loop and subsequently injected into the GC column at selected intervals. This sample is always transferred at a fixed cell pressure (regularised by the solenoid valve at the gas inlet of the cell), assuring the volume of gas transferred remains the same in between experiments. This setup can be seen in **Figure 2-2**.

Figure 2-2. *Photograph of the electrochemical setup used for the experiments. From left to right, there are mass flow controllers, the electrochemical cell and the GC-MS apparatus.*

Quantification of gases using this system was performed by comparing the experimental results with an external standard calibration curve. This calibration curve was constructed from sampling the headspace of the cell, which contained known molar amounts of standard gases (H_2, CO, CH_4, C_2H_4 and C_2H_6), in the exact same conditions as during experimental activity.

2.1.12.1 Cyclic voltammetry

Cyclic voltammetry (CV) is a type of electrochemical analysis that is used to study the electrochemical behaviour of redox (reduction-oxidation) reactions. It involves the application of a series of cyclic potentials to an electrochemical cell, in which the potential of the working electrode is varied in a controlled way with respect to a reference electrode.

In a typical CV experiment, the potential is swept back and forth between two limits (known as the upper and lower potential limits) at a fixed scan rate. During the forward sweep, the potential is increased linearly, and the current is measured.

During the reverse sweep, the potential is decreased linearly, and the current is measured again. The resulting plot is known as a cyclic voltammogram[7].

The resulting current-potential curve, known as the voltammogram, provides information about the kinetics and thermodynamics of the redox reactions taking place at the electrode surface, as well as the nature of the species involved in the reactions. By varying the scan rate, i.e. the speed at which the potential varies, it is possible to observe reactions with different kinetics. CV is widely used in the study of electrocatalysis, corrosion, and electrosynthesis, as well as in the development of electrochemical sensors and energy storage devices.

All of electrochemical tests were performed in a 3-electrode single chamber cell with the anode, a platinum wire, contained in a bridge tube. The cell was filled with 40 mL of 0.1 M $KHCO_3$ aqueous solution as electrolyte. The reference electrode was a Ag/AgCl electrode (saturated KCl solution). A potentiostat PGSTAT 204, regulated via the Metroohm Autolab software, was used to apply the potential between the working and the reference electrode.

2.1.12.2 Linear sweep voltammetry

Linear sweep voltammetry (LSV) is a type of electrochemical analysis in which the potential of an electrochemical cell is varied linearly with time, while the resulting current is measured. It is similar to cyclic voltammetry (CV), but in LSV, the potential is varied in a continuous, linear fashion rather than in a series of cyclic steps.

In an LSV experiment, a potential waveform is applied to the working electrode of the electrochemical cell, and the resulting current is measured. The waveform typically consists of a linear ramp of increasing or decreasing potential, which is applied to the working electrode over a set period of time.

The resulting current-potential curve, known as the voltammogram, provides information about the kinetics and thermodynamics of the redox reactions taking place at the electrode surface, as well as the nature of the species involved in the reactions. However, as opposed to CV, the experiment is limited solely to the study of a cathodic (reduction) or anodic (oxidation) process. LSV is commonly used in the

study of electrocatalysis, corrosion, and electrosynthesis, as well as in the development of electrochemical sensors and energy storage devices. We applied it to determine the potential range at which our electrocatalysts were active for CO2RR.

All of electrochemical tests were performed in a 3-electrode single chamber cell with the anode, a platinum wire, contained in a bridge tube. The cell was filled with 40 mL of 0.1 M $KHCO_3$ aqueous solution as electrolyte. The reference electrode was a Ag/AgCl electrode (saturated KCl solution). A potentiostat PGSTAT 204, regulated via the Metroohm Autolab software, was used to apply the potential between the working and the reference electrode.

2.1.12.3 Chronoamperometry

Chronoamperometry (CA) is an electrochemical technique that allows the determination of the changes a current undergoes over time in a system. With this technique, a constant potential is applied between the working electrode and the counter, which results in a current which is monitored over time. This continuous measurement of the current provides information on the rate of electron transfer at the electrode-electrolyte interface, which can be used to study the kinetics of electrochemical reactions, evaluate the surface area and distribution of reactants and products, and determine the rate of mass transport of reactants and products in the solution. The information obtained from chronoamperometry can also be used to optimize the performance of electrochemical devices, such as batteries and fuel cells[7]. This technique was used heavily in this work for performing electroreduction of CO_2 at a constant potential.

All of electrochemical tests were performed in a 3-electrode single chamber cell with the anode, a platinum wire, contained in a bridge tube. The cell was filled with 40 mL of 0.1 M $KHCO_3$ aqueous solution as electrolyte. The reference electrode was an Ag/AgCl electrode (saturated KCl solution). A potentiostat PGSTAT 204, regulated via the Metroohm Autolab software, was used to apply the potential between the working and the reference electrode.

2.2 Synthetic techniques

2.2.1 Blade coating

In this technique, a doctor blade is used to spread a liquid precursor material onto a substrate. The doctor blade is a flat, straight edge tool made of a material that is compatible with the precursor material. It is typically made of metal or plastic and has a thickness of a few hundred microns. The precursor material is poured onto the substrate and the doctor blade is dragged across the surface of the substrate. As the doctor blade moves, it spreads the material into a thin, uniform layer. The thickness of the layer is determined by the gap between the blade and the substrate and by the linear velocity of the moving blade. There are blades with fixed gap and adjustable blades which allow the fine tuning of this gap.

The doctor blade deposition technique is a simple and cost-effective method for depositing thin films of materials. It can be used to deposit a wide range of materials, including metals, semiconductors, and insulators. However, the technique has some limitations, including the need for a flat and smooth substrate surface and the possibility of introducing defects or impurities during the deposition process.

In this work, doctor blade coating was used as part of the synthesis of copper oxide thin films on top of glass/ITO substrates. A copper oxide precursor solubilised in a solution of dimethylformamide (DMF) and hydroxypropyl cellulose was coated on the substrates using this methodology and was further calcined at 500ºC to form copper oxide.

2.2.2 Dip Coating

Dip coating is a technique used to apply a thin film of material onto a substrate by immersing the substrate into a liquid solution of the material, and then slowly withdrawing it from the solution. After the coating, the resulting film can be further treated using various techniques, such as baking.

Dip coating is a simple and low-cost technique for applying thin films to a substrate. It can be used to coat a wide range of materials, including metals, polymers, ceramics, and composites. It is particularly useful for applications where

the substrate has a complex shape or when a large area needs to be coated. However, dip coating has some limitations, such as limited control over the thickness and uniformity of the coating, and difficulties in coating very thin films.

In this work, this technique was performed in order to deposit thin polymeric films on top of electrodes for CO_2 electrocatalysis.

2.2.3 Spin coating

Spin coating is a process used to apply thin layers of material onto a substrate, such as a wafer or a glass slide. It is typically used in the semiconductor, electronics, and optoelectronics industries to deposit thin films of various materials, such as metals, polymers, and ceramics, onto substrates.

In a spin coating process, a substrate is placed on a spinning platform, and a small amount of coating material is deposited onto the center of the substrate. As the platform rotates, the coating material is spread evenly over the surface of the substrate by centrifugal force. The thickness of the coating can be controlled by adjusting the speed and acceleration of the spinning platform, the amount of coating material applied, and the viscosity of the coating material.

Spin coating is a simple and efficient technique that allows for the rapid deposition of uniform, thin layers of material onto a substrate. It is widely used in the manufacturing of electronic devices, such as smartphones, laptops, and tablets, as well as in the production of solar cells and optoelectronic devices. Spin coating is also commonly used in research and development to coat various materials onto substrates for various applications, such as sensors, batteries, and catalysts.

In this work, thin polymeric and thin titanium dioxide (TiO_2) films were deposited on top of the desired substrates

2.2.4 Breath figure method

The breath figure methodology is a simple and versatile technique for creating honeycomb-structured mesoporous polymeric films. It is based on the evaporation of

a volatile hydrophobic organic solution of polymer carried out in a high humidity environment.

The breath figure method is typically carried out as follows: a solution of a polymer is prepared in a volatile hydrophobic solvent. The solution is then dropped onto a clean surface, such as a glass slide, a silicon wafer, or a metallic film. As the solvent evaporates, water droplets condense on the surface, forming a regular pattern. The size and spacing of the droplets depend on various factors, such as the concentration of the solution, the volatility of the solvent, and the temperature and humidity of the environment[123,124,127].

After the droplets have formed, the solution is left to dry completely. The resulting pattern of holes left behind by the droplets can be used as a template for the deposition of other materials, such as metals or semiconductors, to create ordered arrays of micro- and nanostructures or can be used in order to create ordered mesoporous gas diffusion membranes[123,124,127].

The breath figure method has several advantages over other techniques for creating ordered structures, such as lithography. It is simple and requires only basic equipment, making it an attractive option for researchers and industry. The resulting patterns can be easily tuned by adjusting the conditions of the process, and a wide range of materials can be used.

In this work, a polymeric gas diffusion membrane was synthesised on top of copper oxide electrodes for the electrocatalysis of CO_2.

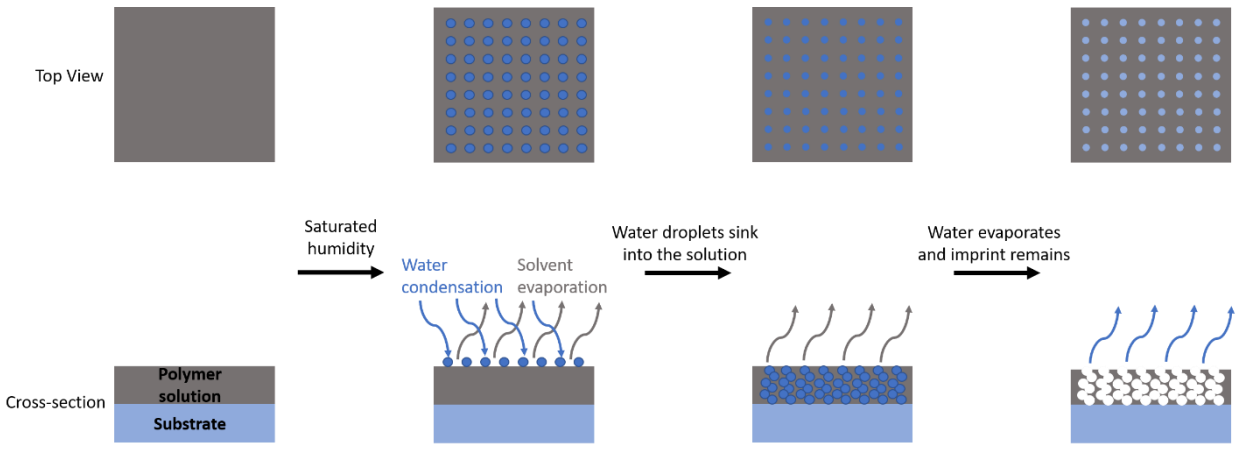

***Figure 2-3**. Schematic depiction of the breath figure methodology.*

3 - Narrow band gap cuprous/cupric oxide thin films prepared via sol-gel methods for the electrochemical reduction of CO_2

3.1 Introduction

Greenhouse gas emissions, particularly those of CO_2, are hitting alarming levels. Over the past decades, great efforts have been made by the scientific community to design new systems and new catalysts to electrochemically reduce CO_2 into potential feedstock to be reused in a so-called circular economy.[148–154] In this respect, gaseous and liquid C_{2+} products are highly desirable due to the high demand associated with such products and the ease of storage.[155] Among the inorganic catalysts available to efficiently perform the CO_2RR electrochemically, copper has proved to be arguably the best alternative despite the inherent lack of selectivity for one or the other adduct.[107,110,156–163] Indeed, the selectivity of copper is tunable to some extent using nanostructured forms of metallic copper[164–168] or using copper oxide precursors with a different micro or mesostructure.[84,169–182,182–184,184–190]. In the latter case, both cuprous and cupric oxide (Cu_2O and CuO) have been employed. Both precursors benefit from bang gaps well centered in the visible part of the solar spectrum (~2.2 eV and ~1.4 eV) and strong extinction coefficient. This adds the ability to inject an electron into the LUMO band of CO_2 upon absorption of a photon, the catalyst acting concomitantly as a photocatalyst and an electrocatalyst.[175,181,184,188,190] Recent studies on Cu_2O have demonstrated that the catalytic activity of such precursors is acquired *via* the *in-situ* reduction of the oxide, at least superficially, forming a nanostructured Cu (0) active surface.[182,183,186] The increase in selectivity of such catalysts, compared to bare copper, is therefore attributed to the nanostructure of the Cu (0) active layer acquired from the CuO/Cu_2O precursor and the presence of oxygen vacancies. The case of cupric oxide (CuO) is somewhat similar, and although the direct reduction to Cu (0) from copper (II) is not favoured according to Pourbaix's diagram, local proton concentrations can drive the reduction of CuO to Cu (0) *via* Cu_2O. As a result, the catalytic activity is

again predominantly attributed to Cu(0).[177,177] Additional to these mechanistic features, the catalytic selectivity of the CuO is generally poor unless it is doped or functionalised with different metallic dopants, [169,170,172,175,176,176,178,180,181] or organic dopants.[181]

Based on these early reports, herein we describe the fabrication of cuprous oxide (Cu_2O) and cupric oxide (CuO) thin films using a facile sol-gel method in air or under a controlled atmosphere of nitrogen gas. The method allows for the selective formation of thin films of any of the two types of oxides directly on top of conducting transparent electrodes, such as Indium tin oxide, *via* the deposition of a copper nitrate precursor. The versatility of the sol-gel approach allowed the fabrication of thin films of CuO containing various types of metal dopants. Interestingly, it was found that the cuprous oxide (Cu_2O) produced using this method possessed a significantly narrower band gap than that of intrinsic Cu_2O. This was later rationalised by the presence of a high concentration of carbon and nitrogen dopants. Furthermore, the CuO and Cu_2O films were characterised by (X-Ray diffraction) XRD, XPS (X-Ray photoelectron spectroscopy) and SEM/Auger emission spectroscopy (AES). Finally, preliminary CO_2 reduction showed some selectivity for forming carbon monoxide (CO) in an aqueous electrolyte at a reasonably low over-potential.

3.2 Results and discussion

3.2.1 Background

CuO and Cu_2O thin films are often produced from Cu metal using chemical vapour deposition techniques such as reactive sputtering or physical vapour deposition.[191–193] However, due to the growing interest in copper oxides for applications to the electroreduction of CO_2, new methods have recently been reported. Available work on the production of CuO and Cu_2O catalysts for CO_2 reduction most often involves either the preparation of CuO/Cu_2O nanoparticles *via* hydrothermal or sol-gel methods and their subsequent deposition onto conductive electrodes,[173,175,176,188] the anodization of Cu sheets to be directly used as electrodes,[180,181] or the electrodeposition from copper precursors.[184,194,195] Nonetheless,

CuO and Cu_2O thin films fabricated directly from sol-gel methods have experienced a recent rise in popularity. Indeed, the ease of fabrication and the ability to produce thick textured films with a high surface area render the latter method very attractive for electrocatalytic applications. This method differs from those expounded above in that the precursors are directly deposited on top of a substrate of choice and subsequently treated thermally, forming oxide films in direct contact with the substrate. The sintering effect of the sol-gel process confers a high degree of structural integrity to the film and enhanced current conduction properties due to intimate grain-to-grain contact.

Hence several reports on the formation of either CuO or Cu_2O thin films from soluble precursors have appeared recently in the literature. Some used copper chloride (CuCl) as a precursor,[178,196,197] or copper acetate,[198] however, copper nitrate $Cu(NO_3)_2$ seems to have reached consensus as the preferred copper source.[173,176,186,199,200] Indeed, contrary to CuCl, copper nitrate is known to be a very stable source of copper ions, highly soluble in aqueous solutions and organic solvents to some extent. The precursor undergoes clean transformation to CuO above 300ºC, giving off NO_2 gas as a by-product. The reaction proceeds through a $Cu(OH)_2$ intermediate when carried out in an aqueous medium. It has been shown to produce CuO crystallites ranging from a few tenths of nanometers to several microns in size, with shapes varying from rods and needles to sheets or flake-like. The lower oxidation state of the copper oxide, Cu_2O, is however, more difficult to synthesise from a sol-gel approach since copper (I) tends to naturally oxidise to its Cu (II) counterpart under the high-temperature oxidative conditions used to produce CuO. The formation of Cu_2O *via* wet deposition techniques has shown to be possible, however, the process is generally carried out in two steps. They involve either the previous formation of Cu (0), which is selectively oxidised to Cu_2O under mild conditions,[189] or *via* the formation of CuO which is subsequently selectively reduced under specific conditions.[194] Alternatively, Cu_2O has been prepared as thin films by sol-gel methods from a copper (II) precursor in the presence of a reducing agent (e.g. glucose).[201,202] The fabrication of the CuO and Cu_2O films described herein was, therefore, inspired by the above work, and based on a copper precursor being calcined at high temperature, typically above 300°C, in air or under a stream of nitrogen gas to yield either cupric or cuprous oxide selectively.

3.2.2 CuO and Cu_2O film fabrication

Due to the difficulty associated with the fabrication of thick and homogeneous films of CuO using the aforementioned methods, we developed a procedure where copper nitrate ($Cu(NO_3)_2$) is dissolved in DMF containing high molecular weight hydroxypropyl cellulose as an additive. The increase in viscosity provided by the cellulosic derivative allows forming thick and homogeneous films of the copper precursor on glass or ITO substrates, using either blade or spin coating. Moreover, the viscosity can be tuned to suit one or the other technique by simply varying the concentration of the cellulose derivative. Since the copper oxide described here are to be applied to CO_2 photo-electroreduction, thick films are desirable to maximise catalytic activity. Therefore, blade coating of a concentrated solution of $Cu(NO_3)_2$ and cellulose precursor were used (See Annex A for details). After deposition of the precursors' layer, the film is dried at 80°C leaving a film of $Cu(NO_3)_2$ with residual DMF embedded in the cellulose matrix, which is readily pyrolyzed during a subsequent calcination step (500°C), leaving homogeneous films whose composition is exclusively CuO (see below) when carried out in air. The CuO film is, therefore, conveniently doped with metals by adding know amounts of metal salts to the sol-gel precursor solution, e.g. Zinc acetate (ZnAc), cerium nitrate ($CeNO_3$) or silver nitrate ($AgNO_3$), which will form CuO films with the corresponding metal. Interestingly however, when the calcination of the Cu-precursor film is carried out under a steady stream of nitrogen gas in an air-tight quartz tube, Cu_2O is formed instead of CuO. Although surprising at first glance, the formation of the lower oxidation state analogue is rationalised from the lesser availability of O_2 during the calcination and the reducing nature of the cellulose precursor and in the presence of N_2.

Interestingly the absorption properties of the Cu_2O films are significantly changed with respect to literature descriptions of Cu_2O films, displaying a very dark colour even in the case of very thin films (100 nm). N-doping was initially suspected to be responsible for such an apparent decrease in bandgap, however, no nitrogen atoms were detected by XPS (see below). Instead, it was found that, depending on the N_2-stream flow rate, a large quantity of carbon remains embedded in the Cu_2O films as a result of the incomplete pyrolysis of the hydroxypropyl cellulose matrix. The thorough analysis of these films is expounded below, showing that the

composition of the films is consistent with the presence of an amorphous form of elemental carbon, as observed in a recent report on carbon-supported CuO electrodes.[198] Interestingly, the amount of residual carbon in the Cu_2O films highly depended on the flow rate used during the high-temperature calcination step (see below).

3.2.3 X-ray diffraction characterisation

The structural characterisation of the produced CuO and Cu_2O films was first carried out by X-Ray diffraction (XRD) on a benchtop diffractometer. **Figure 3-1a** show the XRD diffractograms of all doped and un-doped samples whose fabrication procedure implied a calcination step in air. The characteristic diffraction pattern of the monoclinic tenorite CuO crystalline phase confirms the presence of exclusive CuO fraction in the bulk of the films.

However, diffractograms of films calcined in N_2 displayed the characteristic cubic cuprite Cu_2O crystalline phase (**Figure 3-1b**). The crystallite sizes calculated using the Scherrer method range from 10 nm to 20 nm for both types of oxides (**Figure 3-1**). The latter parameter was calculated using the Bruker XRD processing software, *Diffrac Plus*, after the background was corrected using the diffractogram of a blank substrate identical to those on which the copper oxides were deposited.

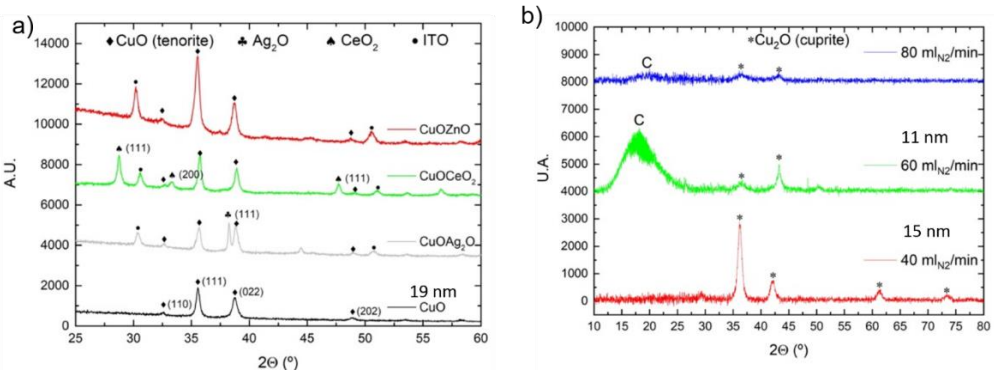

Figure 3-1 *- a) stacked diffractograms of 5% doped and undoped CuO thin films deposited on glass slides; b) stacked diffractograms of Cu_2O thin films deposited on glass slides. The background was corrected against a diffractogram of a blank glass substrate to subtract the typical amorphous broad diffraction peak of the glass.*

The size of the crystallites is relatively modest; however, it is consistent with typical values reported for CuO and Cu_2O thin films. Importantly, the diffractograms do not show detectable amounts of crystalline adducts of metallic copper (Cu(0)). Additionally, the metallic dopants are crystalline enough to be detected as their respective oxides in the case of cerium and silver. However, no crystalline fraction of ZnO was detected on the corresponding Zn-doped CuO films' diffractogram. In the latter case, the metal oxide alloy is not seen to affect the CuO phase to a significant extent either, as seen by the diffractogram corresponding to pristine CuO. The Cu_2O samples follow a similar trend in that their diffractograms do not show any significant difference from expected Cu_2O cuprite phases (**Figure 3-1b**). Interestingly, the diffractograms of the Cu_2O films calcined at different N_2-flow rates show somewhat different crystalline features with respect to one another. As seen in **Figure 3-1b**, their respective crystalline volume varies significantly with increasing N_2 flow rate. Importantly, a very broad peak of semi-amorphous material at $2\theta=17°$, attributed to elemental carbon, is apparent from the samples calcined at a 60 mL/min and 80 mL/min N_2-flow rate. The peak assignment was made *a priori* based on earlier reports,[198] nevertheless, it was later unambiguously confirmed by XPS and SEM/AES characterisation (see below). The amount of carbon is seen to be particularly elevated in films processed at medium N_2-flow rates (60 mL/min), as evidenced by the intensity of the peak. Interestingly, the intensity of the corresponding peak is much lower in samples calcined at 80 mL/min and non-existent in samples calcined at a low flow rate (40 mL/min). Moreover, a concomitant decrease in overall crystalline volume from both the Cu_2O fraction and carbon fraction is observed upon increasing the N_2 flow rate up to a point where the film calcined under an N_2-flow rate above 60 mL/min can virtually be considered amorphous. The presence of carbon is readily rationalised by the fact that the final pyrolysis step in the formation of the oxide is carried out under a controlled inert atmosphere where O_2 is not present in other than trace amounts in the reaction chamber. Indeed, under such oxygen-depleted conditions, the carbon-based matrix (hydroxypropyl cellulose) is not expected to fully oxidise to CO_2 as for the CuO films. Thus, the carbon backbone of the former cellulose additive remains embedded in the metallic oxide films as elemental carbon.

3.2.4 Scanning electron microscopy/ Auger emission spectroscopy (SEM/AES)

To assess the impact of the dopants on the films' surface morphology, we carried out low-resolution SEM imaging (**Figure 3-2**). Although unexpected from the crystalline properties of the films, i.e. small crystallite sizes, most of the copper oxide films studied herein showed a relatively high degree of roughness with peak-to-peak values averaging microns in some cases. This trend is in line with previous work on copper oxide thin films prepared via sol-gel methods. However, in our case, the surface's roughness shows to be dependent on the nature of the element with which the film is doped. Indeed Zn-doped samples are seen as texture-less on an average SEM magnification, while the texture gradually increases when moving to undoped, Ag-doped to Ce-doped (**Figure 3-2**). To further investigate the composition of the bulk of the film, we carried out SEM-AES imaging on the Cu_2O films, where ion etching with argon plasma was used to penetrate through the film's depth. High resolution SEM micrographs and their corresponding Auger spectra are shown in **Figure 3-3**. The surface morphology of the films calcined at 60 and 80 mL/min N_2 flow rate shows an increase in roughness with increasing flow rate. Indeed, SEM micrographs of **Figure 3-3a, 3b and 3c** show a net increase in protrusion density per unit area, reaching a somewhat overwhelming roughness in the case of films calcined at 80 mL/min, with particle sizes approaching microns in size. Interestingly, this increase is not linked to an increase in crystallinity—quite the contrary since the crystalline volume is seen to decrease with increasing flow rate. Therefore, the increase in roughness is likely linked to an increase in the kinetics of oxide formation, inducing fast precipitation of largely amorphous Cu_2O particles. Interestingly, these textured surfaces are reminiscent of previously reported work on copper oxide films made *via* sol-gel methods.[182,194]

Importantly, the Auger spectra confirm that elemental carbon is present in significant amounts throughout the bulk of the films and that its distribution is rather homogeneous across the thickness of the layer. Indeed, after an initial low energy ion etching event for removal of adventitious carbon and oxygen species (usually present on the surface of most air exposed samples) the relative distribution of the main elements, *i.e.* C, Cu, O, remains nearly identical in each sample, even after

several ion etching events (**Figure 3-5**). The distribution of carbon through the bulk of the samples shows a very similar trend to the results obtained from XRD. A large amount of carbon remains in the bulk when the films are calcined under a higher flow rate (60 and 80 mL/min), while carbon is present in much lower amounts in the samples calcined at 40 mL/min.

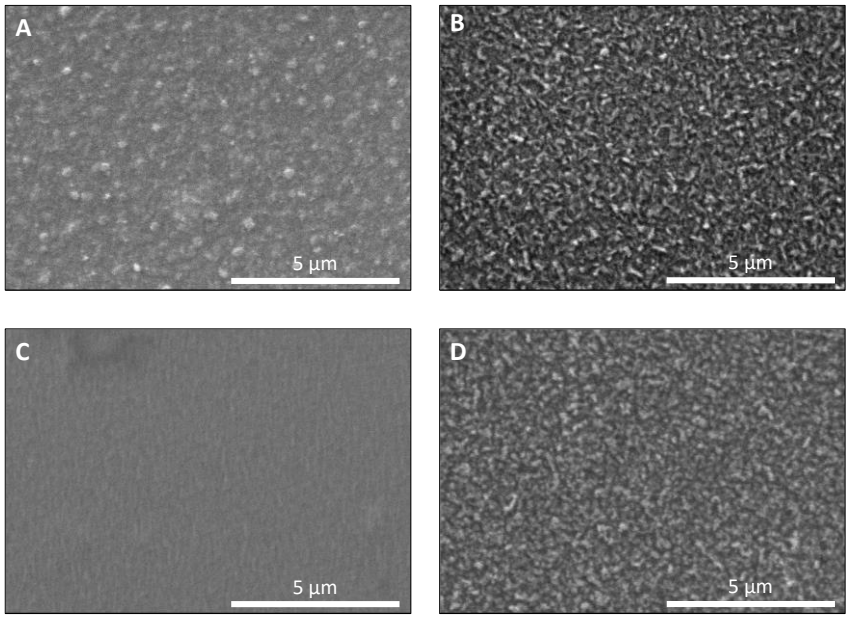

Figure 3-2. *Low resolution scanning electron micrographs of cupric oxide films a) undoped; b) doped with cerium c) doped with zinc d) doped with silver.*

Noteworthy, the latter films show the incorporation of significant amounts of nitrogen atoms in addition to carbon atoms. This can be rationalised by the presence of a large excess of N_2 during the Cu_2O formation, which likely intercalates as a dopant in the Cu_2O structure, as seen in other methods of Cu_2O formation (**Figure 3-3g).**[181,203] SEM images show, however, that the surface of the films fabricated under a 40 mL/min N_2 flow rate is rather inhomogeneous, with protrusions in the range of a few tens of nanometers in diameter scattered along the surface. A semi-quantitative composition analysis based on experimental spectra peak deconvolution using external references (Cu, CuO and Cu_2O) was carried out (see SI). Data confirms that the latter films are mostly composed of pure Cu_2O species, with CuO present only in trace amounts. Additionally, it shows that the concentration of copper is higher with respect to the carbon atoms within the protrusions.

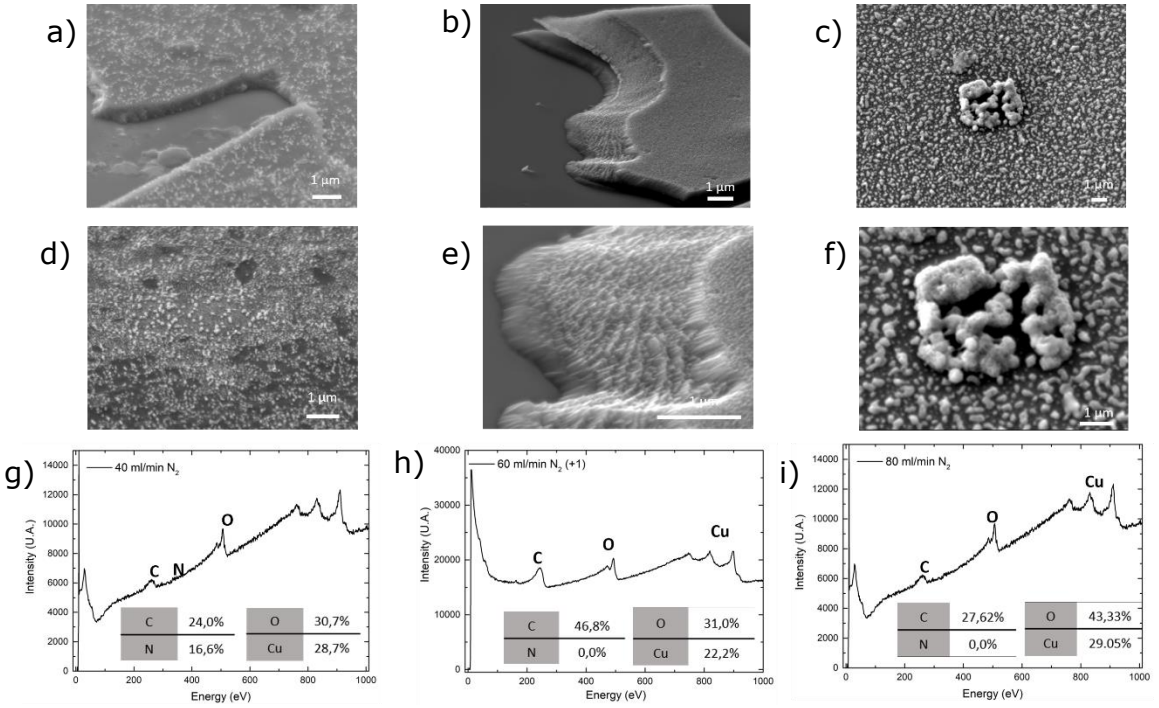

Figure 3-3. *High resolution SEM imaging of thin films of Cu2O calcined at different N2 flow rates a) and d) 40 mL/min; b) and e) 60 mL/min; c) and f) 80 mL/min. Auger spectra recorded from thin films of N2-annealed cuprous oxide thin films at the following flowrates g) 40 mL/min h) 60 mL/min i) 80 mL/min.*

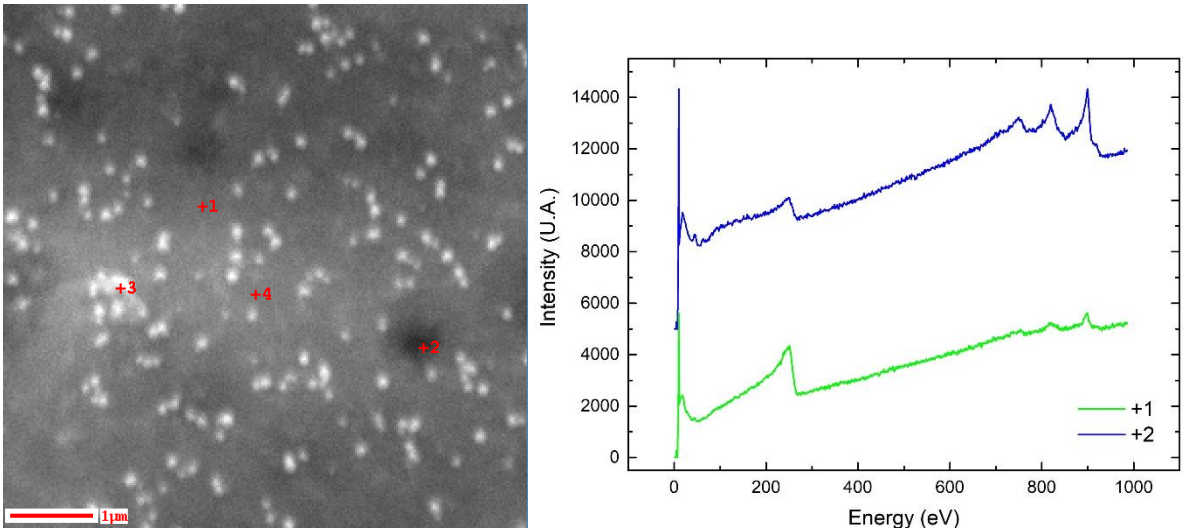

Figure 3-4. *Auger spectra at different regions on the surface of a Cu_2O 60 ml/min film.*

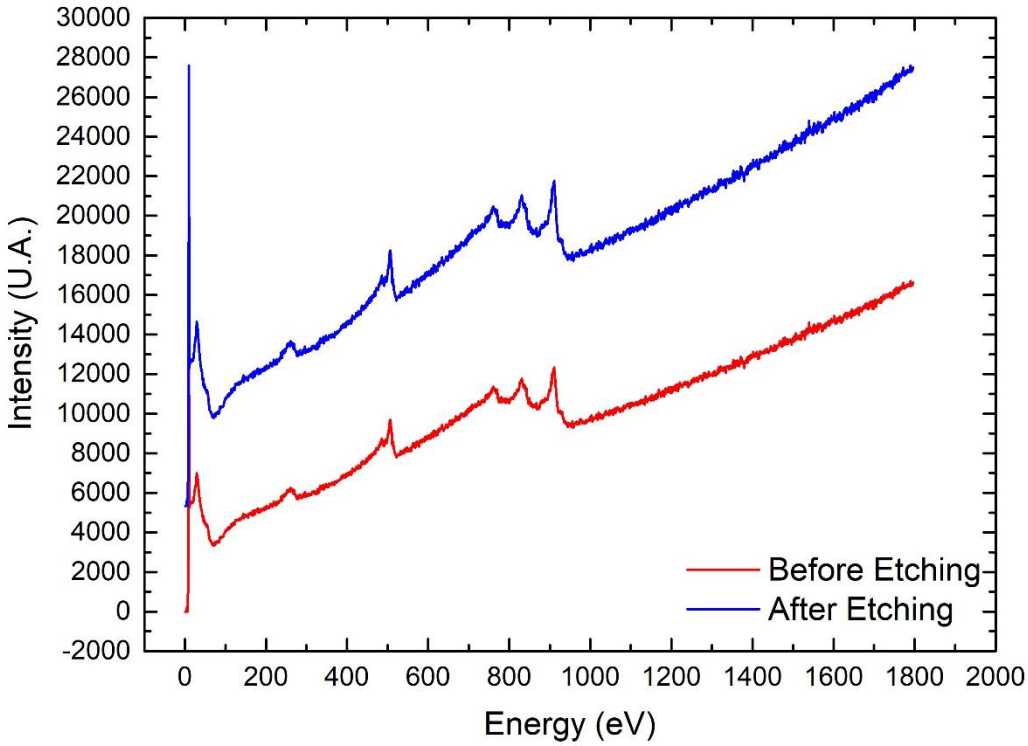

Figure 3-5. *Auger spectra of Cu_2O 80ml/min before and after etching of the film surface by 3 events of ion milling (1 min at 2kV).*

The latter methodology was applied to the films made at a higher flow rate, showing that the copper fraction remains predominantly of cuprous oxide (Cu_2O) nature, however, a substantial amount of CuO is accounted for (**Figure 3-6**). Although counter-intuitive at first glance, greater amounts of CuO in higher-flowrate samples can be rationalised by the availability of oxygen atoms from the hydroxypropyl cellulose organic matrix. The pyrolysis of the latter oxygen-rich molecule is found to be incomplete with an increasing N_2 flow rate, leaving an excess of oxygen atoms to be included in the copper oxide structure. Concomitant to the increase in CuO relative to Cu_2O, a stark increase in carbon content is also observed. This is particularly the case for samples calcined at 60 mL/min, where carbon is now the dominant element in the film, confirming the data from XRD. A similar rationale for the presence of CuO can be applied in this case, whereby the high carbon content underpins the evidence of incomplete combustion of the cellulosic matrix under a higher N_2 flow rate. As this fraction of CuO is not detected by XRD and is only present in significant amounts in the 60 and 80mL/min films, i.e. containing a larger

amount of carbon, it can be assumed that this species is embedded in the carbon matrix in an amorphous state.

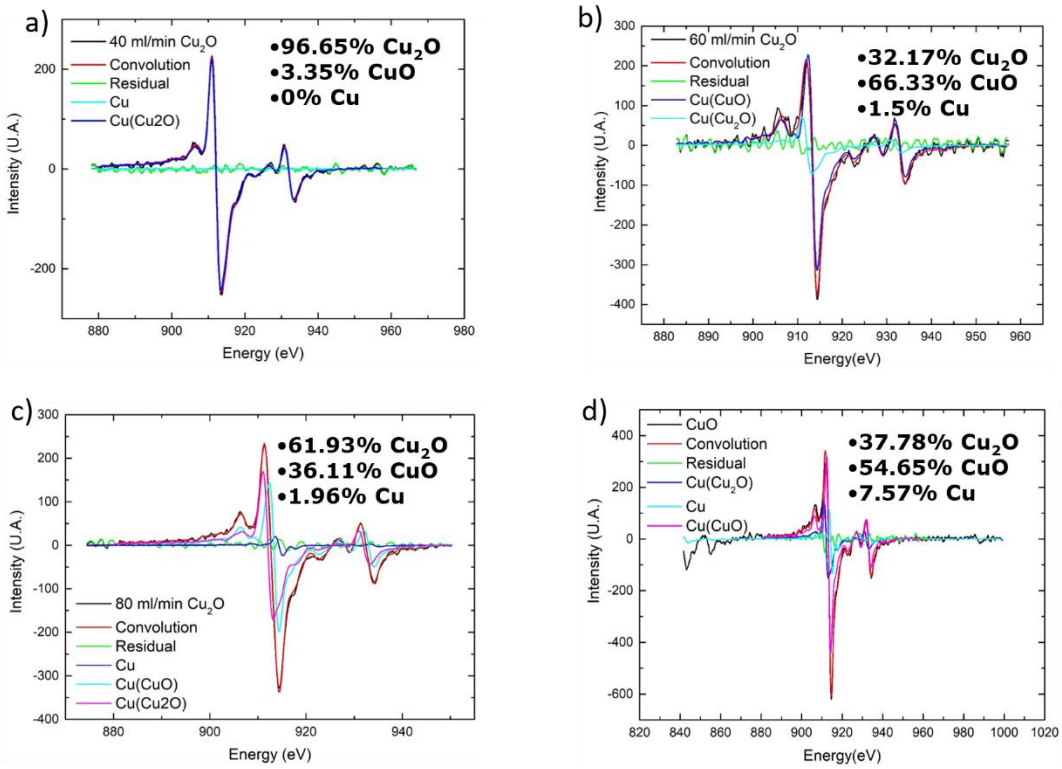

Figure 3-6. *Determination of the oxidation state of the copper present in the a) 40ml/min, b) 60 ml/min, c) 80 ml/min and d) CuO films via semi-quantitative composition analysis based on experimental spectra peak deconvolution.*

3.2.5 X-Ray photoelectron spectroscopy

To shine light on the nature of the films' surface, XPS characterisation was utilised. The XPS spectra complement the analysis from the SEM-AES characterisation, although limiting the analysis to the very few top atomic layers of the film. This comes with a significant drawback in that native surface oxidation, which is readily expected for such types of copper oxide materials, renders the composition ratio between the two types of oxides unrepresentative of the bulk of the materials. However, XPS provides accurate quantification of the absolute elemental composition of the films. As such, the satellite Auger bands characteristic of both Cu(II) et Cu(I) species are present in all the samples of either CuO or Cu_2O.

Furthermore, no electron emission from Cu(0) is detected either, confirming that the surface of the catalyst is composed solely of Cu(II) and Cu(I) species (**Figure 3-7a**).

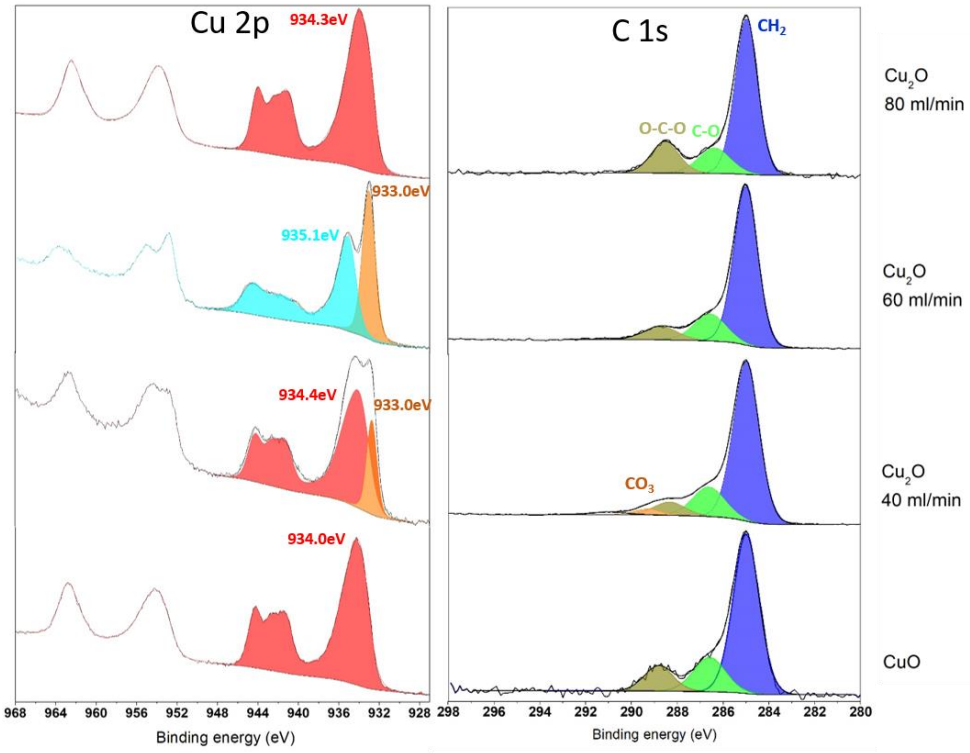

***Figure 3-7**. XPS spectra of CuO and Cu_2O thin films a) showing the Cu and Cu 2+ Auger satellites emission peaks with CuO peaks in red, Cu_2O peaks in blue and $Cu(OH)_2$ peaks in orange; b) showing the C-O and C=O emission peaks.*

In the case of the sample calcined at 60mL/min, no characteristic peak of CuO was detected, however the peak characteristic of copper hydroxide ($Cu(OH)_2$) is present. The presence of $Cu(OH)_2$ presumably stems from the remainder of the hydroxypropyl cellulose matrix or from the reaction of CuO with surface-bound water molecules. Indeed, CuO is known to readily dissolve in mild acidic aqueous conditions, forming the corresponding Cu (II) salt.

For the sample calcined at 80mL/min, CuO is the only species detected, in contrast with SEM-AES results which shows a majority of Cu_2O in the bulk of the film. This indicates that partial pyrolysis of the hydroxypropyl cellulose matrix provides the Cu_2O film with enough oxygen to form a very thin layer of pure CuO on the surface of the film.

Figure 3-8 show the Oxygen and Cu LMM emission peaks for the CuO and Cu_2O films. Analysing the shape of the peaks, it's possible to infer the oxidation state of the copper. For CuO and Cu_2O 80 ml/min, the copper is at oxidation state +2 (CuO), while for Cu_2O 40 ml/min the major oxidation state is +2 (CuO) but the oxidation state +1 (Cu_2O) is also present. In the case of Cu_2O 60 ml/min, the oxidation state is +1 (Cu_2O). It is important to note that XPS is a surface analysis tech and the composition of the bulk film may differ, so a SEM-EDS analysis was performed to analyse the bulk composition of the films.

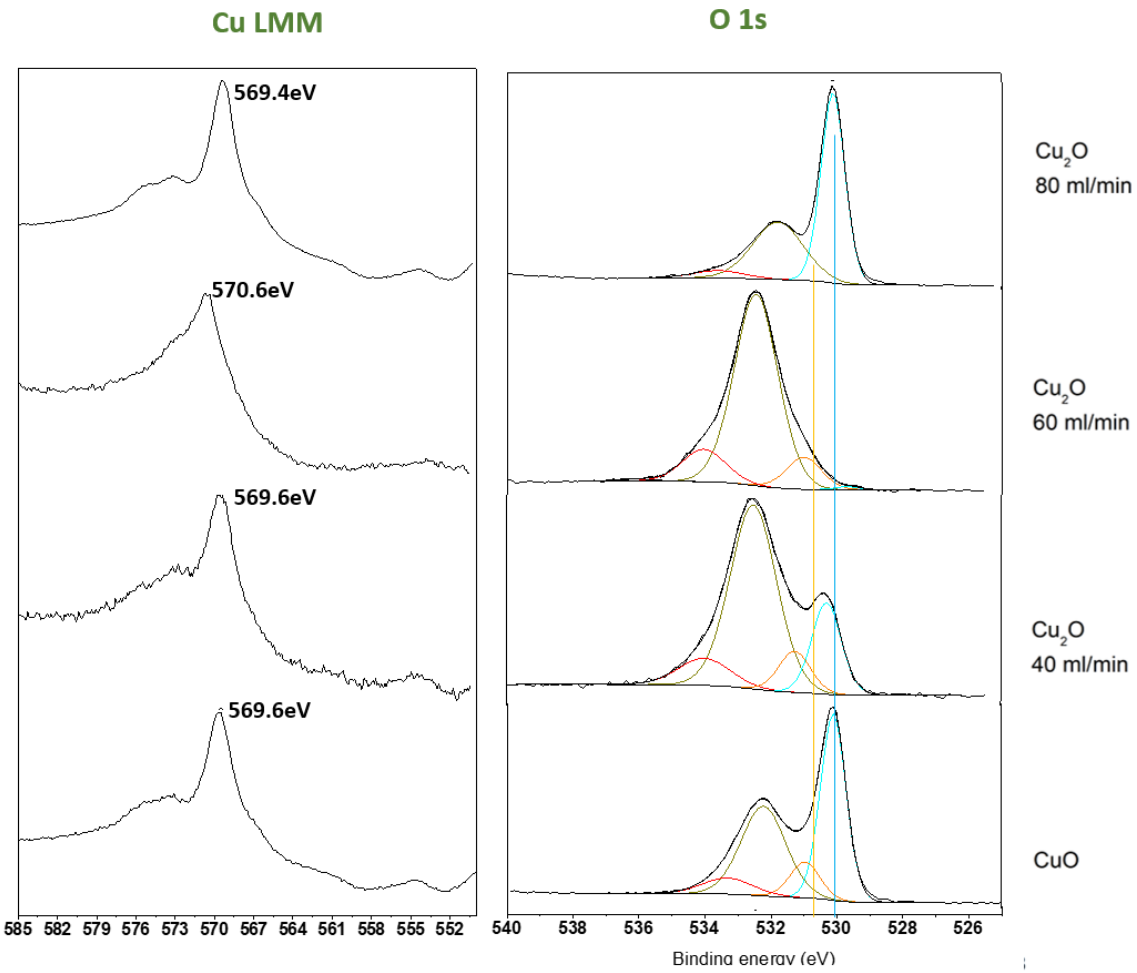

Figure 3-8. *XPS spectra of CuO and Cu_2O thin films showing the Cu LMM (left) and the oxygen 1S (right) emission peaks.*

Table 3-1 summarises the relative composition of the elements in all the films characterised, confirming that a large amount of carbon is present in both oxides, corroborating the data from XRD and SEM-AES. Additionally, emission peaks with a

binding energy corresponding to characteristic C-O and C=O bonds are also detected in the XPS spectra, evidence of incomplete pyrolysis of the cellulose matrix. **Figure 3-7b** shows the characteristic emission peaks of the *C1s* electrons with their characteristic C-O and C=O signature. These adducts likely account for a significant fraction of the total elements as seen by the mismatch between Cu and O elements in the fractional composition analysis (**Table 3-1**). The mismatch is more predominant for the films of Cu_2O calcined under high N_2 flow rates (e.g. **Table 3-1**, line 3), where the amount of oxygen is over 6-fold higher than that of Cu. Overall, these values are consistent with the trend observed by XRD. That is, Cu_2O films calcined under a high N_2 flow rate are seen to contain a large proportion of carbon with respect to the copper and oxygen content, while those calcined at 40mL/min have a lesser amount of carbon compared to copper and oxygen. The ratio of Cu to C in the latter case is in a similar range to that of CuO films.

Table 3-1. *Elements molar fraction of CuO and Cu2O films determined by XPS*

	C	O	Cu	N
CuO	7.4	49	35	
Cu_2O (40ml/min)	21	41	31	
Cu_2O (60 mL/min)	66	22	3.4	2.2
Cu_2O (80ml/min)	53	29	5.4	2.3

3.2.6 UV-Vis and conductivity characterisation

Stark similarities in light absorption properties of the cuprous and cupric oxide films prompted us to carry out an in-depth characterisation of their absorption and electrical properties. That is, both types of oxides show a dark brown to black colouring. Although this is expected for CuO, regular Cu_2O was expected to have an absorption onset well shifted towards higher energy wavelengths, usually appearing reddish when deposited as thin films as a result of a significantly wider band gap than that of CuO (2.2ev *vs* 1.4eV, respectively). To verify that the light absorption properties of the Cu_2O films were linked to a significant decrease in band gap, the absorption spectra of the films were recorded in the UV-visible range, and the effective band gap was calculated *via* a Tauc plot (**Figure A 8** to **Figure A 11**). The absorption spectra and Tauc plots for the two types of oxides are shown in **Figure 3-9**. The UV-Vis spectra confirm the visual similarity between the two types of

oxides, and the Tauc plot further confirms that the Cu_2O underwent a very significant decrease in band gap (**Table 3-2**). Although doped Cu_2O layers with wider or narrower band gap than intrinsic Cu_2O have been described in the literature, such a stark decrease is quite unique for Cu_2O. The rationale behind this apparent decrease is likely the result of heavy carbon and nitrogen doping.

Due to the potential applications in photogeneration devices (e.g. photovoltaics) of such a narrow band gap Cu_2O, it is essential to assess the impact of the alloy distribution on the electrical conductivity of the films. For that purpose, a home-built Van der Paw apparatus was used to measure surface conductivity with a four probes setup. As expected, the heavily doped Cu_2O (60 and 80 mL/min N_2-flow rate) showed a conductivity value about two orders of magnitude lower than its more lightly doped analogue (40 mL/min N_2-flow rate). Nevertheless, the conductivity is comparable to available values from the literature for solution-processed Cu_2O (**Table 3-2**).[204–206] The conductivity reaches 2.28 S/cm for samples calcined at 40 mL/in, which is remarkable since it stands in the same range as CuO films. Overall, this data shows that carbon doping has a strong impact on the band gap of Cu_2O, as well as on the electrical conductivity. However, a compromise between dopant concentration and reasonably high electrical conductivity can be found, as exemplified by the samples calcined at a 40 mL/min flow rate.

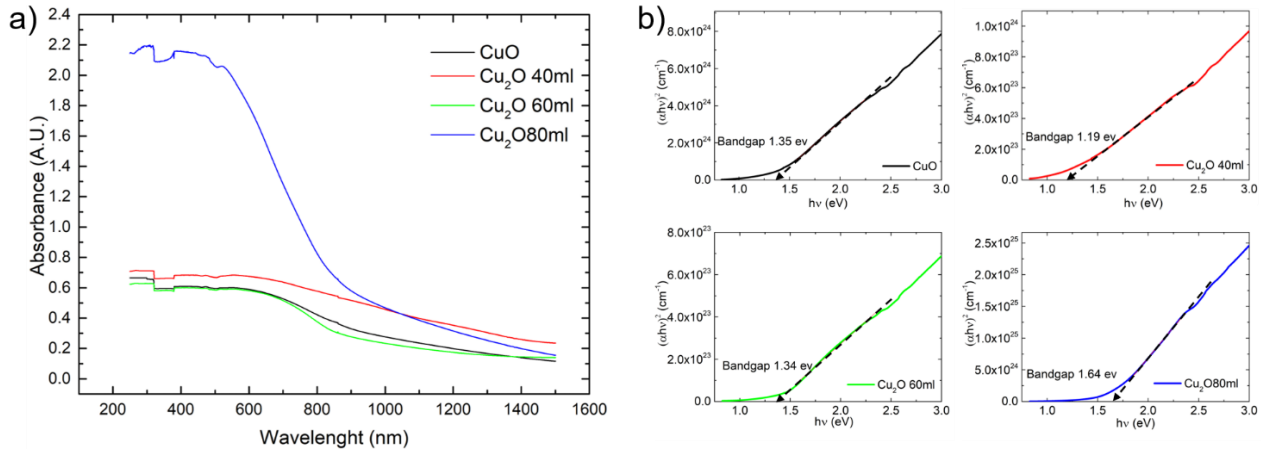

Figure 3-9. *(a) Absorbance spectra and (b) Tauc plot of the CuO and Cu_2O films deposited on quartz substrates.*

Table 3-2. *Bandgap, conductivity and ratio between Cu(I) and Cu(II) for each of the copper oxide films.*

	Conductivity (S/m)	Optical band gap (eV)	Cu (I)/Cu (II) relative ratio (%)
CuO	6.25	1.35	41/59
Cu_2O (40ml/min)	2.28	1.19	97/3
Cu_2O (60 mL/min)	0.026	1.34	33/67
Cu_2O (80ml/min)	0.015	1.64	63/37

3.2.7 Electrochemical reduction of CO_2

The ability of the different copper oxides to catalyse the CO_2 reduction reaction was assessed. To do so, the films were deposited on indium tin oxide (ITO) substrates in identical conditions as above. The choice of ITO for that purpose was motivated by the future goal of applying our films to the photo-electroreduction of CO_2, hence the necessity of a transparent and conductive substrate. Fluorine doped tin oxide (FTO) substrates were also considered but ITO showed better performance. Therefore, ITO substrates of a nominal 15 ohm/sq sheet resistance were used for this purpose. A preliminary study was carried out to verify that the temperature used during the calcination step had no detrimental effect on the conductivity of the substrate. A significant drop in sheet resistance was observed upon calcination at 500°C. Nonetheless, the final sheet resistance remained sufficiently low for electrochemical experiments, with a value reaching about 159 ohms/sq (Table S2). Additional to the electrical properties of the substrates, a linear sweep voltammetry (LSV) towards negative potentials in a three electrodes cell set up in the conditions used for the CO2RR allowed establishing the experimental range under which ITO substrates are stable during the electrochemical experiment. Voltammograms indicate that reduction voltages up to about -0.90 V (*vs* RHE) could be used. However more negative potentials have a direct impact on the integrity of the ITO layer, which is seen to reduce to In(0) or Sn(0) species as evidenced by the resulting metallic lustre (**Figure A1**).

A subsequent LSV experiment with an ITO substrate on top of which a CuO layer was deposited confirmed that the ITO layer is compatible with CuO as a catalyst in that the onset of reduction in a $KHCO_3$ (0.5 M) solution is significantly lower than the reduction potential of ITO. Indeed, **Figure A 2** to **Figure A 5** show the LSV of undoped CuO and Cu_2O in N_2-degassed and CO_2-saturated electrolytes. A faradic current at voltages as low as -0.40V (*vs* RHE) was observed in both cases. Additionally, the latter experiment indicates, due to the increase in current, an explicit reducing catalytic activity, presumably of H_2O or CO_2, which are the predominant species in solution. Therefore, the subsequent quantification of the electrocatalytic activity of the copper oxide layers towards the CO_2RR was carried at reduction potentials ranging from -1.0 to -0.60V *vs* RHE in $KHCO_3$ near pH 7.

With these preliminary parameters established, we then carried out constant potential chronoamperometry experiments to evaluate the rate at which the catalysis reaction occurs. Experiments at -0.60V vs RHE show a low reaction rate, with current densities around 1 mA/cm^2, while the main product of catalysis is H_2. The rate increases significantly, however, under more negative electrical potentials, with currents reaching values of 2.2 mA/cm^2. However, the copper oxide films showed a strong tendency to delaminate in the very early stages of the catalytic process under electrolysis at potentials below -0.50V vs RHE. This effect is evidenced by the stark decrease in current density recorded in all chronoamperometry experiments, as seen in Figure 3-10 (black curve). This effect is likely the result of water molecules diffusing through the copper oxide layer and being subsequently reduced to H_2 at the ITO/copper oxide interface. The production of gas at the interface would therefore be the reason for the film delaminating. Additionally, the structural modification of the catalyst surface under electrolytic conditions is expected to significantly weaken the binding interaction between the film and the ITO surface (Van der Waals or electrostatic). Further evidence for the process to be electrochemically triggered is that no delamination occurs in a similar time frame when the film is left in the electrolyte with no electrical potential applied. To circumvent this setback, a thin layer of TiO_2 was intercalated between the ITO and CuO (**Figure A 7**), however, with no significant improvement. Nonetheless, the electroreduction reaction was quantified via head-space gas chromatography and the total faradic efficiency was calculated. Figure 3-10**b** shows the faradic efficiency and the product distribution for

the three main catalyst types studied herein for chronoamperometry experiments carried out at -0.60V (vs RHE) for the longest time before delamination occurred. As seen in Figure 3-10**a**, delamination occurred within seconds of the process's initiation in the case of CuO, as evidenced by the fast current drop. Cuprous oxide films proved more robust, with delamination occurring later than 300 seconds after the electrolysis had begun. Despite these limitations, quantification after a short electrolysis time showed a nearly quantitative total faradic efficiency for all catalyst types. However, the selectivity of the CO2RR is overwhelmingly shifted towards H_2, although a modest quantity of CO could be detected.

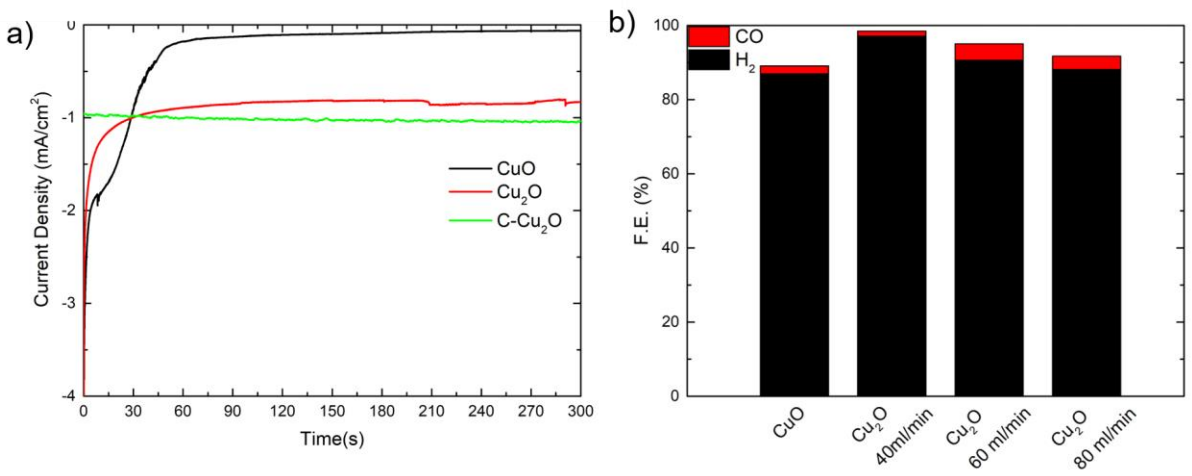

Figure 3-10. *a) Chronoamperograms of CO_2 reduction experiments carried out with the three types of copper oxide films at -0.6 V (vs RHE) for 5 minutes in 0.5 M $KHCO_3$; b) Faradic efficiencies of the corresponding experiments calculated from the quantification of the electrochemical cell head space and from the expected quantity of produced from the electrical charge passed through the catalyst during the experiment.*

3.3 Conclusion

To conclude, we have developed a convenient sol-gel method to prepare both cupric and cuprous oxide from a single precursor by controlling the gaseous atmosphere of the pyrolysis step. That is, carrying out the pyrolysis step under a saturated atmosphere of N_2 has a reducing effect on the copper precursor, forming Cu_2O exclusively. We additionally demonstrated that under the latter conditions, the Cu_2O is doped with significant amounts of carbon resulting from the incomplete

pyrolysis of the cellulosic additive used during the film deposition. The extent of doping has been shown to be linked to the N_2 flow rate used in the pyrolysis step. Nitrogen is also seen to dope the Cu_2O film when a low N_2 flow rate is used, presumably from nitrogen atoms coming from the nitrate precursor counter ion. Importantly, carbon doping has a significant impact on the band gap of the Cu_2O films, decreasing it from a standard experimental value above 2 eV to a value in the same range as that of CuO (1.3 eV). This is a unique feature which is expected to have an impact on the photocatalytic properties of these films. The electrical properties of the films were characterised, showing a decrease in conductivity with increasing carbon doping concentration. However, the conductivity of lightly C-doped Cu_2O was only slightly lower than that of CuO. Early electrochemical catalytic activity towards CO_2 reduction was characterised by chronoamperometry and quantification of the gaseous products. Results showed very similar activity for all three copper oxide types studied, showing modest carbon monoxide (CO) faradic efficiencies. The latter study was somewhat hampered by the fact that the films showed a marked tendency to delaminate upon electrolytic conditions at potentials above - 0.50V *vs* RHE. A solution for the delamination is shown is the next chapter.

4 Hydrophobic mesoporous copolymer layer for tuning the selectivity of CO_2RR

4.1 Introduction

Despite late breakthrough discoveries in the field of CO_2 catalysis, the mechanistic implications underlying the formation of the different CO_2-reduction adducts on the catalyst surface are still not well understood. For example, the formation of hydrocarbons from metallic surfaces arise from a common metal-bonded carbonyl intermediate which undergoes successive dimerization and/or hydrogenation steps. The affinity of each of the intermediates for the metal, as well as the kinetics of each step are a key determinant of the reaction's selectivity. These late considerations indicate that high selectivity towards single products would therefore require the subtle modification of the surface of the catalyst at the atomic level rather than the nanoscopic level. Indeed, early strategies have included the synthesis of binary or ternary metal alloys, which have shown to have a great impact on the CO_2 selectivity[17,21,38,98,165,167,197]. However, since metal alloys consist of segregated domains of crystalline metal entities, an intimate heterogeneous metal-metal contact in which reaction intermediates are allowed to shift metal centers, can only be found at grain boundaries. Therefore, the catalytic properties of the alloy are often difficult to control.

Recent reports have shown that interactions of the above-mentioned intermediates with the catalyst can be tuned *via* the adsorption of organic molecules on the catalyst surface itself. Results showed that either elemental carbon, small molecules or polymers can have a strong impact on the selectivity of the CO2RR from a metallic or oxide-based catalyst. Indeed, the functionalization of catalysts surfaces with small molecules known for their activity in the reduction of CO_2 has recently attracted considerable interest. Molecules such as secondary amines, whose CO2-reduction capability have long been known, have been used to functionalize copper or silver catalyst's surfaces[17,155,207–209]. Pyridine, or carbenes derivatives, in particular, have shown to shift the selectivity of metal-based catalysts to a significant extent[96,210–212].

Second to these small molecule alternatives, polymers have been recently investigated as an additive to be deposited on top of the active catalyst surface to mediate the selectivity of the CO2RR[73,93,94,96,99,101,102,135,213]. Polymers, contrary to small molecules can be deposited as thin layers on top of the catalyst surface, therefore mediating the diffusion of gases in and out of the catalyst surface. The hydrophobicity of this polymers is extremely important, as recent studies have shown that hydrophobicity can have a big impact on the selectivity for CO2RR by limiting the concentration of water at the catalyst surface and improving the CO_2 concentration[94,99–103,111,136].

Hydrophobic honeycomb self-assembled polymers are a new class of materials that are attracting a lot of attention[123–132]. They are made up of polymer chains that have the ability to self-assemble into a honeycomb-like structure. This structure is achieved through the breath figure method. This method involves the use of a polymer solution that is applied to a substrate, typically a glass or silicon wafer. The substrate is then exposed to a humid environment, which causes water droplets to form on the surface of the polymer film. These droplets act as a template for the formation of air-filled pores in the polymer film, which results in a regular honeycomb-like structure. The hydrophobic nature of these polymer films provides a unique environment that can improve the selectivity and efficiency of catalytic reactions[94,96,100–102,111,135–137].

These films can also be defined by their hydrophobic/hydrophilic switching properties and have been used for bioadhesion and tunable wettability applications. As examples of bioadhesion applications, Li et al.[128] in 2023 have introduced didodecyl selenide in the structure of a ordered honeycomb film to not only improved the biocompatibility but also in order to control the hydrophobicity/hydrophilicity of the film *via* redox reactions while Yin et al.[132] prepared highly ordered porous honeycomb-like films with a hydrophilic CO_2-sensitive melamine derivate that acts as a wettability switch triggered by CO_2, which allows to change the cell adhesion properties of the film. Moreover, a hydrophobic/hydrophilic transition can be triggered by using well-designed block copolymer based on a pH-sensitive block, as seen in the works of Marcasuzaa et al[131] and Escalé et al[133]. Both these works show that the formation honeycomb structured film from a copolymer containing a pH sensitive block, Poly 4-VinylPiridine (P4VP) in these examples, results in a pH-

triggered wettability (hydrophobic when above the pKa of the P4VP, otherwise hydrophilic).

Herein, we aim at studying the extent to which the diffusion of the gases though a (co)polymer layer has an impact on the selectivity of metallic and metal oxide catalysts, particularly copper oxide type catalysts. As seen in **Chapter 3**, copper oxide thin film catalysts suffer from stability issues, delaminating from the substrate during electrocatalysis. For the purpose of not only tuning the selectivity of these catalysts but also ensure their long-term stability under electrochemical conditions, we describe the synthesis of methacrylate-*block*-vinyl pyridine copolymers, and their impact of the CO2RR selectivity on CuO, Cu_2O, Cu and Ag catalyst. We assessed the impact of gas diffusion to the catalyst by comparing the selectivity of the above-mentioned catalyst to which either a micrometer thick mesoporous layer of PolyMethylMethAcrylate-*block*-Poly-4-VinylPyridine (PMMA-*b*-P4VP) or a continuous nanometer thick layer of the same block copolymer. The selectivity of the catalyst-polymer systems was linked to a myriad of physical parameters such as porosity, hydrophobicity, reaction pH and layer thickness in order to draw a clear trend and identify the key factors dictating the shift in selectivity. We put particular focus of copper oxides catalysts deposited on transparent conductive oxide glass substrates since mesoporous (PMMA-*b*-P4VP) layers were additionally found to have a dramatic impact on the structural stability of the catalyst layer. Overall, we found that both hydrophobicity and the gas diffusion properties through the copolymer layer play a major role in mediating the selectivity of the CO2RR. We found that both parameters can be tuned to a significant extent to favour one or the other CO2RR adduct.

4.2 Results and discussion

4.2.1 Fabrication of PMMA-*b*-P4VP

The study described herein originates from the aim of using polymer membranes to protect copper oxide catalysts for the CO2RR. Indeed, we found that copper oxide thin films deposited from sol-gel methods on transparent conducting electrodes were prone to delamination under electrochemically reducing conditions

(**Chapter 3 3** of this work). Therefore, we originally focused on developing mesoporous copolymer films deposited on top of the catalyst surface, using the so-called "breath figure" approach to tackle this setback[123–125]. Such approach consists in creating a highly arranged network of micrometer-sized pores throughout the polymer cross section during the deposition step. The process relies on the controlled self-assembly of water droplets on top of the polymer film during the formation of the film from wet techniques such as drop casting or spin coating. The condensing micrometer-sized droplets arising from the cooling of the film upon the evaporation of the highly volatile solvents used in the process arrange in a hexagonal close-packed fashion, imprinting their shape onto the polymer surface and through the bulk of the layer if the latter is thick enough to accommodate large voids. The method is known to be tolerant to a wide range of polymer structures and molecular weights insofar as the polymer structure has a sufficiently high degree of hydrophobicity. Therefore, polystyrene or PMMA backbones have become the benchmark for forming porous films *via* a "breath-figure" approach. A deriving block copolymer of the latter two structures have been shown to provide the necessary hydrophobicity to form the porous network, while being able to add key functionality to the final porous film. As such, we envisioned the synthesis of a PMMA-*b*-P4VP copolymer in which the amphoteric character of the pyridine group allowed tuning the hydrophobicity properties of the catalyst environment after the copolymer film is deposited on the catalyst surface. The effect of hydrophobicity on the catalyst performance was assessed by varying the pH of the CO2RR conditions. Additionally, the concentration of the casting solution could be tuned in a way to produce copolymer membranes with a wide range of pore sizes. Finally, the effect of the porous copolymer layer on the catalyst performance was compared to the performance of a dense thin copolymer film of identical chemical composition as the latter. The copolymer layers were tested on three types of catalysts, namely copper oxide (CuO and Cu_2O) fabricated *via* sol-gel methods and deposited on top of transparent conductive electrodes, silver foil and copper foil.

The synthesis of the copolymer was carried out *via* a nitroxide-mediated controlled polymerization. A first PMMA block temporarily terminated by the resulting SG1 radical from the initiation step, was synthesised. The reaction was carried at relatively high concentration in DMF, in a 0.7:100 initiator: monomer ratio. The

temperature and reaction time were optimised to yield a PMMA block of approximately 32000 Da (see **Annex B** for SEC characterization). After purification by precipitation, the PMMA block was reinitiated in the presence of a quantity of 4VP monomer as to incorporate a P4VP block, leading to a final ratio of PMMA:P4PV of 78:22 and a final molar mass of 40000 Da. The latter ratio was deemed optimum to grant a high enough solubility in a volatile solvent such as dichloromethane or chloroform and high degree of hydrophobicity. The exact ratio between each block was determined accurately by ^{1}H NMR (**Figure 4-2**), while the final molar mass and degree of polymerization were determined via analytical SEC against a polystyrene standard calibration (**Annex B**).

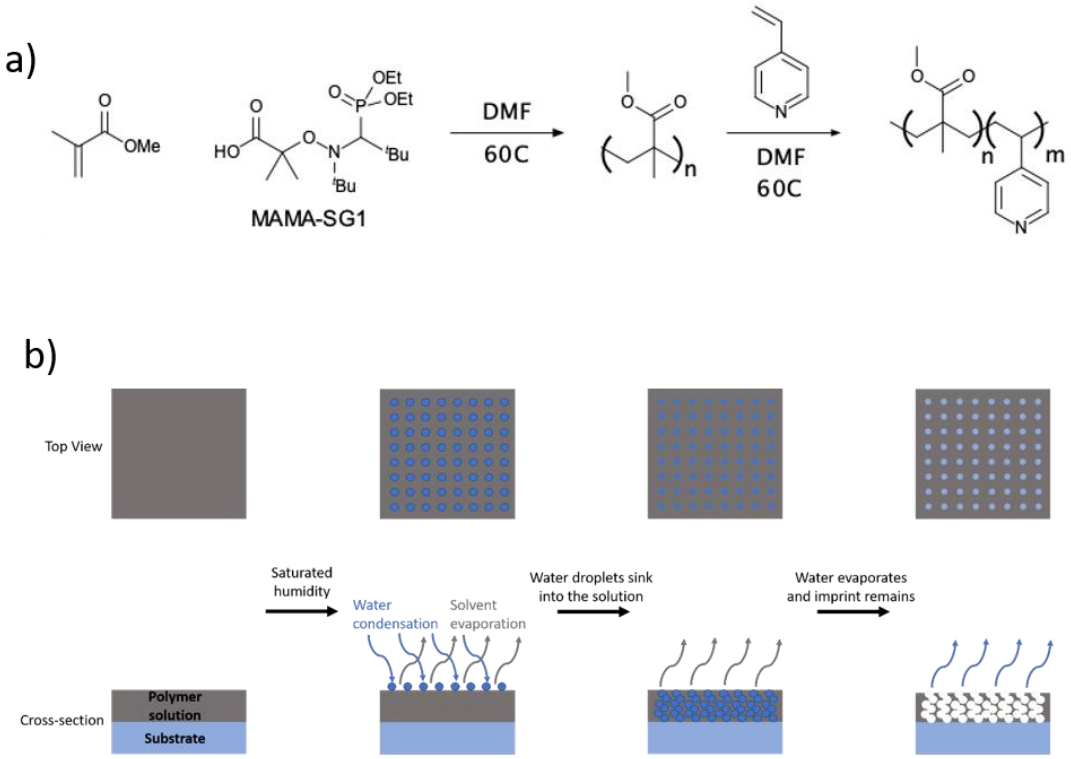

Figure 4-1. *a) Schematic depiction of the synthetic route to the PMMA-b-P4VP copolymer. b) schematic depiction of the breath figure approach to porous polymer membranes*

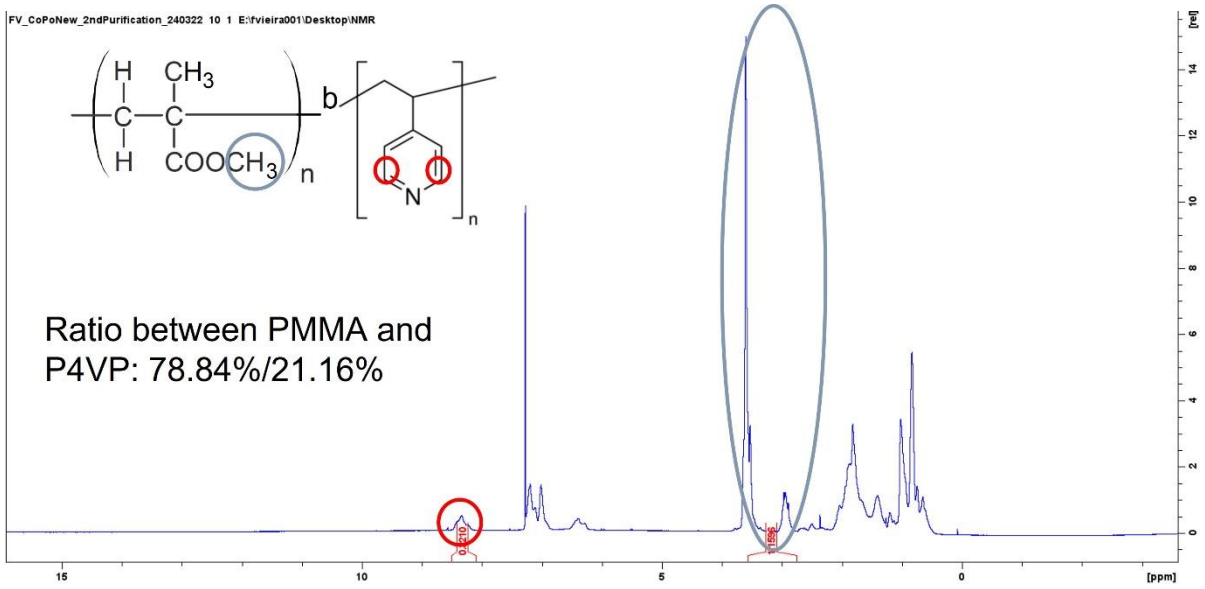

Figure 4-2. *^{1}H NMR spectra of the copolymer in $CDCl_3$.*

The film forming properties of the copolymer were subsequently evaluated on CuO and Cu_2O thin film catalysts in order to assess the compatibility of the method with the rather rough surface of the catalyst, as well as to assess the impact on the catalyst lifetime. The fabrication of CuO and Cu_2O films is described elsewhere, in brief, a copper salt precursor is deposited via blade coating on top of indium tin oxide substrates, and subsequently heat-treated at 500ºC. The formation of the copolymer membrane on top of the catalyst surface was carried out by placing the substrate in a closed vessel with a water vapour-saturated atmosphere (>90% humidity) at room temperature. A constant volume of a solution of copolymer in $CHCl_3$ was drop-cast on top of the substrate, and the solvent was left to evaporate over a 10 min timeframe. A white layer results from the drying process, characteristic of the porous nature of the film. On the other hand, a colourless layer is generally characteristic of the copolymer forming a dense layer. Interestingly, the pore size, and therefore the overall porosity, could be tuned to some extent, by varying the concentration of the PMMA-*b*-P4VP copolymer used for casting the membranes. It was found that a range between 2.5 g/L and 8 g/L is the stable range for pore size, since at the ends of this range the copolymer membranes fail in protecting the copper oxide thin films from delamination. Optical microscope photographs of intermediate porosity membranes (~1.66 µm) were recorded

showing a nearly perfect hexagonal arrangement of the pores throughout the surface (**Figure 4-3**).

Importantly, scanning electron micrographs display multiple layers of micrometer-sized pores along the membrane's cross section, opposed to the archetypical membranes fabricated *via* the "breath figure" approach (**Figure 4-5**). As seen in **Figure 4-5b** foam-like membranes form, however quite importantly, the spherical interconnected voids show a significant number of openings within the interconnections, whose size is in the range of a few tenth of nanometers (red arrows). This feature is capital to the expected function of the membrane as to allow gases to diffuse to and from the catalyst surface through the membrane layer. Images of membranes resulting from employing extreme conditions of concentrations are shown in **Figure 4-5**. As shown in **Figure 4-4**, highly dilute solutions of copolymer yield poorly resolved pores, i.e. small non-interconnected pores, while concentrated solutions of copolymer yield an inhomogeneous pores arrangement with pores unevenly scattered throughout the surface and a "stickier" film. Due to this structural and morphological analysis, the ideal concentration for the formation of the mesoporous membrane was determined to be 6 mg/ml, with an average surface pore size of 1.66 µm.

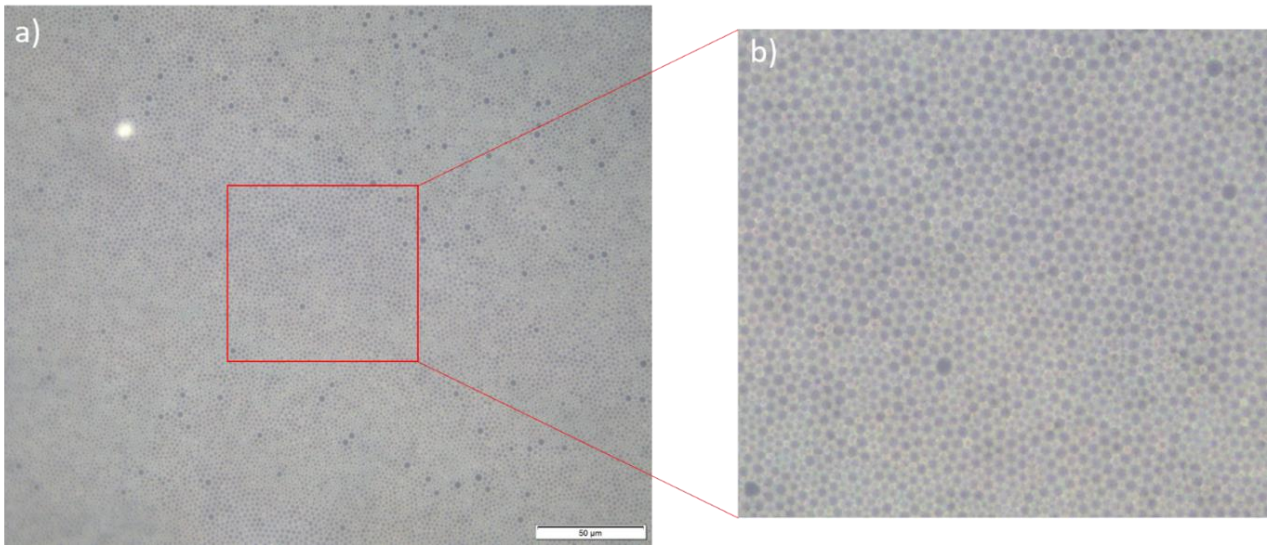

***Figure 4-3**. Optical microscope imaging of a (a) intermediate porosity (~1.66µm) membrane and (b) a zoom in of it.*

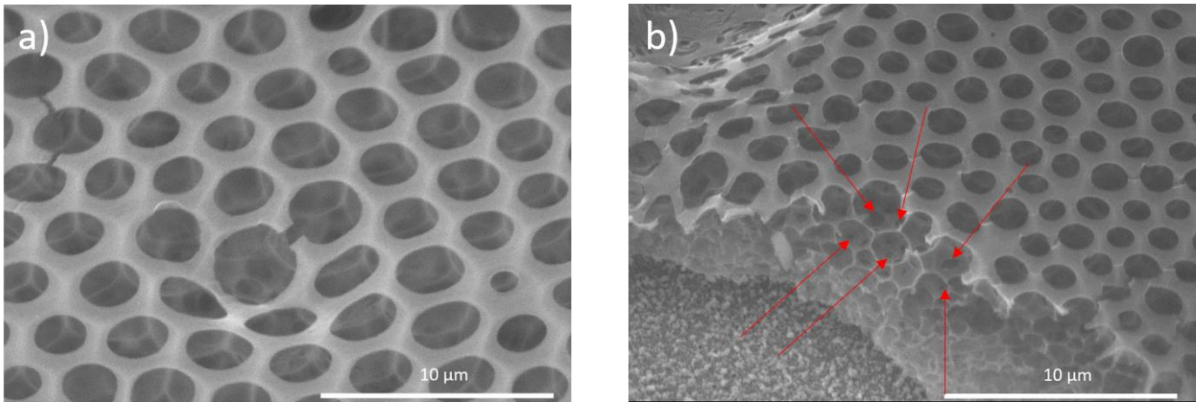

***Figure 4-5**. SEM micrographs of an intermediate porosity (~1.66µm) membrane in (a) top view and in (b) a 60° tilt.*

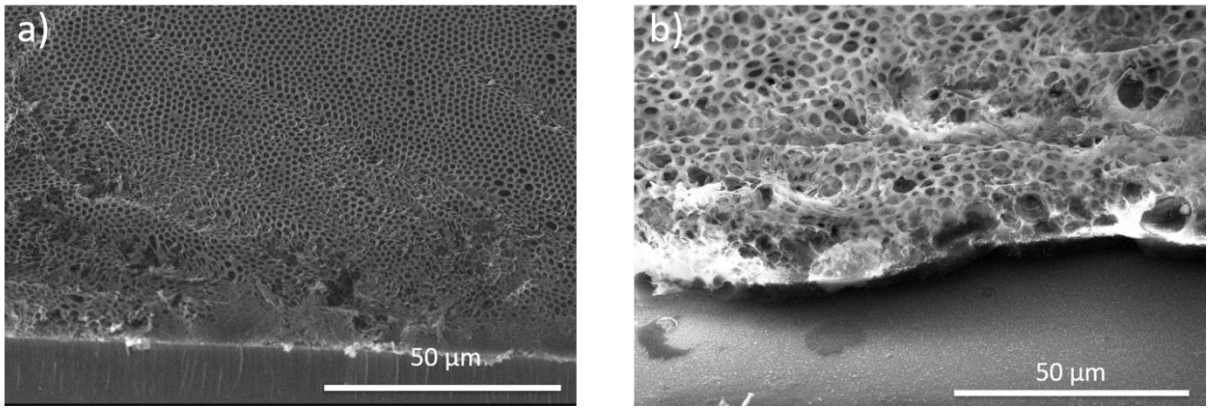

***Figure 4-4.** SEM imaging of copolymer membrane with average pore size of (a) 0.86 µm) and (b) 3.17 µm.*

Table 4-1 summarizes the extent to which the pore size can be varied, and the corresponding effect on the contact angle formed by a drop of water in contact with the copolymer film. The small variation of contact angle with respect to the change in porosity indicates that the hydrophobicity of the film remains nearly constant in this range of porosities.

***Table 4-1.** Impact of concentration of copolymer on the average pore size, contact angle and electrochemical performance*

CoPo Concentration (mg/ml)	5	6	7	8
Average Pore Size (µm)	1.17	1.66	2.02	3.17
Contact Angle (°)	99.1	101.8	93.1	94.0

The impact of the copolymer membranes on the stability and activity of the CO_2 reduction catalysts were first assessed on copper oxide. The extent to which the membrane protects against delamination was first assessed *via* linear sweep voltammetry in N_2- and CO_2-saturated bicarbonate solution and secondly *via* controlled potential chronoamperometry in a CO_2-saturated bicarbonate solution, as shown in **Figure 4-6**. Further quantification of the adducts formed during the experiments allowed assessing the impact of the copolymer on the CO2RR selectivity. Stability assays carried out on typical CuO and Cu_2O showed that the membranes were extremely efficient in extending the lifetime of the catalyst layers. Indeed, the mere presence of the copolymer membrane on top of the copper oxide catalyst thin film rendered the latter completely stable against delamination over a long period of time (typically hours), and over a wide range of electrolysis potentials. **Figure 4-6b)** shows typical chronoamperogram carried out at a potential of -0.75 V vs RHE, in which the CuO catalyst underwent sustained electrolytic conditions for 2 hours without notable decrease in rate. This stark increase in stability is apparent from the stable electrolysis current, showing no significant decrease over time. A very similar trend is followed by ITO substrates with Cu2O catalysts films, as well as with thermally evaporated thin layers (150 nm) of metal catalysts on top of ITO, such as Gold. The metal was shown to delaminate almost instantly when no copolymer membrane is present on top of it, while the gold thin film remains in close contact with the ITO surface throughout the electrolysis when the copolymer membrane is present. The impact of pore size was swiftly investigated by depositing membranes layers on top of identical CuO substrates. The pore size, and therefore the overall porosity, could be tuned to some extent, by varying the concentration of the PMMA-*b*-P4VP copolymer used for casting the membranes, as shown previously in **Table 4-1**. It was found that a range between 2.5 g/L and 8 g/L is the stable range for pore size, since at the ends of this range the copolymer membranes fails in protecting the copper oxide thin films and suffers delamination. The quantification of the CO2RR was carried out in identical conditions of time, applied potential, and electrolyte compositions as in earlier experiments (See Annex A for more information).

Table 4-2 reports the faradaic efficiencies of H_2 and CO for different pore sizes, corresponding to the average size of the pores measure by top-view SEM

images. The table shows a clear trend where the selectivity shifts towards CO upon increasing pore size, reaching a sweet spot at average pore size of 2 microns. The selectivity towards CO decreases for porosity values above 2 microns. Due to the more uniform morphology and the greater current density achieved by the membrane with average pore size of 1.66 microns, this was the one selected to continue to be study.

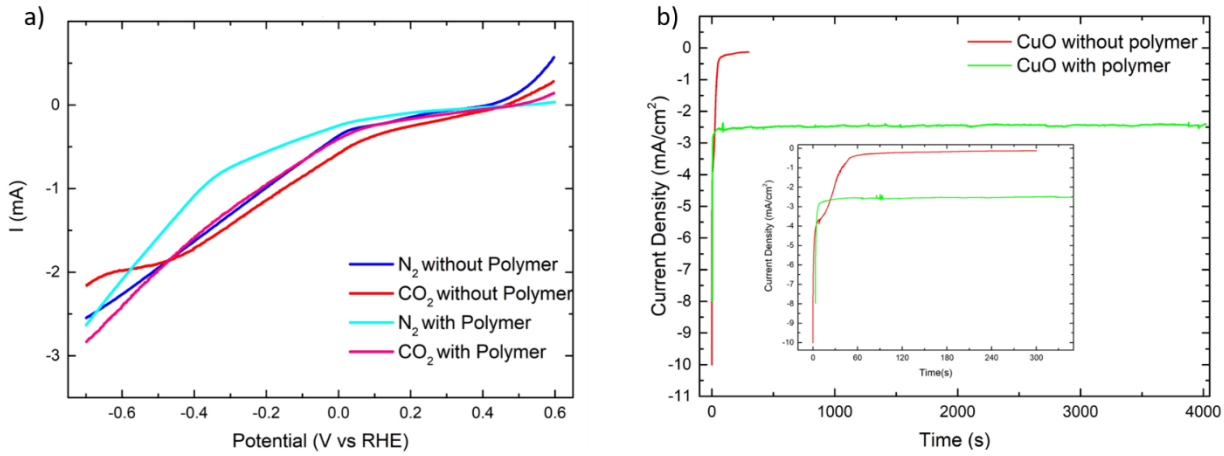

***Figure 4-6**. (a) Linear sweep voltammetries conducted with a 100 mV scanrate in a azote or a CO_2 saturated electrolyte of 0.5 M $KHCO_3$ and (b) chronoamperometries of substrates with and without the polymeric membrane on top conducted at -0.75 V vs RHE.*

Further quantification of the reduction adducts from the electrolysis cell head-space showed, to our surprise, a drastic shift in selectivity with respect to experiments carried out without the copolymer membrane. Indeed, while bare copper oxide produced an overwhelming amount of H_2, when covered with a thick, porous membrane as that of **Figure 4-5**, the selectivity of the reaction shifts towards CO to a great extent. Quite surprisingly, a shift in selectivity of a very similar magnitude was observed on all different types of copper oxide thin films tested in this study, namely, CuO, Cu_2O, carbon dopped-Cu_2O. The structural characteristics of each type of oxide is described in detail in **Chapter 3**, nevertheless, **Figure 4-7** shows that all three types of oxides yield mostly H_2 under electrocatalytic conditions (-0.75 V vs RHE) in CO_2, while they produce mostly CO when protected with the porous membrane. The fact that the final CO:H_2 ratio is

very similar in all cases is evidence that the shift in selectivity can be attributed to the porous membrane.

The trend observed herein corroborates the assumption according to which the selectivity towards carbon-based adducts is a consequence of the copolymer playing an active role in mediating the kinetics of both competing CO2RR and hydrogen evolution reaction (HER). It seems however that the mediating effect is not linked to the energetics of the chemical process, since there is no expected change in intrinsic physical properties of the copolymer with respect to the pore size. This is further confirmed by contact angle measurements carried out on the membranes described above, confirming that hydrophobicity of the layer is seen virtually constant regardless of the average pore size.

***Table 4-2**. Influence of pore size on selectivity.*

CoPo Concentration (mg/ml)	**2.5**	**5**	**6**	**7**	**8**
Average Pore Size (µm)	0.86	1.17	1.66	2.02	3.17
Current Density (mA/cm^2)	3.33	1.29	2.25	1.36	0.71
H2 F.E. (%)	49.23	40.59	68.72	34.06	38.6
Co F.E. (%)	20.09	33.82	13.11	40.49	14.34
CH4 F.E. (%)	0	0	0	0	0
C2+ F.E. (%)	0	0	0	0	0

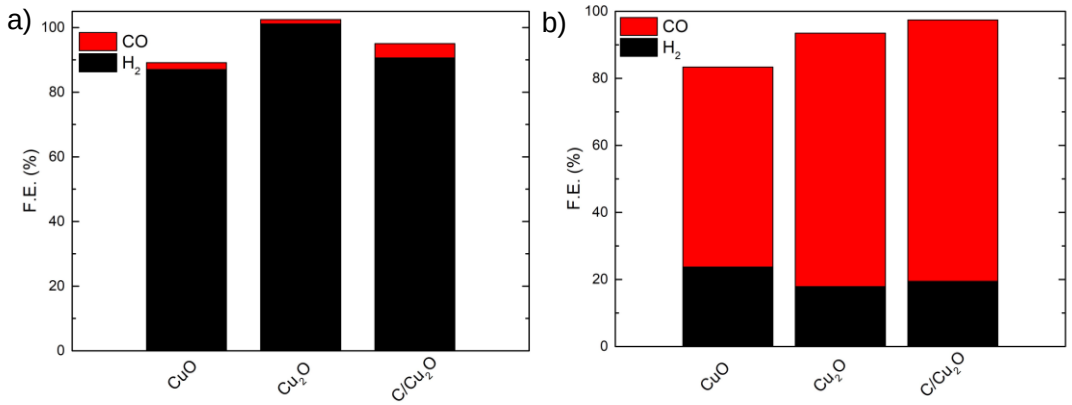

***Figure 4-7**. a) histogram depicting the faradic efficiency of CuO, lightly-doped (carbon) Cu2O and heavily doped (carbon) Cu2O. a) bare copper oxide films on ITO; b) copper oxide films on ITO with a top copolymer membrane deposited via the breath figure approach performed at -0.75 V (vs RHE) in 0.5 M $KHCO_3$.*

Interestingly, the shift in selectivity is not instantaneous, as it requires several minutes of continuous electrolysis to reach the optimum CO:H_2 ratio. **Figure 4-8** shows that the catalyst/polymer system reach equilibrium after two chronoamperometry cycles carried out at -0.75V (vs RHE) for 30 min each, with a final (CO:H_2) ratio of H_2:CO close to 1:4. This behaviour is similar for both types of oxides, however, the shift is more obvious for CuO species, which produces very little CO during the first run, rather than Cu_2O which produces an already significant amount from the first run. Based on our earlier studies on copper oxide catalyst (Chapter 3) and evidence from the corresponding chronoamperogram, it arises that the cycling effect is likely the result of a morphological or structural change of the copper oxide thin films, explaining the slight difference in behaviour observed when comparing CuO with Cu_2O. This indicates a reduction to Cu (O) at the surface, which is faster when starting from Cu (I) than from Cu (II).

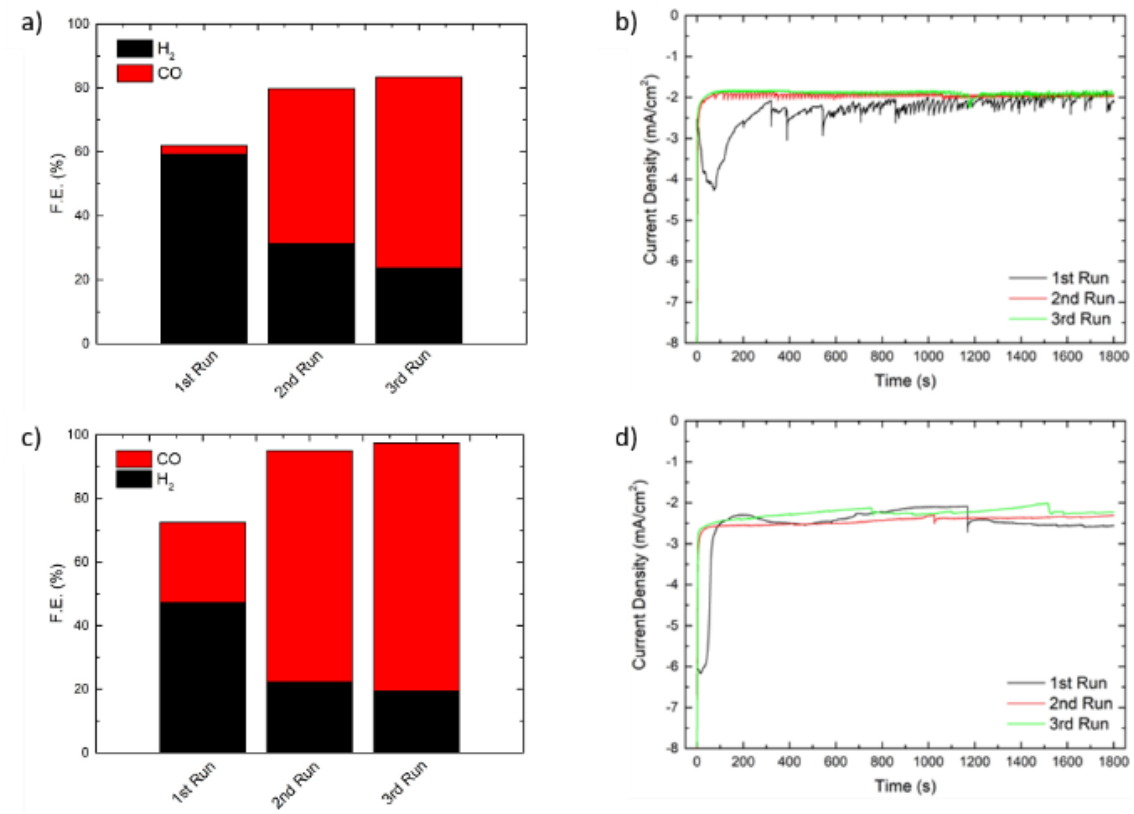

***Figure 4-8**. Histograms depicting the shift in selectivity upon cycling both CuO (a) and Cu_2O (c) catalyst via chronoamperometry experiments and their respective chronoamperogram (30 min.) in $KHCO_3$ (0.5M) at -0.75 V (vs RHE).*

4.2.2 Electrochemical pH study

To see if the protonation state and/or the wettability of the copolymer had an impact on how the copolymer shifts the electrode selectivity from H_2 towards CO, CuO thin film electrodes with a PMMA-b-P4VP mesoporous layer on top (6 mg/ml) were used on electrocatalytic reactions at -0.75 V vs RHE for 30 minutes. These reactions occurred the various potassium buffer electrolytes with pH ranging from 2.7 to 8.0. As we see by the selectivity evolution from acidic to neutral pH in **Figure 4-9**, at 4.1 and bellow the major product is H_2, with only small traces of CO being detected. When we started to move to less acidic pH (5.5), the selectivity shifted to equal parts H_2 and CO and when we reached pH 8.0, which is very similar to the pH of the potassium bicarbonate used as electrolyte throughout the rest of the experiments, we observed the same selectivity behaviour. With this study, it can be concluded that the hydrophobicity of the copolymer is necessary for the selectivity shift. It is also important to note that there was no delamination in the more acidic mediums, showing that the protective function of the copolymer was not lost. In **Figure 4-10** it is displayed how the copolymer layer changes its visual properties (goes from being white to being transparent) when in contact with a solution with a pH bellow its pKa. This happens due to the fact that when the copolymer goes from being hydrophobic to hydrophilic the aqueous solution permeates through it whilst when it is hydrophobic there is no water permeation and thus there is no colour change. This is confirmed by the change in wettability observed in **Figure B 11** and **Figure B 12**, that shows that the contact angles vary from 101.8° at pH 7.0 to 82.0° at pH 4.14 to 68.9° at pH 2.0. In 2021, Marcasuzaa et al.[131] have shown this behaviour with a very similar copolymer (P(MMA-stat-S)-*b*-P4VP) that they analyse by sweeping the pH from 10 to 1 and observe a transition from a Cassie-Baxter model towards a model considering a partial water penetration into the pores below the P4VP pKa.

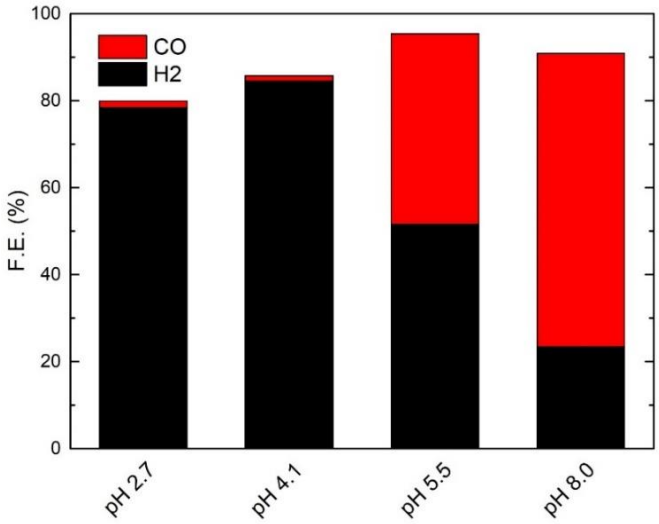

Figure 4-9. *pH influence in the **s**electivity of CuO thin film electrodes with a PMMA-b-P4VP mesoporous layer on top. Experience performed at -0.75 V (vs RHE) in 0.5 M $KHCO_3$.*

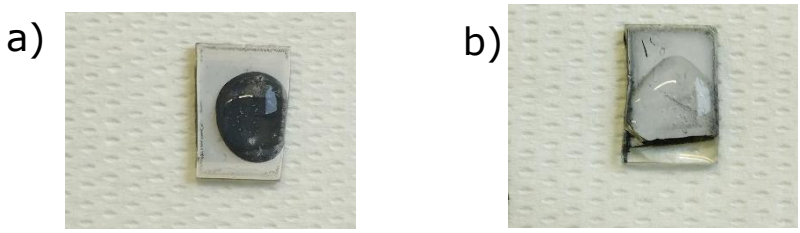

Figure 4-10. *Electrode with a drop of a) pH 2.7 and with a drop of b) pH 8.0.*

4.2.3 Effects of the membrane on different substrates

To confirm that the cycling effect is due to our copper electrode and to evaluate the real role of the honeycomb PMMA-*b*-P4VP film as gas diffusion, the copolymer was tested on different electrodes (copper and silver foil). These electrodes are fairly well known and were used on electrocatalytic tests with and without a copolymer layer on top. These electrocatalytic tests were performed for 10 minutes on a potential range varying from -0.6 to -1.4 V vs RHE in the case of silver foil and varying from -0.6 to -1.2 V vs RHE for copper foil. This disparity between ranges is due to limits on the gas quantification system, as copper foil at -1.4 V vs RHE was producing a volume of gas products that were much higher that the highest amount we had calibrated for. All these tests were repeated at least three times with different electrodes to guarantee their reproducibility.

Starting with the copper foil electrodes, before electrocatalytic testing or copolymer deposition they were subjected to two distinct cleanings. Part of the cooper foils were mechanically polished and afterwards washed with miliq water, acetone and isopropanol while the rest of the copper foil substrates were just subjected to the same solvent washing without any type of surface polishing. In **Figure 4-11** the selectivity of these two different subtracts, with and without the mesoporous copolymer film on top is shown.

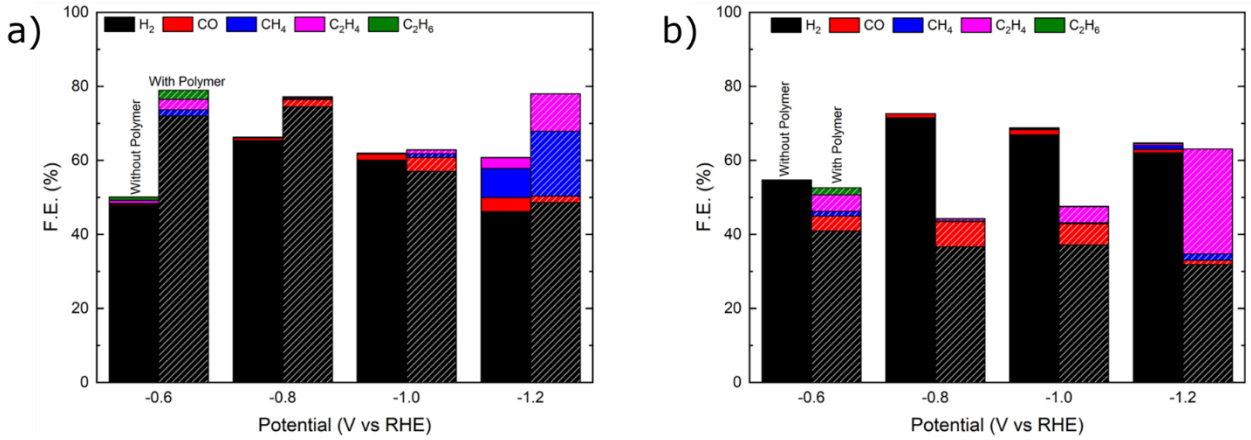

Figure 4-11. *Selectivity with and without copolymer of a) washed and b) mechanically polished copper foils.*

Analysing the performance of bare copper foil in terms of selectivity, it is observed that the copper foil that was only washed presents an overall lower selectivity for hydrogen production when compared to its polished counterpart but also a stronger activity towards CO2RR products, specially at the higher potential point (-1.2 V vs RHE), with the bare polished copper foil barely show any activity towards CO_2 reduction. When the copolymer is added to the electrodes, a major shift in behaviour is observed, showing the real potential applications of this mesoporous copolymer as a hydrogen suppressor and selectivity changer. In the case of washed copper foil, the copolymer improves the selectivity for CO2RR across the entire potential range as it does also for the polished copper foil. Moreover, while for the washed copper the H_2 selectivity in most cases improves, for the polished copper it is suppressed to half in most points. Also, at the highest point, the improvement of the selectivity for CO2RR is very significative, showing a more than 2-fold increase for

the washed copper foil and a very impressive 10-fold improvement for the polished copper, with a very high selectivity (~30% of the overall faradaic efficiency) for ethylene. One important reason for the change in activity of the two distinctly prepared copper foils can be explained to a failure to remove a passivation oxide layer on top of the copper foil just by washing it, whilst by mechanically polishing it we guarantee that such layers are gone. It is also important to consider that the overall faradaic efficiency of all these substrates are far from 100%. This disparity between charge and products can be explained by the production of liquid products, like formate or acetate, that were seen in the electrolyte at the end of the experiment but unfortunately were not quantified.

With silver foil electrodes, the same approach was applied, with the exception of the manual polishing. Silver foil electrodes were cleaned by solvent washing and tested with and without the mesoporous membrane on top, with the performance of these electrodes being showcased in **Figure 4-12**. The results observed with silver foil seems to contribute to the idea that just by washing the substrate without any kind of chemical or mechanical polishing, the activity is much weaker for both hydrogen evolution and CO2RR in the whole potential range, despite the lack of testing mechanically polished silver foils to really prove this theory (due unfortunately to a lack of time). From comparing the performance with and without the copolymer on top of the electrode, observe from this study was the improvement in CO selectivity (mostly between -1.0 and -1.2 V vs RHE) that the copolymer provided. These are similar results as seen previously in the copper oxide thin films and the copper foils and confirms that a mesoporous PMMA-*b*-P4VP gas diffusion membrane on top of an electrode for CO_2 electroreduction shifts the selectivity towards the reduction of CO_2 and causes HER suppression in most of the electrodes tested, excluding the silver and copper foil that were not subject to a throughout cleaning of their surface.

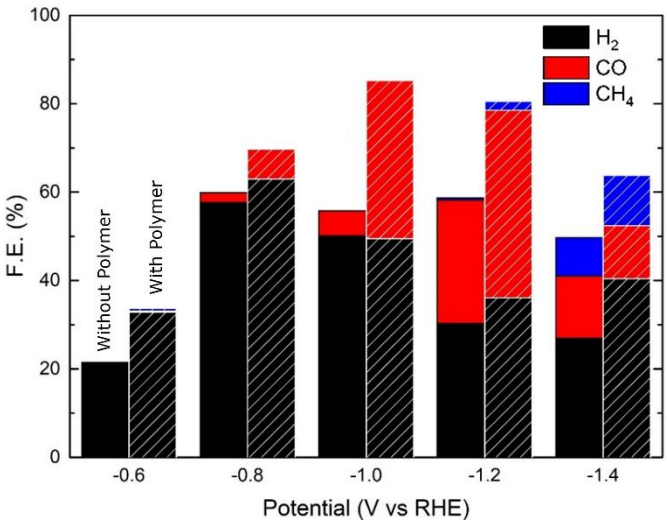

Figure 4-12. *Selectivity of silver foil electrodes with and without copolymer.*

4.3 Continuous film *vs* mesoporous membrane

A question left unanswered was the real impact of the morphology of the copolymer. Was a thick mesoporous gas diffusion layer necessary or a thin nanometric film of PMMA-*b*-P4VP would be as effective? Indeed, our group recently described the ability of a continuous film, as a functional coating, to tune the selectivity of molecular catalyst deposited onto a GDL, from H_2 to CO in water-based electrolyte[214].

To answer this question, deep coating of PMMA-*b*-P4VP was performed in order to deposit on the thin CuO/Cu_2O films and in silver foil. Four different film theoretical (See **Annex B**) thickness were tested: 7, 22, 49 and 70 nanometers. The thickness was controlled with the concentration of copolymer on dichloromethane (DCM) and on the withdrawal speed of the substrate from the solution.

When we moved for electrocatalysis, it was clear that as a continuous film the copolymer membrane did not retain its protective aspect and every CuO and Cu_2O thin film tested with the four different copolymer thicknesses delaminate almost instantaneously, making it impossible to test. On the other hand, since the silver foil has no stability issues and doesn't require the protective properties of the mesoporous copolymer, the study with it could proceed. **Figure 4-13** shows the faradaic efficiencies achieved by the four different electrodes for 10 minutes electrocatalysis under a potential bias ranging from -0.6 to -1.2 V vs RHE.

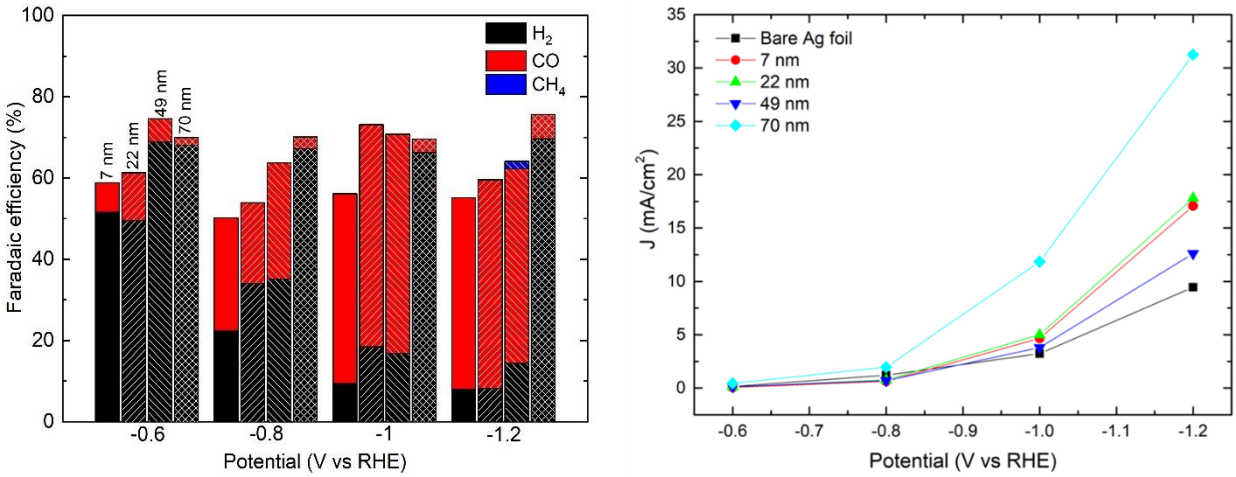

Figure 4-13. *Selectivity (left) and current density (right) of silver foil electrodes with thin copolymer films (7, 22, 49 and 70 nm) on top.*

This electrocatalytic characterization show that a low bias (-0.6 V vs RHE) the major product is H_2 for all the electrodes but as the bias is increased the selectivity shifts from H_2 to CO in all cases except for the electrode with a copolymeric thin film with 70 nm of thickness. This result show that the copolymer can be used as a thin layer, with best performance at a thickness of 7 nm, for reducing HER and promoting, for the case of silver electrodes, CO production. Looking at the behaviour observed with a 70 nm thick layer brought the conclusion that there is a maximum thickness when using the PMMA-*b*-P4VP copolymer as a thin film for shifting electrocatalysis from HER to CO2RR. This maximum limit could be explained by the thickness of the copolymer layer not allowing for the diffusion of CO_2 to the surface of the silver. There is also a huge increase in current density for the 70 nm electrode when compared to the others, which points to the Poly-4-VinylPyridine chains in the copolymer protonating and acting as proton exchange from the electrolyte to the electrodes surface. AFM characterization of the 7 nm, 22nm and 70 nm thick thin films was conducted (since the 22 nm and 49 nm had the same performance, the 49 nm thick film was excluded from this characterization) in order to observe if microphase segregation was occurring between the two polymeric block of the copolymer, creating in theory domains in the morphology of columns/cylinders, which would guarantee chains of P4VP going from the electrolyte to the surface, ensuring an open proton exchange nano-channel[130,215,216] when the P4VP is protonated (pH bellow its pKa). The results of the characterization are shown in

Figure 4-14 and it is observed that microphase separation occurs for all the thicknesses. With the 7 nm thickness showing cylindrical morphology in parallel with the surface, i.e. *in-the-plane*, therefore not creating channels of P4VP through the film, while the 22 and 70 nm show cylindrical structures as well but now perpendicular to the surface, i.e. *out-of-the-plane*, creating such conductive nano-channels. These findings support the high current seen in **Figure 4-15**, as these P4VP cylinders acting as proton exchange membranes by protonation of the pyridine in a potassium buffer electrolyte of pH 2.7, promoting HER. It is also notable the increase in faradaic efficiency and overall hydrogen production, which lead to the inability to reach a applied potential over -0.95V vs RHE due to limitations of the potentiostat (maximum applied bias between the working and the counter was achieved).

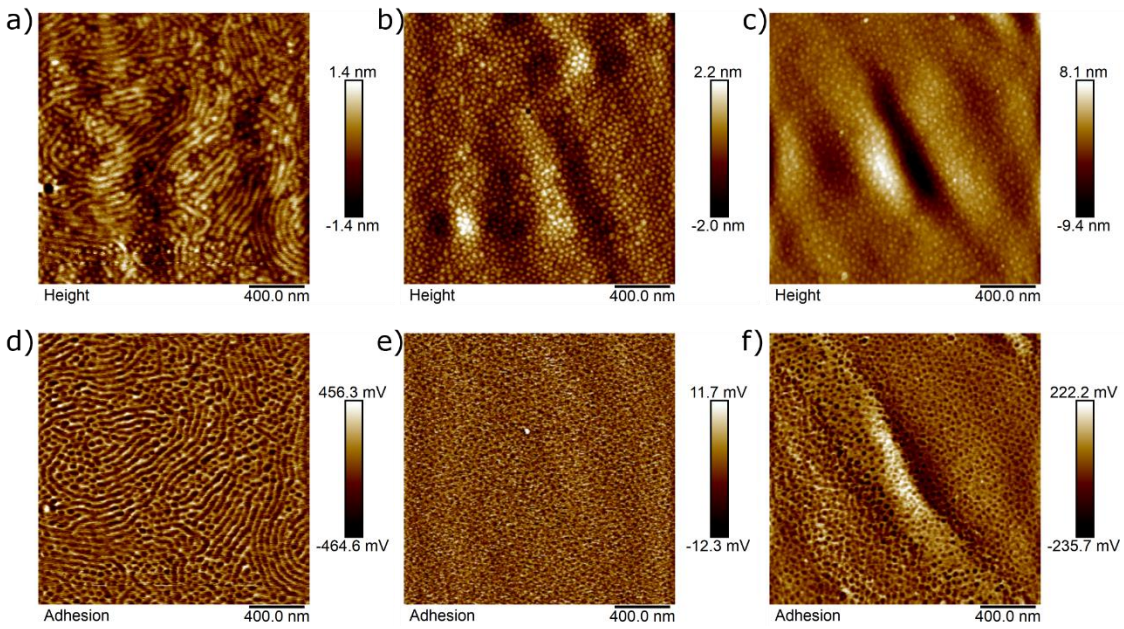

Figure 4-14. *AFM imaging of the copolymer thin films with 7 nm a) and d), 22 nm b) and e) and 70 nm c) and f) thicknesses.*

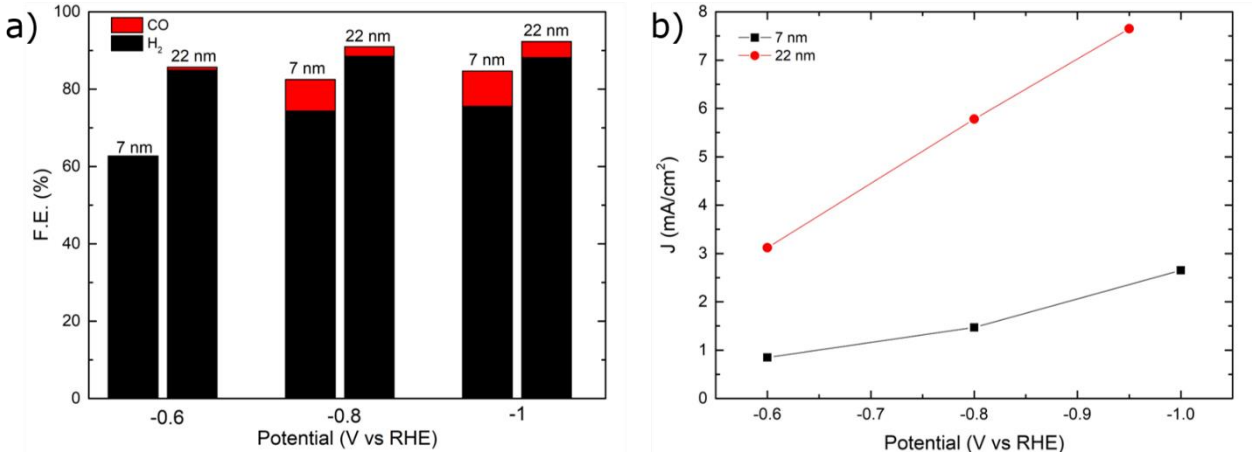

Figure 4-15. *Selectivity (left) and current density (right) of silver foil electrodes with thin copolymer films (7, 22) on top at pH 2.7.*

To close all these studies, it is presented in **Figure 4-16** a comparison between the bare silver foil electrode, the silver foil electrode with a 7 nm thick film of our PMMA-*b*-P4VP and the silver foil electrode with a mesoporous layer of the same copolymer. Amongst the three, the electrode that presents the best selectivity towards CO is the thin film one, although the mesoporous one also presents better CO2RR performance when compared to the blank one and it is the one that produces the most methane of all.

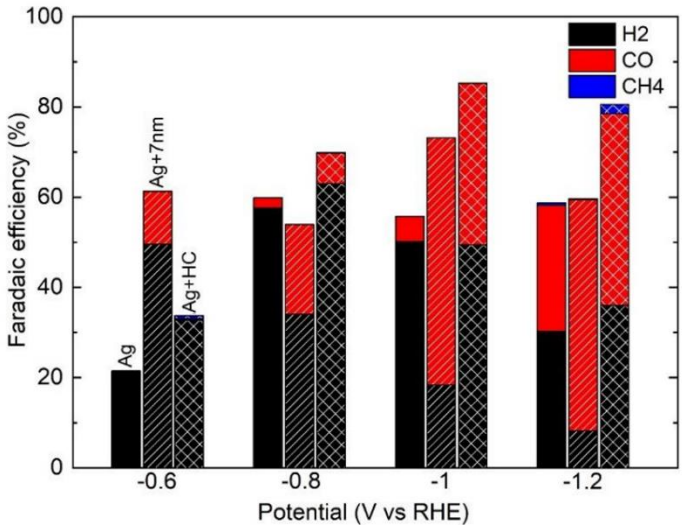

Figure 4-16. *Faradaic efficiency of bare silver foil vs silver foil with the polymeric mesoporous gas diffusion layer on top vs silver foil with a 7nm copolymer continuous 7 nm thick film.*

4.4 Conclusion

To conclude, a PMMA-*b*-P4VP block copolymer with a ratio of 78:22 has been developed as a protective layer for copper oxide thin film electrodes. This protective layer was created via the breath figure methodology, which allowed for a mesoporous polymeric layer that has tunable porosity. PMMA and P4VP were chosen as the monomers due to the fact that a block copolymer of the two would be eligible for the breath figure method and the copolymer would be hydrophobic. Afterwards, it was demonstrated that this layer not only protected the copper oxide thin films from delamination during electrocatalysis but also significantly altered the product selectivity of the electrocatalysis. With this copolymer on top of the electrodes CO was nearly 80% of the products observed, with differs with the results showed in **Chapter 3** of the bare electrodes, that were almost only producing H_2. After seeing these results, a deeper study of the copolymer was conducted using different substrates (copper and silver foils) and again with the addiction of the copolymer, as a mesoporous layer on top of the electrodes, a shift on the selectivity towards CO2RR and suppression of HER was observed. The copolymer was lastly tested as a thin film instead of a mesoporous layer and better results for CO2RR were observed but these thin films lost their protective capacity and when applied to the copper oxide electrodes delamination was not prevented. Nevertheless, these continuous films were used with silver electrodes and not only better results were achieved in terms of CO selectivity in neutral pH but the copolymer presents an extreme shift in selectivity towards HER at pH 2.7 due to the self-assembly of proton exchange nano-channels of P4VP. To conclude, this copolymer can be applied as a thin film to stable electrocatalysts to modify their selectivity during CO_2 electrocatalysis and can be applied as a mesoporous layer to unstable electrodes, not only to perform as a selectivity tuner but also to act as a stabilizing layer.

5 Final remarks and future outlook

The body of work presented in this Thesis has demonstrated a simple synthesis of copper oxide thin films that can be applied to electrocatalysts for the CO2RR. These copper oxide oxidation state can be tuned by changing the calcination atmosphere (CuO in air and Cu_2O in N_2) and can be easily alloyed to form bimetallic oxide films. Within this work we also studied the use of a block copolymer of PMMA and P4VP as a tunable mesoporous top layer of the electrodes that can protect and shift their selectivity towards CO2RR (performing HER suppression) and as a thin film which as the same properties of its mesoporous counterpart except for the protective aspect.

In **Chapter 2**, a brief description of the synthetic and characterization methodologies applied over the course of the Thesis work was provided, giving an insight on each technique used.

In **Chapter 3**, the synthesis of the copper oxide electrodes is explained in detail, describing the simple and cost-effective synthesis process and the thorough characterization performed to understand the mechanisms responsible for the formation of the CuO and Cu_2O. The chapter shows a sol-gel method that can produce both cupric and cuprous oxide from a single precursor by controlling the atmosphere during pyrolysis (CuO in air and Cu_2O in N_2). Interestingly, varying the flow of nitrogen during the pyrolysis results in Cu_2O films with different characteristics. The resulting films show no doping (CuO) to significant doping (Cu_2O) of carbon and nitrogen, which affects their band gap, electrical properties, and photocatalytic activity. However, the films tend to delaminate under certain electrolytic conditions, which limits their use in electrochemical catalysis. The study found that all three types of copper oxide exhibited similar activity towards CO2 reduction, with modest CO faradic efficiencies, before delamination.

In **Chapter 4**, we discuss the use of a PMMA-*b*-P4VP block copolymer as a protective layer for copper oxide thin film electrodes. The breath figure methodology was used to create a mesoporous polymeric layer that is tunable in porosity. The protective layer not only prevented delamination of the copper oxide thin films during electrocatalysis but also significantly altered the product selectivity of the

electrocatalysis towards CO, as opposed to H_2 which was the main product without it. Further studies were conducted on copper and silver foils, which showed a shift towards CO2RR and suppression of HER with the addition of the copolymer as a mesoporous layer on top of the electrodes. The copolymer was also tested as a thin film instead of a mesoporous layer, which showed better results for CO2RR but the thin films lost their protective capacity when applied to the copper oxide electrodes, resulting in delamination during electrocatalysis. Overall, the copolymer can be applied as a thin film to stable electrocatalysts to modify their selectivity towards CO2RR and suppress HER, and can be applied as a mesoporous layer to unstable electrodes to not only perform as a selectivity tuner but also act as a stabilizing layer to prevent delamination.

The assembly of a laboratory with capacity to carry out electrocatalytic reactions and measure the products of such reactions was a significant part of the PhD work, as the team had to work together in order to have a working and optimised setup. On this basis, the PhD student assisted others in setting up of an automatic cell to GC-MS system that can perform electro and photoelectrocatalysis in a cell with a direct connection to the GC-MS apparatus, which guarantees a very high degree of accuracy for the detection of products. This setup is described with more detail in **Chapter 2**. This work marks the first PhD thesis of the INTERMAT group.

5.1 Future outlook

In the future, these findings could and should be applied in CO_2 and water reduction, via photo, electro or photoelectrocatalysis. The copper oxide thin films describe in this work were fabricated on ITO substrates for use in photocatalysis, which unfortunately was not carried out by this work due to time constraints, and therefore we believe it should the electrodes should be tested under those conditions. These films also show electric and optical properties that indicate a potential for photovoltaic applications.

Another study that shows great potential is the bimetallic copper-metal (Ag, Ce, Zn) oxide alloys, which were showed to be easily fabricated but were not tested for catalytic performance. As seen in similar studies in literature, the addition of other metallic centers to our copper oxide electrode could shift the selectivity towards C_{2+} products.

The PMMA-*b*-P4VP block copolymer has been describe as working as a selectivity tuner and a proton exchange layer. This copolymer or other with similar behaviour and characteristics should be studied more in depth for various applications in electrochemistry, from being used as part of the electrode for water splitting or for CO2RR to potentially being used as a cell membrane or as a binder for the electrode materials. It is our opinion that this area of study can make a big impact on the field of CO_2 catalysis and therefore is the most critical topic to further investigate.

References

(1) Johan Rockström; Will Steffen; Kevin Noone; Asa Persson; F. Stuart Chapin III; Eric F. Lambin; Timothy M. Lenton; Marten Scheffer; Carl Folke; Hans Joachim Schellnhuber; Björn Nykvist; Cynthia A. de Wit; Terry Hughes; Sander van der Leeuw; Henning Rodhe; Sverker Sörlin; Peter K. Snyder; Robert Costanza; Uno Svedin; Malin Falkenmark; Louise Karlberg; Robert W. Corell; Victoria J. Fabry; James Hansen; Brian Walker; Diana Liverman; Katherine Richardson; Paul Crutzen; Jonathan A. Foley. A Safe Operating Space for Humanity. *Nature* **2009**, No. 461, 472–475. https://doi.org/10.1038/461472a.

(2) Endrődi, B.; Bencsik, G.; Darvas, F.; Jones, R.; Rajeshwar, K.; Janáky, C. Continuous-Flow Electroreduction of Carbon Dioxide. *Prog. Energy Combust. Sci.* **2017**, *62*, 133–154. https://doi.org/10.1016/j.pecs.2017.05.005.

(3) IPCC. *IPCC Special Report on Global Warming of 1.5°C. Technical Report 5813*; 5813; IPCC, 2018. https://www.ipcc. ch/site/assets/uploads/sites/2/2019/06/SR15_Full_Report_High_Res.pdf.

(4) El-Khouly, M. E.; El-Mohsnawy, E.; Fukuzumi, S. Solar Energy Conversion: From Natural to Artificial Photosynthesis. *J. Photochem. Photobiol. C Photochem. Rev.* **2017**, *31*, 36–83. https://doi.org/10.1016/j.jphotochemrev.2017.02.001.

(5) Bonke, S. A.; Wiechen, M.; MacFarlane, D. R.; Spiccia, L. Renewable Fuels from Concentrated Solar Power: Towards Practical Artificial Photosynthesis. *Energy Environ. Sci.* **2015**, *8* (9), 2791–2796. https://doi.org/10.1039/C5EE02214B.

(6) Beller, J.-N.; Beller, M. Spiers Memorial Lecture : Artificial Photosynthesis: An Introduction. *Faraday Discuss.* **2019**, *215*, 9–14. https://doi.org/10.1039/C9FD90025J.

(7) Qiao, J.; Liu, Y.; Zhang, J. Electrochemical Reduction of Carbon Dioxide: Fundamentals and Technologies. 396.

(8) Dalle, K. E.; Warnan, J.; Leung, J. J.; Reuillard, B.; Karmel, I. S.; Reisner, E. Electro- and Solar-Driven Fuel Synthesis with First Row Transition Metal Complexes. *Chem. Rev.* **2019**, *119* (4), 2752–2875. https://doi.org/10.1021/acs.chemrev.8b00392.

(9) Gattrell, M.; Gupta, N.; Co, A. A Review of the Aqueous Electrochemical Reduction of CO2 to Hydrocarbons at Copper. *J. Electroanal. Chem.* **2006**, *594* (1), 1–19. https://doi.org/10.1016/j.jelechem.2006.05.013.

(10) Yaashikaa, P. R.; Senthil Kumar, P.; Varjani, S. J.; Saravanan, A. A Review on Photochemical, Biochemical and Electrochemical Transformation of CO2 into Value-Added Products. *J. CO2 Util.* **2019**, *33*, 131–147. https://doi.org/10.1016/j.jcou.2019.05.017.

(11) Albero, J.; Peng, Y.; García, H. Photocatalytic CO $_2$ Reduction to C2+ Products. *ACS Catal.* **2020**, *10* (10), 5734–5749. https://doi.org/10.1021/acscatal.0c00478.

(12) Baran, T.; Visibile, A.; Busch, M.; He, X.; Wojtyla, S.; Rondinini, S.; Minguzzi, A.; Vertova, A. Copper Oxide-Based Photocatalysts and Photocathodes: Fundamentals and Recent Advances. *Molecules* **2021**, *26* (23), 7271. https://doi.org/10.3390/molecules26237271.

(13) Stolarczyk, J. K.; Bhattacharyya, S.; Polavarapu, L.; Feldmann, J. Challenges and Prospects in Solar Water Splitting and CO $_2$ Reduction with Inorganic and Hybrid Nanostructures. *ACS Catal.* **2018**, *8* (4), 3602–3635. https://doi.org/10.1021/acscatal.8b00791.

(14) Zhang, B.; Sun, L. Artificial Photosynthesis: Opportunities and Challenges of Molecular Catalysts. *Chem. Soc. Rev.* **2019**, *48* (7), 2216–2264. https://doi.org/10.1039/C8CS00897C.

(15) Apaydin, D. H.; Tordin, E.; Portenkirchner, E.; Aufischer, G.; Schlager, S.; Weichselbaumer, M.; Oppelt, K.; Sariciftci, N. S. Photoelectrochemical Reduction of CO $_2$ Using Third-Generation Conjugated Polymers. *ChemistrySelect* **2016**, *1* (6), 1156–1162. https://doi.org/10.1002/slct.201600326.

(16) Department of Environmental Science and Engineering, Beijing University of Chemical Technology, Beijing 100029, P. R. China; Yuan, J. Photoelectrochemical Reduction of Carbon

Dioxide to Ethanol at Cu2O Foam Cathode. *Int. J. Electrochem. Sci.* **2017**, 8288–8294. https://doi.org/10.20964/2017.09.36.

(17) Louis, H.; Akakuru, O. U.; Monday, P.; Funmilayo, O. O. A Review on the State-of-the-Art Advances for CO2 Electro-Chemical Reduction Using Metal Complex Molecular Catalysts. *Eclética Quím. J.* **2019**, *44* (1), 11. https://doi.org/10.26850/1678-4618eqj.v44.1.2019.p11-39.

(18) Popović, S.; Smiljanić, M.; Jovanovič, P.; Vavra, J.; Buonsanti, R.; Hodnik, N. Stability and Degradation Mechanisms of Copper-Based Catalysts for Electrochemical CO_2 Reduction. *Angew. Chem. Int. Ed.* **2020**, *59* (35), 14736–14746. https://doi.org/10.1002/anie.202000617.

(19) Zhang, R.-Z.; Wu, B.-Y.; Li, Q.; Lu, L.-L.; Shi, W.; Cheng, P. Design Strategies and Mechanism Studies of CO2 Electroreduction Catalysts Based on Coordination Chemistry. *Coord. Chem. Rev.* **2020**, *422*, 213436. https://doi.org/10.1016/j.ccr.2020.213436.

(20) Vasileff, A.; Xu, C.; Jiao, Y.; Zheng, Y.; Qiao, S.-Z. Surface and Interface Engineering in Copper-Based Bimetallic Materials for Selective CO2 Electroreduction. *Chem* **2018**, *4* (8), 1809–1831. https://doi.org/10.1016/j.chempr.2018.05.001.

(21) Wang, Y.; Liu, J.; Wang, Y.; Al-Enizi, A. M.; Zheng, G. Tuning of CO_2 Reduction Selectivity on Metal Electrocatalysts. *Small* **2017**, *13* (43), 1701809. https://doi.org/10.1002/smll.201701809.

(22) Zhang, W.; Hu, Y.; Ma, L.; Zhu, G.; Wang, Y.; Xue, X.; Chen, R.; Yang, S.; Jin, Z. Progress and Perspective of Electrocatalytic CO_2 Reduction for Renewable Carbonaceous Fuels and Chemicals. *Adv. Sci.* **2018**, *5* (1), 1700275. https://doi.org/10.1002/advs.201700275.

(23) Zhu, D. D.; Liu, J. L.; Qiao, S. Z. Recent Advances in Inorganic Heterogeneous Electrocatalysts for Reduction of Carbon Dioxide. *Adv. Mater.* **2016**, *28* (18), 3423–3452. https://doi.org/10.1002/adma.201504766.

(24) Bagger, A.; Ju, W.; Varela, A. S.; Strasser, P.; Rossmeisl, J. Electrochemical CO_2 Reduction: A Classification Problem. *ChemPhysChem* **2017**, *18* (22), 3266–3273. https://doi.org/10.1002/cphc.201700736.

(25) Ren, D.; Gao, J.; Zakeeruddin, S. M.; Grätzel, M. Bimetallic Electrocatalysts for Carbon Dioxide Reduction. *CHIMIA* **2019**, *73* (11), 928. https://doi.org/10.2533/chimia.2019.928.

(26) Wang, Z.; She, X.; Yu, Q.; Zhu, X.; Li, H.; Xu, H. Minireview on the Commonly Applied Copper-Based Electrocatalysts for Electrochemical CO_2 Reduction. *Energy Fuels* **2021**, *35* (10), 8585–8601. https://doi.org/10.1021/acs.energyfuels.1c00700.

(27) Zhao, J.; Xue, S.; Barber, J.; Zhou, Y.; Meng, J.; Ke, X. An Overview of Cu-Based Heterogeneous Electrocatalysts for CO_2 Reduction. *J. Mater. Chem. A* **2020**, *8* (9), 4700–4734. https://doi.org/10.1039/C9TA11778D.

(28) Hansen, H. A.; Shi, C.; Lausche, A. C.; Peterson, A. A.; Nørskov, J. K. Bifunctional Alloys for the Electroreduction of CO_2 and CO. *Phys. Chem. Chem. Phys.* **2016**, *18* (13), 9194–9201. https://doi.org/10.1039/C5CP07717F.

(29) Hori, Y.; Murata, A.; Takahashi, R. Formation of Hydrocarbons in the Electrochemical Reduction of Carbon Dioxide at a Copper Electrode in Aqueous Solution. *J. Chem. Soc. Faraday Trans. 1 Phys. Chem. Condens. Phases* **1989**, *85* (8), 2309. https://doi.org/10.1039/f19898502309.

(30) Hori, Y.; Wakebe, H.; Tsukamoto, T.; Koga, O. Electrocatalytic Process of CO Selectivity in Electrochemical Reduction of CO2 at Metal Electrodes in Aqueous Media. *Electrochimica Acta* **1994**, *39* (11–12), 1833–1839. https://doi.org/10.1016/0013-4686(94)85172-7.

(31) Hori, Y.; Takahashi, R.; Yoshinami, Y.; Murata, A. Electrochemical Reduction of CO at a Copper Electrode. *J. Phys. Chem. B* **1997**, *101* (36), 7075–7081. https://doi.org/10.1021/jp970284i.

(32) Kim, D.; Kley, C. S.; Li, Y.; Yang, P. Copper Nanoparticle Ensembles for Selective Electroreduction of CO_2 to C_2–C_3 Products. *Proc. Natl. Acad. Sci.* **2017**, *114* (40), 10560–10565. https://doi.org/10.1073/pnas.1711493114.

(33) Kuhl, K. P.; Cave, E. R.; Abram, D. N.; Jaramillo, T. F. New Insights into the Electrochemical Reduction of Carbon Dioxide on Metallic Copper Surfaces. *Energy Environ. Sci.* **2012**, *5* (5), 7050. https://doi.org/10.1039/c2ee21234j.

(34) Li, C. W.; Ciston, J.; Kanan, M. W. Electroreduction of Carbon Monoxide to Liquid Fuel on Oxide-Derived Nanocrystalline Copper. *Nature* **2014**, *508* (7497), 504–507. https://doi.org/10.1038/nature13249.
(35) Kortlever, R.; Shen, J.; Schouten, K. J. P.; Calle-Vallejo, F.; Koper, M. T. M. Catalysts and Reaction Pathways for the Electrochemical Reduction of Carbon Dioxide. *J. Phys. Chem. Lett.* **2015**, *6* (20), 4073–4082. https://doi.org/10.1021/acs.jpclett.5b01559.
(36) Calle-Vallejo, F.; Koper, M. T. M. Theoretical Considerations on the Electroreduction of CO to C $_2$ Species on Cu(100) Electrodes. *Angew. Chem. Int. Ed.* **2013**, *52* (28), 7282–7285. https://doi.org/10.1002/anie.201301470.
(37) Li, H.; Li, Y.; Koper, M. T. M.; Calle-Vallejo, F. Bond-Making and Breaking between Carbon, Nitrogen, and Oxygen in Electrocatalysis. *J. Am. Chem. Soc.* **2014**, *136* (44), 15694–15701. https://doi.org/10.1021/ja508649p.
(38) Varela, A. S.; Ju, W.; Reier, T.; Strasser, P. Tuning the Catalytic Activity and Selectivity of Cu for CO $_2$ Electroreduction in the Presence of Halides. *ACS Catal.* **2016**, *6* (4), 2136–2144. https://doi.org/10.1021/acscatal.5b02550.
(39) Verdaguer-Casadevall, A.; Li, C. W.; Johansson, T. P.; Scott, S. B.; McKeown, J. T.; Kumar, M.; Stephens, I. E. L.; Kanan, M. W.; Chorkendorff, I. Probing the Active Surface Sites for CO Reduction on Oxide-Derived Copper Electrocatalysts. *J. Am. Chem. Soc.* **2015**, *137* (31), 9808–9811. https://doi.org/10.1021/jacs.5b06227.
(40) Schouten, K. J. P.; Kwon, Y.; van der Ham, C. J. M.; Qin, Z.; Koper, M. T. M. A New Mechanism for the Selectivity to C1 and C2 Species in the Electrochemical Reduction of Carbon Dioxide on Copper Electrodes. *Chem. Sci.* **2011**, *2* (10), 1902. https://doi.org/10.1039/c1sc00277e.
(41) Peterson, A. A.; Abild-Pedersen, F.; Studt, F.; Rossmeisl, J.; Nørskov, J. K. How Copper Catalyzes the Electroreduction of Carbon Dioxide into Hydrocarbon Fuels. *Energy Environ. Sci.* **2010**, *3* (9), 1311. https://doi.org/10.1039/c0ee00071j.
(42) Montoya, J. H.; Shi, C.; Chan, K.; Nørskov, J. K. Theoretical Insights into a CO Dimerization Mechanism in CO $_2$ Electroreduction. *J. Phys. Chem. Lett.* **2015**, *6* (11), 2032–2037. https://doi.org/10.1021/acs.jpclett.5b00722.
(43) Schouten, K. J. P.; Qin, Z.; Pérez Gallent, E.; Koper, M. T. M. Two Pathways for the Formation of Ethylene in CO Reduction on Single-Crystal Copper Electrodes. *J. Am. Chem. Soc.* **2012**, *134* (24), 9864–9867. https://doi.org/10.1021/ja302668n.
(44) Schouten, K. J. P.; Pérez Gallent, E.; Koper, M. T. M. The Influence of PH on the Reduction of CO and CO 2 to Hydrocarbons on Copper Electrodes. *J. Electroanal. Chem.* **2014**, *716*, 53–57. https://doi.org/10.1016/j.jelechem.2013.08.033.
(45) Xiao, Y.; Chen, B.-L.; Yang, H.-P.; Wang, H.; Lu, J.-X. Electrosynthesis of Enantiomerically Pure Cyclic Carbonates from CO2 and Chiral Epoxides. *Electrochem. Commun.* **2014**, *43*, 71–74. https://doi.org/10.1016/j.elecom.2014.03.012.
(46) Asiri, A. M.; Gao, J.; Khan, S. B.; Alamry, K. A.; Marwani, H. M.; Khan, M. S. J.; Adeosun, W. A.; Zakeeruddin, S. M.; Ren, D.; Grätzel, M. Revisiting the Impact of Morphology and Oxidation State of Cu on CO $_2$ Reduction Using Electrochemical Flow Cell. *J. Phys. Chem. Lett.* **2022**, *13* (1), 345–351. https://doi.org/10.1021/acs.jpclett.1c03957.
(47) Windle, C. D.; Perutz, R. N. Advances in Molecular Photocatalytic and Electrocatalytic CO2 Reduction. *Coord. Chem. Rev.* **2012**, *256* (21–22), 2562–2570. https://doi.org/10.1016/j.ccr.2012.03.010.
(48) Li, C.; Chen, K.; Wang, X.; Xue, N.; Yang, H. Understanding the Role of Cu/ZnO Interaction in CO_2 Hydrogenation to Methanol. *Acta Phys. Chim. Sin.* **2020**, *0* (0), 2009101–0. https://doi.org/10.3866/PKU.WHXB202009101.
(49) Branco, J. B.; Ferreira, A. C.; Vieira, F.; Martinho, J. F. Cerium-Based Bimetallic Oxides as Catalysts for the Methanation of CO $_2$: Influence of the Preparation Method. *Energy Fuels* **2021**, *35* (8), 6725–6737. https://doi.org/10.1021/acs.energyfuels.1c00030.

(50) Dongare, S.; Singh, N.; Bhunia, H.; Bajpai, P. K. Electrochemical Reduction of CO2 Using Oxide Based Cu and Zn Bimetallic Catalyst. *Electrochimica Acta* **2021**, *392*, 138988. https://doi.org/10.1016/j.electacta.2021.138988.
(51) Chen, Z.; Mou, K.; Wang, X.; Liu, L. Nitrogen-Doped Graphene Quantum Dots Enhance the Activity of Bi $_2$ O $_3$ Nanosheets for Electrochemical Reduction of CO $_2$ in a Wide Negative Potential Region. *Angew. Chem. Int. Ed.* **2018**, *57* (39), 12790–12794. https://doi.org/10.1002/anie.201807643.
(52) Fan, L.; Xia, Z.; Xu, M.; Lu, Y.; Li, Z. 1D SnO $_2$ with Wire-in-Tube Architectures for Highly Selective Electrochemical Reduction of CO $_2$ to C $_1$ Products. *Adv. Funct. Mater.* **2018**, *28* (17), 1706289. https://doi.org/10.1002/adfm.201706289.
(53) Loiudice, A.; Lobaccaro, P.; Kamali, E. A.; Thao, T.; Huang, B. H.; Ager, J. W.; Buonsanti, R. Tailoring Copper Nanocrystals towards C $_2$ Products in Electrochemical CO $_2$ Reduction. *Angew. Chem. Int. Ed.* **2016**, *55* (19), 5789–5792. https://doi.org/10.1002/anie.201601582.
(54) Reske, R.; Mistry, H.; Behafarid, F.; Roldan Cuenya, B.; Strasser, P. Particle Size Effects in the Catalytic Electroreduction of CO $_2$ on Cu Nanoparticles. *J. Am. Chem. Soc.* **2014**, *136* (19), 6978–6986. https://doi.org/10.1021/ja500328k.
(55) Bu, Y.; Zhao, M.; Zhang, G.; Zhang, X.; Gao, W.; Jiang, Q. Electroreduction of CO $_2$ on Cu Clusters: The Effects of Size, Symmetry, and Temperature. *ChemElectroChem* **2019**, *6* (6), 1831–1837. https://doi.org/10.1002/celc.201801830.
(56) Zhang, B.; Zhang, J.; Hua, M.; Wan, Q.; Su, Z.; Tan, X.; Liu, L.; Zhang, F.; Chen, G.; Tan, D.; Cheng, X.; Han, B.; Zheng, L.; Mo, G. Highly Electrocatalytic Ethylene Production from CO $_2$ on Nanodefective Cu Nanosheets. *J. Am. Chem. Soc.* **2020**, *142* (31), 13606–13613. https://doi.org/10.1021/jacs.0c06420.
(57) Hori, Y.; Konishi, H.; Futamura, T.; Murata, A.; Koga, O.; Sakurai, H.; Oguma, K. "Deactivation of Copper Electrode" in Electrochemical Reduction of CO2. *Electrochimica Acta* **2005**, *50* (27), 5354–5369. https://doi.org/10.1016/j.electacta.2005.03.015.
(58) Pan, Z.; Han, E.; Zheng, J.; Lu, J.; Wang, X.; Yin, Y.; Waterhouse, G. I. N.; Wang, X.; Li, P. Highly Efficient Photoelectrocatalytic Reduction of CO2 to Methanol by a p–n Heterojunction CeO2/CuO/Cu Catalyst. *Nano-Micro Lett.* **2020**, *12* (1), 18. https://doi.org/10.1007/s40820-019-0354-1.
(59) Wang, P.; Qiao, M.; Shao, Q.; Pi, Y.; Zhu, X.; Li, Y.; Huang, X. Phase and Structure Engineering of Copper Tin Heterostructures for Efficient Electrochemical Carbon Dioxide Reduction. *Nat. Commun.* **2018**, *9* (1), 4933. https://doi.org/10.1038/s41467-018-07419-z.
(60) Durand, W. J.; Peterson, A. A.; Studt, F.; Abild-Pedersen, F.; Nørskov, J. K. Structure Effects on the Energetics of the Electrochemical Reduction of CO2 by Copper Surfaces. *Surf. Sci.* **2011**, *605* (15–16), 1354–1359. https://doi.org/10.1016/j.susc.2011.04.028.
(61) Liu, X.; Xiao, J.; Peng, H.; Hong, X.; Chan, K.; Nørskov, J. K. Understanding Trends in Electrochemical Carbon Dioxide Reduction Rates. *Nat. Commun.* **2017**, *8* (1), 15438. https://doi.org/10.1038/ncomms15438.
(62) Hori, Y.; Takahashi, I.; Koga, O.; Hoshi, N. Selective Formation of C2 Compounds from Electrochemical Reduction of CO $_2$ at a Series of Copper Single Crystal Electrodes. *J. Phys. Chem. B* **2002**, *106* (1), 15–17. https://doi.org/10.1021/jp013478d.
(63) Hori, Y.; Takahashi, I.; Koga, O.; Hoshi, N. Electrochemical Reduction of Carbon Dioxide at Various Series of Copper Single Crystal Electrodes. *J. Mol. Catal. Chem.* **2003**, *199* (1–2), 39–47. https://doi.org/10.1016/S1381-1169(03)00016-5.
(64) Hahn, C.; Hatsukade, T.; Kim, Y.-G.; Vailionis, A.; Baricuatro, J. H.; Higgins, D. C.; Nitopi, S. A.; Soriaga, M. P.; Jaramillo, T. F. Engineering Cu Surfaces for the Electrocatalytic Conversion of CO $_2$: Controlling Selectivity toward Oxygenates and Hydrocarbons. *Proc. Natl. Acad. Sci.* **2017**, *114* (23), 5918–5923. https://doi.org/10.1073/pnas.1618935114.
(65) Ross, P. N. Structure Sensitivity in the Electrocatalytic Properties of Pt: I . Hydrogen Adsorption on Low Index Single Crystals and the Role of Steps. *J. Electrochem. Soc.* **1979**, *126* (1), 67–77. https://doi.org/10.1149/1.2128990.

(66) Marković, N. M.; Adić, R. R.; Vešović, V. B. Structural Effects in Electrocatalysis. *J. Electroanal. Chem. Interfacial Electrochem.* **1984**, *165* (1–2), 121–133. https://doi.org/10.1016/S0022-0728(84)80091-1.
(67) Lee, C. W.; Yang, K. D.; Nam, D.-H.; Jang, J. H.; Cho, N. H.; Im, S. W.; Nam, K. T. Defining a Materials Database for the Design of Copper Binary Alloy Catalysts for Electrochemical CO_2 Conversion. *Adv. Mater.* **2018**, *30* (42), 1704717. https://doi.org/10.1002/adma.201704717.
(68) Tsai, A. P.; Kameoka, S.; Nozawa, K.; Shimoda, M.; Ishii, Y. Intermetallic: A Pseudoelement for Catalysis. *Acc. Chem. Res.* **2017**, *50* (12), 2879–2885. https://doi.org/10.1021/acs.accounts.7b00476.
(69) Zhao, Z.; Lu, G. Cu-Based Single-Atom Catalysts Boost Electroreduction of CO_2 to CH_3OH: First-Principles Predictions. *J. Phys. Chem. C* **2019**, *123* (7), 4380–4387. https://doi.org/10.1021/acs.jpcc.8b12449.
(70) Wang, Y.; Liu, J.; Zheng, G. Designing Copper-Based Catalysts for Efficient Carbon Dioxide Electroreduction. *Adv. Mater.* **2021**, *33* (46), 2005798. https://doi.org/10.1002/adma.202005798.
(71) Ni, Z.; Liang, H.; Yi, Z.; Guo, R.; Liu, C.; Liu, Y.; Sun, H.; Liu, X. Research Progress of Electrochemical CO2 Reduction for Copper-Based Catalysts to Multicarbon Products. *Coord. Chem. Rev.* **2021**, *441*, 213983. https://doi.org/10.1016/j.ccr.2021.213983.
(72) Chen, C. S.; Wan, J. H.; Yeo, B. S. Electrochemical Reduction of Carbon Dioxide to Ethane Using Nanostructured Cu_2O-Derived Copper Catalyst and Palladium(II) Chloride. *J. Phys. Chem. C* **2015**, *119* (48), 26875–26882. https://doi.org/10.1021/acs.jpcc.5b09144.
(73) Zhang, S.; Kang, P.; Bakir, M.; Lapides, A. M.; Dares, C. J.; Meyer, T. J. Polymer-Supported CuPd Nanoalloy as a Synergistic Catalyst for Electrocatalytic Reduction of Carbon Dioxide to Methane. *Proc. Natl. Acad. Sci.* **2015**, *112* (52), 15809–15814. https://doi.org/10.1073/pnas.1522496112.
(74) Li, Q.; Fu, J.; Zhu, W.; Chen, Z.; Shen, B.; Wu, L.; Xi, Z.; Wang, T.; Lu, G.; Zhu, J.; Sun, S. Tuning Sn-Catalysis for Electrochemical Reduction of CO_2 to CO via the Core/Shell Cu/SnO_2 Structure. *J. Am. Chem. Soc.* **2017**, *139* (12), 4290–4293. https://doi.org/10.1021/jacs.7b00261.
(75) Sarfraz, S.; Garcia-Esparza, A. T.; Jedidi, A.; Cavallo, L.; Takanabe, K. Cu–Sn Bimetallic Catalyst for Selective Aqueous Electroreduction of CO_2 to CO. *ACS Catal.* **2016**, *6* (5), 2842–2851. https://doi.org/10.1021/acscatal.6b00269.
(76) DeMeo, D.; MacNaughton, S.; Sonkusale, S.; Vandervelde, T. Electrodeposited Copper Oxide and Zinc Oxide Core-Shell Nanowire Photovoltaic Cells. In *Nanowires - Implementations and Applications*; Hashim, A., Ed.; InTech, 2011. https://doi.org/10.5772/17644.
(77) Ting, L. R. L.; Piqué, O.; Lim, S. Y.; Tanhaei, M.; Calle-Vallejo, F.; Yeo, B. S. Enhancing CO_2 Electroreduction to Ethanol on Copper–Silver Composites by Opening an Alternative Catalytic Pathway. *ACS Catal.* **2020**, *10* (7), 4059–4069. https://doi.org/10.1021/acscatal.9b05319.
(78) Sripada, P.; Kimpton, J.; Barlow, A.; Williams, T.; Kandasamy, S.; Bhattacharya, S. Investigating the Dynamic Structural Changes on Cu/CeO2 Catalysts Observed during CO2 Hydrogenation. *J. Catal.* **2020**, *381*, 415–426. https://doi.org/10.1016/j.jcat.2019.11.017.
(79) Zhu, J.; Su, Y.; Chai, J.; Muravev, V.; Kosinov, N.; Hensen, E. J. M. Mechanism and Nature of Active Sites for Methanol Synthesis from CO/CO_2 on Cu/CeO_2. *ACS Catal.* **2020**, *10* (19), 11532–11544. https://doi.org/10.1021/acscatal.0c02909.
(80) Li, J.; Zhang, S.; Wang, J.; Yin, X.; Han, Z.; Chen, G.; Zhang, D.; Wang, M. Electrocatalytic CO2 Reduction and H2 Evolution by a Copper (II) Complex with Redox-Active Ligand. *Molecules* **2022**, *27* (4), 1399. https://doi.org/10.3390/molecules27041399.
(81) Boutin, E.; Wang, M.; Lin, J. C.; Mesnage, M.; Mendoza, D.; Lassalle-Kaiser, B.; Hahn, C.; Jaramillo, T. F.; Robert, M. Aqueous Electrochemical Reduction of Carbon Dioxide and Carbon Monoxide into Methanol with Cobalt Phthalocyanine. *Angew. Chem.* **2019**, *131* (45), 16318–16322. https://doi.org/10.1002/ange.201909257.
(82) Li, P.; Xu, J.; Jing, H.; Wu, C.; Peng, H.; Lu, J.; Yin, H. Wedged N-Doped CuO with More Negative Conductive Band and Lower Overpotential for High Efficiency Photoelectric Converting CO2 to

Methanol. *Appl. Catal. B Environ.* **2014**, *156–157*, 134–140. https://doi.org/10.1016/j.apcatb.2014.03.011.

(83) Tran, N.-H.; Duong, H. P.; Rousse, G.; Zanna, S.; Schreiber, M. W.; Fontecave, M. Selective Ethylene Production from CO_2 and CO Reduction via Engineering Membrane Electrode Assembly with Porous Dendritic Copper Oxide. *ACS Appl. Mater. Interfaces* **2022**, *14* (28), 31933–31941. https://doi.org/10.1021/acsami.2c06068.

(84) Huan, T. N.; Dalla Corte, D. A.; Lamaison, S.; Karapinar, D.; Lutz, L.; Menguy, N.; Foldyna, M.; Turren-Cruz, S.-H.; Hagfeldt, A.; Bella, F.; Fontecave, M.; Mougel, V. Low-Cost High-Efficiency System for Solar-Driven Conversion of CO_2 to Hydrocarbons. *Proc. Natl. Acad. Sci.* **2019**, *116* (20), 9735–9740. https://doi.org/10.1073/pnas.1815412116.

(85) Anandan, S.; Wen, X.; Yang, S. Room Temperature Growth of CuO Nanorod Arrays on Copper and Their Application as a Cathode in Dye-Sensitized Solar Cells. *Mater. Chem. Phys.* **2005**, *93* (1), 35–40. https://doi.org/10.1016/j.matchemphys.2005.02.002.

(86) Chen, J.; Xu, L.; Xing, R.; Song, J.; Song, H.; Liu, D.; Zhou, J. Electrospun Three-Dimensional Porous CuO/TiO2 Hierarchical Nanocomposites Electrode for Nonenzymatic Glucose Biosensing. *Electrochem. Commun.* **2012**, *20*, 75–78. https://doi.org/10.1016/j.elecom.2012.01.032.

(87) Dias, E. H.; Da Silva, G. T. S. T.; Da Cruz, J. C.; Ribeiro, C. One-Pot Solvothermal Synthesis of Carbon Black-Supported CuO for Catalysis of CO_2 Electroreduction. *ChemElectroChem* **2022**, *9* (11). https://doi.org/10.1002/celc.202200206.

(88) Dhanasekaran, V.; Mahalingam, T. Electrochemical and Physical Properties of Electroplated CuO Thin Films. *J. Nanosci. Nanotechnol.* **2013**, *13* (1), 250–259. https://doi.org/10.1166/jnn.2013.6709.

(89) Avgouropoulos, G.; Ioannides, T.; Matralis, H. Influence of the Preparation Method on the Performance of CuO–CeO2 Catalysts for the Selective Oxidation of CO. *Appl. Catal. B Environ.* **2005**, *56* (1–2), 87–93. https://doi.org/10.1016/j.apcatb.2004.07.017.

(90) Ren, D.; Deng, Y.; Handoko, A. D.; Chen, C. S.; Malkhandi, S.; Yeo, B. S. Selective Electrochemical Reduction of Carbon Dioxide to Ethylene and Ethanol on Copper(I) Oxide Catalysts. *ACS Catal.* **2015**, *5* (5), 2814–2821. https://doi.org/10.1021/cs502128q.

(91) Lum, Y.; Yue, B.; Lobaccaro, P.; Bell, A. T.; Ager, J. W. Optimizing C–C Coupling on Oxide-Derived Copper Catalysts for Electrochemical CO_2 Reduction. *J. Phys. Chem. C* **2017**, *121* (26), 14191–14203. https://doi.org/10.1021/acs.jpcc.7b03673.

(92) Vasileff, A.; Zhu, Y.; Zhi, X.; Zhao, Y.; Ge, L.; Chen, H. M.; Zheng, Y.; Qiao, S. Electrochemical Reduction of CO_2 to Ethane through Stabilization of an Ethoxy Intermediate. *Angew. Chem. Int. Ed.* **2020**, *59* (44), 19649–19653. https://doi.org/10.1002/anie.202004846.

(93) Abuhmaiera, R.; Lan, Y.; Ako, A. M.; Kostakis, G. E.; Mavrandonakis, A.; Klopper, W.; Clérac, R.; Anson, C. E.; Powell, A. K. One-Dimensional Cu(II) Coordination Polymers: Tuning the Structure by Modulating the "Carboxylate Arm" Lengths of Polycarboxylate Ligands. *CrystEngComm* **2009**, *11* (6), 1089. https://doi.org/10.1039/b820834d.

(94) Tapan, N. A. CO2 Electroreduction on P4VP Modified Copper Deposited Gas Diffusion Layer Electrode: PH Effect. *Mater. Renew. Sustain. Energy* **2016**, *5* (4), 19. https://doi.org/10.1007/s40243-016-0082-0.

(95) Gao, B.; Kong, D.; Zhang, Y. Preparation and Catalytic Activity of P4VP–Cu(II) Complex Supported on Silica Gel. *J. Mol. Catal. Chem.* **2008**, *286* (1–2), 143–148. https://doi.org/10.1016/j.molcata.2008.02.012.

(96) Kamata, R.; Kumagai, H.; Yamazaki, Y.; Sahara, G.; Ishitani, O. Photoelectrochemical CO_2 Reduction Using a Ru(II)–Re(I) Supramolecular Photocatalyst Connected to a Vinyl Polymer on a NiO Electrode. *ACS Appl. Mater. Interfaces* **2019**, *11* (6), 5632–5641. https://doi.org/10.1021/acsami.8b05495.

(97) Brezinski, W. P.; Karayilan, M.; Clary, K. E.; McCleary-Petersen, K. C.; Fu, L.; Matyjaszewski, K.; Evans, D. H.; Lichtenberger, D. L.; Glass, R. S.; Pyun, J. Macromolecular Engineering of the Outer Coordination Sphere of [2Fe-2S] Metallopolymers to Enhance Catalytic Activity for H_2

Production. *ACS Macro Lett.* **2018**, *7* (11), 1383–1387. https://doi.org/10.1021/acsmacrolett.8b00765.
(98) Zhang, L.; Wei, Z.; Thanneeru, S.; Meng, M.; Kruzyk, M.; Ung, G.; Liu, B.; He, J. A Polymer Solution To Prevent Nanoclustering and Improve the Selectivity of Metal Nanoparticles for Electrocatalytic CO $_2$ Reduction. *Angew. Chem.* **2019**, *131* (44), 15981–15987. https://doi.org/10.1002/ange.201909069.
(99) Liu, Y.; McCrory, C. C. L. Modulating the Mechanism of Electrocatalytic CO2 Reduction by Cobalt Phthalocyanine through Polymer Coordination and Encapsulation. *Nat. Commun.* **2019**, *10* (1), 1683. https://doi.org/10.1038/s41467-019-09626-8.
(100) Pham, T. H. M.; Zhang, J.; Li, M.; Shen, T.; Ko, Y.; Tileli, V.; Luo, W.; Züttel, A. Enhanced Electrocatalytic CO $_2$ Reduction to C $_{2+}$ Products by Adjusting the Local Reaction Environment with Polymer Binders. *Adv. Energy Mater.* **2022**, *12* (9), 2103663. https://doi.org/10.1002/aenm.202103663.
(101) Soucy, T. L.; Dean, W. S.; Zhou, J.; Rivera Cruz, K. E.; McCrory, C. C. L. Considering the Influence of Polymer–Catalyst Interactions on the Chemical Microenvironment of Electrocatalysts for the CO $_2$ Reduction Reaction. *Acc. Chem. Res.* **2022**, *55* (3), 252–261. https://doi.org/10.1021/acs.accounts.1c00633.
(102) Senocrate, A.; Bernasconi, F.; Rentsch, D.; Kraft, K.; Trottmann, M.; Wichser, A.; Bleiner, D.; Battaglia, C. Importance of Substrate Pore Size and Wetting Behavior in Gas Diffusion Electrodes for CO $_2$ Reduction. *ACS Appl. Energy Mater.* **2022**, *5* (11), 14504–14512. https://doi.org/10.1021/acsaem.2c03054.
(103) Wakerley, D.; Lamaison, S.; Ozanam, F.; Menguy, N.; Mercier, D.; Marcus, P.; Fontecave, M.; Mougel, V. Bio-Inspired Hydrophobicity Promotes CO2 Reduction on a Cu Surface. *Nat. Mater.* **2019**, *18* (11), 1222–1227. https://doi.org/10.1038/s41563-019-0445-x.
(104) Cao, Z.; Derrick, J. S.; Xu, J.; Gao, R.; Gong, M.; Nichols, E. M.; Smith, P. T.; Liu, X.; Wen, X.; Copéret, C.; Chang, C. J. Chelating N-Heterocyclic Carbene Ligands Enable Tuning of Electrocatalytic CO $_2$ Reduction to Formate and Carbon Monoxide: Surface Organometallic Chemistry. *Angew. Chem.* **2018**, *130* (18), 5075–5079. https://doi.org/10.1002/ange.201800367.
(105) Ma, Y.; Wang, J.; Yu, J.; Zhou, J.; Zhou, X.; Li, H.; He, Z.; Long, H.; Wang, Y.; Lu, P.; Yin, J.; Sun, H.; Zhang, Z.; Fan, Z. Surface Modification of Metal Materials for High-Performance Electrocatalytic Carbon Dioxide Reduction. *Matter* **2021**, *4* (3), 888–926. https://doi.org/10.1016/j.matt.2021.01.007.
(106) Koshy, D. M.; Akhade, S. A.; Shugar, A.; Abiose, K.; Shi, J.; Liang, S.; Oakdale, J. S.; Weitzner, S. E.; Varley, J. B.; Duoss, E. B.; Baker, S. E.; Hahn, C.; Bao, Z.; Jaramillo, T. F. Chemical Modifications of Ag Catalyst Surfaces with Imidazolium Ionomers Modulate H $_2$ Evolution Rates during Electrochemical CO $_2$ Reduction. *J. Am. Chem. Soc.* **2021**, *143* (36), 14712–14725. https://doi.org/10.1021/jacs.1c06212.
(107) García de Arquer, F. P.; Dinh, C.-T.; Ozden, A.; Wicks, J.; McCallum, C.; Kirmani, A. R.; Nam, D.-H.; Gabardo, C.; Seifitokaldani, A.; Wang, X.; Li, Y. C.; Li, F.; Edwards, J.; Richter, L. J.; Thorpe, S. J.; Sinton, D.; Sargent, E. H. CO $_2$ Electrolysis to Multicarbon Products at Activities Greater than 1 A Cm $^{-2}$. *Science* **2020**, *367* (6478), 661–666. https://doi.org/10.1126/science.aay4217.
(108) Iijima, G.; Kitagawa, T.; Katayama, A.; Inomata, T.; Yamaguchi, H.; Suzuki, K.; Hirata, K.; Hijikata, Y.; Ito, M.; Masuda, H. CO $_2$ Reduction Promoted by Imidazole Supported on a Phosphonium-Type Ionic-Liquid-Modified Au Electrode at a Low Overpotential. *ACS Catal.* **2018**, *8* (3), 1990–2000. https://doi.org/10.1021/acscatal.7b03274.
(109) Han, Z.; Kortlever, R.; Chen, H.-Y.; Peters, J. C.; Agapie, T. CO $_2$ Reduction Selective for C $_{\geq 2}$ Products on Polycrystalline Copper with N-Substituted Pyridinium Additives. *ACS Cent. Sci.* **2017**, *3* (8), 853–859. https://doi.org/10.1021/acscentsci.7b00180.
(110) Wang, X.; Wang, Z.; García de Arquer, F. P.; Dinh, C.-T.; Ozden, A.; Li, Y. C.; Nam, D.-H.; Li, J.; Liu, Y.-S.; Wicks, J.; Chen, Z.; Chi, M.; Chen, B.; Wang, Y.; Tam, J.; Howe, J. Y.; Proppe, A.; Todorović, P.; Li, F.; Zhuang, T.-T.; Gabardo, C. M.; Kirmani, A. R.; McCallum, C.; Hung, S.-F.; Lum, Y.; Luo,

M.; Min, Y.; Xu, A.; O'Brien, C. P.; Stephen, B.; Sun, B.; Ip, A. H.; Richter, L. J.; Kelley, S. O.; Sinton, D.; Sargent, E. H. Efficient Electrically Powered CO2-to-Ethanol via Suppression of Deoxygenation. *Nat. Energy* **2020**, *5* (6), 478–486. https://doi.org/10.1038/s41560-020-0607-8.

(111) Buckley, A. K.; Lee, M.; Cheng, T.; Kazantsev, R. V.; Larson, D. M.; Goddard III, W. A.; Toste, F. D.; Toma, F. M. Electrocatalysis at Organic–Metal Interfaces: Identification of Structure–Reactivity Relationships for CO_2 Reduction at Modified Cu Surfaces. *J. Am. Chem. Soc.* **2019**, *141* (18), 7355–7364. https://doi.org/10.1021/jacs.8b13655.

(112) Zhao, Y.; Wang, C.; Liu, Y.; MacFarlane, D. R.; Wallace, G. G. Engineering Surface Amine Modifiers of Ultrasmall Gold Nanoparticles Supported on Reduced Graphene Oxide for Improved Electrochemical CO_2 Reduction. *Adv. Energy Mater.* **2018**, *8* (25), 1801400. https://doi.org/10.1002/aenm.201801400.

(113) Wei, X.; Yin, Z.; Lyu, K.; Li, Z.; Gong, J.; Wang, G.; Xiao, L.; Lu, J.; Zhuang, L. Highly Selective Reduction of CO_2 to C_{2+} Hydrocarbons at Copper/Polyaniline Interfaces. *ACS Catal.* **2020**, *10* (7), 4103–4111. https://doi.org/10.1021/acscatal.0c00049.

(114) Liang, H.-Q.; Zhao, S.; Hu, X.-M.; Ceccato, M.; Skrydstrup, T.; Daasbjerg, K. Hydrophobic Copper Interfaces Boost Electroreduction of Carbon Dioxide to Ethylene in Water. *ACS Catal.* **2021**, *11* (2), 958–966. https://doi.org/10.1021/acscatal.0c03766.

(115) Thevenon, A.; Rosas-Hernández, A.; Peters, J. C.; Agapie, T. In-Situ Nanostructuring and Stabilization of Polycrystalline Copper by an Organic Salt Additive Promotes Electrocatalytic CO_2 Reduction to Ethylene. *Angew. Chem. Int. Ed.* **2019**, *58* (47), 16952–16958. https://doi.org/10.1002/anie.201907935.

(116) Kim, C.; Eom, T.; Jee, M. S.; Jung, H.; Kim, H.; Min, B. K.; Hwang, Y. J. Insight into Electrochemical CO_2 Reduction on Surface-Molecule-Mediated Ag Nanoparticles. *ACS Catal.* **2017**, *7* (1), 779–785. https://doi.org/10.1021/acscatal.6b01862.

(117) Verma, S.; Hamasaki, Y.; Kim, C.; Huang, W.; Lu, S.; Jhong, H.-R. M.; Gewirth, A. A.; Fujigaya, T.; Nakashima, N.; Kenis, P. J. A. Insights into the Low Overpotential Electroreduction of CO_2 to CO on a Supported Gold Catalyst in an Alkaline Flow Electrolyzer. *ACS Energy Lett.* **2018**, *3* (1), 193–198. https://doi.org/10.1021/acsenergylett.7b01096.

(118) Creissen, C. E.; Rivera de la Cruz, J. G.; Karapinar, D.; Taverna, D.; Schreiber, M. W.; Fontecave, M. Molecular Inhibition for Selective CO_2 Conversion. *Angew. Chem. Int. Ed.* **2022**, *61* (32). https://doi.org/10.1002/anie.202206279.

(119) Li, F.; Thevenon, A.; Rosas-Hernández, A.; Wang, Z.; Li, Y.; Gabardo, C. M.; Ozden, A.; Dinh, C. T.; Li, J.; Wang, Y.; Edwards, J. P.; Xu, Y.; McCallum, C.; Tao, L.; Liang, Z.-Q.; Luo, M.; Wang, X.; Li, H.; O'Brien, C. P.; Tan, C.-S.; Nam, D.-H.; Quintero-Bermudez, R.; Zhuang, T.-T.; Li, Y. C.; Han, Z.; Britt, R. D.; Sinton, D.; Agapie, T.; Peters, J. C.; Sargent, E. H. Molecular Tuning of CO2-to-Ethylene Conversion. *Nature* **2020**, *577* (7791), 509–513. https://doi.org/10.1038/s41586-019-1782-2.

(120) Ahn, S.; Klyukin, K.; Wakeham, R. J.; Rudd, J. A.; Lewis, A. R.; Alexander, S.; Carla, F.; Alexandrov, V.; Andreoli, E. Poly-Amide Modified Copper Foam Electrodes for Enhanced Electrochemical Reduction of Carbon Dioxide. *ACS Catal.* **2018**, *8* (5), 4132–4142. https://doi.org/10.1021/acscatal.7b04347.

(121) de la Cruz, P. T. S.; Irikura, K.; Lachgar, A.; Cardoso, J. C.; Cavero, H. A.; Zanoni, M. V. B. Preparation of FTO/CU2O Electrode Protected by PEDOT:PSS and Its Better Performance in the Photoelectrocatalytic Reduction of CO2 to Methanol. *Electrocatalysis* **2020**, *11* (5), 546–554. https://doi.org/10.1007/s12678-020-00612-z.

(122) Barton Cole, E.; Lakkaraju, P. S.; Rampulla, D. M.; Morris, A. J.; Abelev, E.; Bocarsly, A. B. Using a One-Electron Shuttle for the Multielectron Reduction of CO_2 to Methanol: Kinetic, Mechanistic, and Structural Insights. *J. Am. Chem. Soc.* **2010**, *132* (33), 11539–11551. https://doi.org/10.1021/ja1023496.

(123) Escalé, P.; Rubatat, L.; Billon, L.; Save, M. Recent Advances in Honeycomb-Structured Porous Polymer Films Prepared via Breath Figures. *Eur. Polym. J.* **2012**, *48* (6), 1001–1025. https://doi.org/10.1016/j.eurpolymj.2012.03.001.
(124) Aynard, A.; Pessoni, L.; Billon, L. Directed Self-Assembly in "Breath Figure" Templating of Block Copolymers Followed by Soft Hydrolysis-Condensation: One Step towards Synthetic Bio-Inspired Silica Diatoms Exoskeleton. *Polymer* **2020**, *210*, 123047. https://doi.org/10.1016/j.polymer.2020.123047.
(125) Li, Z.; Ma, X.; Zang, D.; Hong, Q.; Guan, X. Honeycomb Porous Films of Pentablock Copolymer on Liquid Substrates via Breath Figure Method and Their Hydrophobic Properties with Static and Dynamic Behaviour. *RSC Adv.* **2015**, *5* (27), 21084–21089. https://doi.org/10.1039/C5RA00066A.
(126) Zhou, W.; Chen, J.; Li, Y.; Wang, D.; Chen, J.; Feng, X.; Huang, Z.; Liu, R.; Lin, X.; Zhang, H.; Mi, B.; Ma, Y. Copper Mesh Templated by Breath-Figure Polymer Films as Flexible Transparent Electrodes for Organic Photovoltaic Devices. *ACS Appl. Mater. Interfaces* **2016**, *8* (17), 11122–11127. https://doi.org/10.1021/acsami.6b01117.
(127) Bertrand, A.; Dumur, F.; Mruczkiewicz, M.; Perrin, M.; Lartigau-Dagron, C.; Bousquet, A.; Vignau, L.; Billon, L.; Fasquel, S. Bottom-up Honeycomb Top Layer for Light Outcoupling Enhancement in Blue Organic Light Emitting Diodes. *Org. Electron.* **2018**, *52*, 222–229. https://doi.org/10.1016/j.orgel.2017.10.022.
(128) Li, Z.; Shang, Y.; Liu, L.; Long, H.; Feng, Y.; Billon, L.; Yin, H. Selenium-Decorated Biocompatible Honeycomb Films with Redox-Switchable Surface for Controlling Cell Adhesion/Detachment. *J. Colloid Interface Sci.* **2023**, *635*, 503–513. https://doi.org/10.1016/j.jcis.2022.12.133.
(129) Marcasuzaa, P.; Pearson, S.; Bosson, K.; Pessoni, L.; Dupin, J.-C.; Billon, L. Reactive Nano-Patterns in Triple Structured Bio-Inspired Honeycomb Films as a Clickable Platform. *Chem. Commun.* **2018**, *54* (93), 13068–13071. https://doi.org/10.1039/C8CC05333B.
(130) Bosson, K.; Marcasuzaa, P.; Bousquet, A.; Tovar, G. E. M.; Atanasov, V.; Billon, L. PentaFluoroStyrene-Based Block Copolymers Controlled Self-Assembly Pattern: A Platform Paving the Way to Functional Block Copolymers. *Eur. Polym. J.* **2022**, *179*, 111560. https://doi.org/10.1016/j.eurpolymj.2022.111560.
(131) Marcasuzaa, P.; Save, M.; Gérard, P.; Billon, L. When a PH-Triggered Nanopatterned Shape Transition Drives the Wettability of a Hierarchically Self-Organized Film: A Bio-Inspired Effect of "Sea Anemone." *J. Colloid Interface Sci.* **2021**, *581*, 96–101. https://doi.org/10.1016/j.jcis.2020.07.130.
(132) Yin, H.; Zhan, F.; Li, Z.; Huang, H.; Marcasuzaa, P.; Luo, X.; Feng, Y.; Billon, L. CO_2 -Triggered ON/OFF Wettability Switching on Bioinspired Polylactic Acid Porous Films for Controllable Bioadhesion. *Biomacromolecules* **2021**, *22* (4), 1721–1729. https://doi.org/10.1021/acs.biomac.1c00134.
(133) Escalé, P.; Rubatat, L.; Derail, C.; Save, M.; Billon, L. PH Sensitive Hierarchically Self-Organized Bioinspired Films. *Macromol. Rapid Commun.* **2011**, *32* (14), 1072–1076. https://doi.org/10.1002/marc.201100296.
(134) Billon, L.; Manguian, M.; Pellerin, V.; Joubert, M.; Eterradossi, O.; Garay, H. Tailoring Highly Ordered Honeycomb Films Based on Ionomer Macromolecules by the Bottom-Up Approach. *Macromolecules* **2009**, *42* (1), 345–356. https://doi.org/10.1021/ma8020568.
(135) Birdja, Y. Y.; Vos, R. E.; Wezendonk, T. A.; Jiang, L.; Kapteijn, F.; Koper, M. T. M. Effects of Substrate and Polymer Encapsulation on CO_2 Electroreduction by Immobilized Indium(III) Protoporphyrin. *ACS Catal.* **2018**, *8* (5), 4420–4428. https://doi.org/10.1021/acscatal.7b03386.
(136) Leung, J. J.; Vigil, J. A.; Warnan, J.; Edwardes Moore, E.; Reisner, E. Rational Design of Polymers for Selective CO_2 Reduction Catalysis. *Angew. Chem. Int. Ed.* **2019**, *58* (23), 7697–7701. https://doi.org/10.1002/anie.201902218.
(137) Coskun, H.; Aljabour, A.; De Luna, P.; Farka, D.; Greunz, T.; Stifter, D.; Kus, M.; Zheng, X.; Liu, M.; Hassel, A. W.; Schöfberger, W.; Sargent, E. H.; Sariciftci, N. S.; Stadler, P. Biofunctionalized

Conductive Polymers Enable Efficient CO 2 Electroreduction. *Sci. Adv.* **2017**, *3* (8), e1700686. https://doi.org/10.1126/sciadv.1700686.
(138) Johnson, D.; Hilal, N.; Bowen, W. R. Basic Principles of Atomic Force Microscopy. In *Atomic Force Microscopy in Process Engineering*; Elsevier, 2009; pp 1–30. https://doi.org/10.1016/B978-1-85617-517-3.00001-8.
(139) Vitha, M. F. *Spectroscopy: Principles and Instrumentation*, First edition.; Wiley: Hoboken, NJ, 2018.
(140) Stiedl, J.; Green, Simon; Chassé, Thomas; Rebner, Karsten. Auger Electron Spectroscopy and UV-Vis Spectroscopy in Combination with Multivariate Curve Resolution Analysis to Determine the Cu2O/CuO Ratios in Oxide Layers on Technical Copper Surfaces. **2019**, *486*, 354–361. https://doi.org/10.1016/j.apsusc.2019.05.028.
(141) Makuła, P.; Pacia, M.; Macyk, W. How To Correctly Determine the Band Gap Energy of Modified Semiconductor Photocatalysts Based on UV–Vis Spectra. *J. Phys. Chem. Lett.* **2018**, *9* (23), 6814–6817. https://doi.org/10.1021/acs.jpclett.8b02892.
(142) Kwok, D. Y.; Neumann, A. W. Contact Angle Measurement and Contact Angle Interpretation. *Adv. Colloid Interface Sci.* **1999**, *81* (3), 167–249. https://doi.org/10.1016/S0001-8686(98)00087-6.
(143) Keeler, J. *Understanding NMR Spectroscopy*, 2nd ed.; John Wiley and Sons: Chichester, U.K, 2010.
(144) Epp, J. X-Ray Diffraction (XRD) Techniques for Materials Characterization. In *Materials Characterization Using Nondestructive Evaluation (NDE) Methods*; Elsevier, 2016; pp 81–124. https://doi.org/10.1016/B978-0-08-100040-3.00004-3.
(145) Inkson, B. J. Scanning Electron Microscopy (SEM) and Transmission Electron Microscopy (TEM) for Materials Characterization. In *Materials Characterization Using Nondestructive Evaluation (NDE) Methods*; Elsevier, 2016; pp 17–43. https://doi.org/10.1016/B978-0-08-100040-3.00002-X.
(146) Powell, C. J.; Jablonski, A.; Tilinin, I. S.; Tanuma, S.; Penn, D. R. Surface Sensitivity of Auger-Electron Spectroscopy and X-Ray Photoelectron Spectroscopy. *J. Electron Spectrosc. Relat. Phenom.* **1999**, *98–99*, 1–15. https://doi.org/10.1016/S0368-2048(98)00271-0.
(147) *Modern Size-Exclusion Liquid Chromatography: Practice of Gel Permeation and Gel Filtration Chromatography*, 2nd ed.; Striegel, A. M., Ed.; Wiley: Hoboken, N.J, 2009.
(148) Chen, C.; Khosrowabadi Kotyk, J. F.; Sheehan, S. W. Progress toward Commercial Application of Electrochemical Carbon Dioxide Reduction. *Chem* **2018**, *4* (11), 2571–2586. https://doi.org/10.1016/j.chempr.2018.08.019.
(149) Bonke, S. A.; Wiechen, M.; MacFarlane, D. R.; Spiccia, L. Renewable Fuels from Concentrated Solar Power: Towards Practical Artificial Photosynthesis. *Energy Environ. Sci.* **2015**, *8* (9), 2791–2796. https://doi.org/10.1039/C5EE02214B.
(150) Hepburn, C.; Adlen, E.; Beddington, J.; Carter, E. A.; Fuss, S.; Mac Dowell, N.; Minx, J. C.; Smith, P.; Williams, C. K. The Technological and Economic Prospects for CO2 Utilization and Removal. *Nature* **2019**, *575* (7781), 87–97. https://doi.org/10.1038/s41586-019-1681-6.
(151) Centi, G.; Perathoner, S. Towards Solar Fuels from Water and CO 2. *ChemSusChem* **2010**, *3* (2), 195–208. https://doi.org/10.1002/cssc.200900289.
(152) Bushuyev, O. S.; De Luna, P.; Dinh, C. T.; Tao, L.; Saur, G.; van de Lagemaat, J.; Kelley, S. O.; Sargent, E. H. What Should We Make with CO2 and How Can We Make It? *Joule* **2018**, *2* (5), 825–832. https://doi.org/10.1016/j.joule.2017.09.003.
(153) De Luna, P.; Hahn, C.; Higgins, D.; Jaffer, S. A.; Jaramillo, T. F.; Sargent, E. H. What Would It Take for Renewably Powered Electrosynthesis to Displace Petrochemical Processes? *Science* **2019**, *364* (6438), eaav3506. https://doi.org/10.1126/science.aav3506.
(154) Smith, W. A.; Burdyny, T.; Vermaas, D. A.; Geerlings, H. Pathways to Industrial-Scale Fuel Out of Thin Air from CO2 Electrolysis. *Joule* **2019**, *3* (8), 1822–1834. https://doi.org/10.1016/j.joule.2019.07.009.

(155) Boutin, E.; Robert, M. Molecular Electrochemical Reduction of CO2 beyond Two Electrons. *Trends Chem.* **2021**, *3* (5), 359–372. https://doi.org/10.1016/j.trechm.2021.02.003.
(156) Wang, Y.; Wang, Z.; Dinh, C.-T.; Li, J.; Ozden, A.; Golam Kibria, M.; Seifitokaldani, A.; Tan, C.-S.; Gabardo, C. M.; Luo, M.; Zhou, H.; Li, F.; Lum, Y.; McCallum, C.; Xu, Y.; Liu, M.; Proppe, A.; Johnston, A.; Todorovic, P.; Zhuang, T.-T.; Sinton, D.; Kelley, S. O.; Sargent, E. H. Catalyst Synthesis under CO2 Electroreduction Favours Faceting and Promotes Renewable Fuels Electrosynthesis. *Nat. Catal.* **2020**, *3* (2), 98–106. https://doi.org/10.1038/s41929-019-0397-1.
(157) Dinh, C.-T.; Burdyny, T.; Kibria, M. G.; Seifitokaldani, A.; Gabardo, C. M.; García de Arquer, F. P.; Kiani, A.; Edwards, J. P.; De Luna, P.; Bushuyev, O. S.; Zou, C.; Quintero-Bermudez, R.; Pang, Y.; Sinton, D.; Sargent, E. H. CO_2 Electroreduction to Ethylene via Hydroxide-Mediated Copper Catalysis at an Abrupt Interface. *Science* **2018**, *360* (6390), 783–787. https://doi.org/10.1126/science.aas9100.
(158) Sedighian Rasouli, A.; Wang, X.; Wicks, J.; Lee, G.; Peng, T.; Li, F.; McCallum, C.; Dinh, C.-T.; Ip, A. H.; Sinton, D.; Sargent, E. H. CO_2 Electroreduction to Methane at Production Rates Exceeding 100 MA/Cm ^{2}. *ACS Sustain. Chem. Eng.* **2020**, *8* (39), 14668–14673. https://doi.org/10.1021/acssuschemeng.0c03453.
(159) Gabardo, C. M.; O'Brien, C. P.; Edwards, J. P.; McCallum, C.; Xu, Y.; Dinh, C.-T.; Li, J.; Sargent, E. H.; Sinton, D. Continuous Carbon Dioxide Electroreduction to Concentrated Multi-Carbon Products Using a Membrane Electrode Assembly. *Joule* **2019**, *3* (11), 2777–2791. https://doi.org/10.1016/j.joule.2019.07.021.
(160) Li, J.; Xu, A.; Li, F.; Wang, Z.; Zou, C.; Gabardo, C. M.; Wang, Y.; Ozden, A.; Xu, Y.; Nam, D.-H.; Lum, Y.; Wicks, J.; Chen, B.; Wang, Z.; Chen, J.; Wen, Y.; Zhuang, T.; Luo, M.; Du, X.; Sham, T.-K.; Zhang, B.; Sargent, E. H.; Sinton, D. Enhanced Multi-Carbon Alcohol Electroproduction from CO via Modulated Hydrogen Adsorption. *Nat. Commun.* **2020**, *11* (1), 3685. https://doi.org/10.1038/s41467-020-17499-5.
(161) Luo, M.; Wang, Z.; Li, Y. C.; Li, J.; Li, F.; Lum, Y.; Nam, D.-H.; Chen, B.; Wicks, J.; Xu, A.; Zhuang, T.; Leow, W. R.; Wang, X.; Dinh, C.-T.; Wang, Y.; Wang, Y.; Sinton, D.; Sargent, E. H. Hydroxide Promotes Carbon Dioxide Electroreduction to Ethanol on Copper via Tuning of Adsorbed Hydrogen. *Nat. Commun.* **2019**, *10* (1), 5814. https://doi.org/10.1038/s41467-019-13833-8.
(162) Gattrell, M.; Gupta, N.; Co, A. A Review of the Aqueous Electrochemical Reduction of CO2 to Hydrocarbons at Copper. *J. Electroanal. Chem.* **2006**, *594* (1), 1–19. https://doi.org/10.1016/j.jelechem.2006.05.013.
(163) Buonsanti, R. Copper, My Precious! *Nat. Catal.* **2021**, *4* (9), 736–737. https://doi.org/10.1038/s41929-021-00674-2.
(164) Huang, J.; Buonsanti, R. Colloidal Nanocrystals as Heterogeneous Catalysts for Electrochemical CO_2 Conversion. *Chem. Mater.* **2019**, *31* (1), 13–25. https://doi.org/10.1021/acs.chemmater.8b04155.
(165) Iyengar, P.; Kolb, M. J.; Pankhurst, J. R.; Calle-Vallejo, F.; Buonsanti, R. Elucidating the Facet-Dependent Selectivity for CO_2 Electroreduction to Ethanol of Cu–Ag Tandem Catalysts. *ACS Catal.* **2021**, *11* (8), 4456–4463. https://doi.org/10.1021/acscatal.1c00420.
(166) De Gregorio, G. L.; Burdyny, T.; Loiudice, A.; Iyengar, P.; Smith, W. A.; Buonsanti, R. Facet-Dependent Selectivity of Cu Catalysts in Electrochemical CO_2 Reduction at Commercially Viable Current Densities. *ACS Catal.* **2020**, *10* (9), 4854–4862. https://doi.org/10.1021/acscatal.0c00297.
(167) Iyengar, P.; Huang, J.; De Gregorio, G. L.; Gadiyar, C.; Buonsanti, R. Size Dependent Selectivity of Cu Nano-Octahedra Catalysts for the Electrochemical Reduction of CO_2 to CH_4. *Chem. Commun.* **2019**, *55* (60), 8796–8799. https://doi.org/10.1039/C9CC02522G.
(168) Loiudice, A.; Lobaccaro, P.; Kamali, E. A.; Thao, T.; Huang, B. H.; Ager, J. W.; Buonsanti, R. Tailoring Copper Nanocrystals towards C_2 Products in Electrochemical CO_2 Reduction. *Angew. Chem. Int. Ed.* **2016**, *55* (19), 5789–5792. https://doi.org/10.1002/anie.201601582.

(169) Lu, Y.; Cao, H.; Xu, S.; Jia, C.; Zheng, G. A Comparative Study of the Effects of Different TiO_2 Supports toward CO_2 Electrochemical Reduction on CuO/TiO_2 Electrode. *RSC Adv.* **2021**, *11* (35), 21805–21812. https://doi.org/10.1039/D1RA02837E.
(170) Ren, D.; Gao, J.; Pan, L.; Wang, Z.; Luo, J.; Zakeeruddin, S. M.; Hagfeldt, A.; Grätzel, M. Atomic Layer Deposition of ZnO on CuO Enables Selective and Efficient Electroreduction of Carbon Dioxide to Liquid Fuels. *Angew. Chem. Int. Ed.* **2019**, *58* (42), 15036–15040. https://doi.org/10.1002/anie.201909610.
(171) Seeharaj, P.; Vittayakorn, N.; Morris, J.; Kim-Lohsoontorn, P. CeO_2 /CuO/TiO_2 Heterojunction Photocatalysts for Conversion of CO_2 to Ethanol. *Nanotechnology* **2021**, *32* (37), 375707. https://doi.org/10.1088/1361-6528/ac08be.
(172) Guzmán, H.; Roldán, D.; Sacco, A.; Castellino, M.; Fontana, M.; Russo, N.; Hernández, S. CuZnAl-Oxide Nanopyramidal Mesoporous Materials for the Electrocatalytic CO2 Reduction to Syngas: Tuning of H2/CO Ratio. *Nanomaterials* **2021**, *11* (11), 3052. https://doi.org/10.3390/nano11113052.
(173) Dongare, S.; Singh, N.; Bhunia, H.; Bajpai, P. K. Electrochemical Reduction of CO2 Using Oxide Based Cu and Zn Bimetallic Catalyst. *Electrochimica Acta* **2021**, *392*, 138988. https://doi.org/10.1016/j.electacta.2021.138988.
(174) Chen, C.; Yan, X.; Liu, S.; Wu, Y.; Wan, Q.; Sun, X.; Zhu, Q.; Liu, H.; Ma, J.; Zheng, L.; Wu, H.; Han, B. Highly Efficient Electroreduction of CO_2 to C2+ Alcohols on Heterogeneous Dual Active Sites. *Angew. Chem. Int. Ed.* **2020**, *59* (38), 16459–16464. https://doi.org/10.1002/anie.202006847.
(175) Pan, Z.; Han, E.; Zheng, J.; Lu, J.; Wang, X.; Yin, Y.; Waterhouse, G. I. N.; Wang, X.; Li, P. Highly Efficient Photoelectrocatalytic Reduction of CO2 to Methanol by a p–n Heterojunction CeO2/CuO/Cu Catalyst. *Nano-Micro Lett.* **2020**, *12* (1), 18. https://doi.org/10.1007/s40820-019-0354-1.
(176) Avgouropoulos, G.; Ioannides, T.; Matralis, H. Influence of the Preparation Method on the Performance of CuO–CeO2 Catalysts for the Selective Oxidation of CO. *Appl. Catal. B Environ.* **2005**, *56* (1–2), 87–93. https://doi.org/10.1016/j.apcatb.2004.07.017.
(177) Wang, X.; Klingan, K.; Klingenhof, M.; Möller, T.; Ferreira de Araújo, J.; Martens, I.; Bagger, A.; Jiang, S.; Rossmeisl, J.; Dau, H.; Strasser, P. Morphology and Mechanism of Highly Selective Cu(II) Oxide Nanosheet Catalysts for Carbon Dioxide Electroreduction. *Nat. Commun.* **2021**, *12* (1), 794. https://doi.org/10.1038/s41467-021-20961-7.
(178) Yuan, J.; Wang, Y. Photoelectrochemical Reduction of Carbon Dioxide to Methanol at CuS/CuO/$CuInS_2$ Thin Film Photocathodes. *J. Electrochem. Soc.* **2017**, *164* (13), E475–E479. https://doi.org/10.1149/2.1301713jes.
(179) Ma, M.; Djanashvili, K.; Smith, W. A. Selective Electrochemical Reduction of CO_2 to CO on CuO-Derived Cu Nanowires. *Phys. Chem. Chem. Phys.* **2015**, *17* (32), 20861–20867. https://doi.org/10.1039/C5CP03559G.
(180) Schreier, M.; Héroguel, F.; Steier, L.; Ahmad, S.; Luterbacher, J. S.; Mayer, M. T.; Luo, J.; Grätzel, M. Solar Conversion of CO2 to CO Using Earth-Abundant Electrocatalysts Prepared by Atomic Layer Modification of CuO. *Nat. Energy* **2017**, *2* (7), 17087. https://doi.org/10.1038/nenergy.2017.87.
(181) Li, P.; Xu, J.; Jing, H.; Wu, C.; Peng, H.; Lu, J.; Yin, H. Wedged N-Doped CuO with More Negative Conductive Band and Lower Overpotential for High Efficiency Photoelectric Converting CO2 to Methanol. *Appl. Catal. B Environ.* **2014**, *156–157*, 134–140. https://doi.org/10.1016/j.apcatb.2014.03.011.
(182) Le, M.; Ren, M.; Zhang, Z.; Sprunger, P. T.; Kurtz, R. L.; Flake, J. C. Electrochemical Reduction of CO2 to CH3OH at Copper Oxide Surfaces. *J. Electrochem. Soc.* **2011**, *158* (5), E45. https://doi.org/10.1149/1.3561636.
(183) Mandal, L.; Yang, K. R.; Motapothula, M. R.; Ren, D.; Lobaccaro, P.; Patra, A.; Sherburne, M.; Batista, V. S.; Yeo, B. S.; Ager, J. W.; Martin, J.; Venkatesan, T. Investigating the Role of Copper Oxide in Electrochemical CO_2 Reduction in Real Time. *ACS Appl. Mater. Interfaces* **2018**, *10* (10), 8574–8584. https://doi.org/10.1021/acsami.7b15418.

(184) Department of Environmental Science and Engineering, Beijing University of Chemical Technology, Beijing 100029, P. R. China; Yuan, J. Photoelectrochemical Reduction of Carbon Dioxide to Ethanol at Cu2O Foam Cathode. *Int. J. Electrochem. Sci.* **2017**, 8288–8294. https://doi.org/10.20964/2017.09.36.
(185) Yu, L.; Li, G.; Zhang, X.; Ba, X.; Shi, G.; Li, Y.; Wong, P. K.; Yu, J. C.; Yu, Y. Enhanced Activity and Stability of Carbon-Decorated Cuprous Oxide Mesoporous Nanorods for CO_2 Reduction in Artificial Photosynthesis. *ACS Catal.* **2016**, *6* (10), 6444–6454. https://doi.org/10.1021/acscatal.6b01455.
(186) Periasamy, A. P.; Ravindranath, R.; Senthil Kumar, S. M.; Wu, W.-P.; Jian, T.-R.; Chang, H.-T. Facet- and Structure-Dependent Catalytic Activity of Cuprous Oxide/Polypyrrole Particles towards the Efficient Reduction of Carbon Dioxide to Methanol. *Nanoscale* **2018**, *10* (25), 11869–11880. https://doi.org/10.1039/C8NR02117A.
(187) Li, J.-Y.; Yuan, L.; Li, S.-H.; Tang, Z.-R.; Xu, Y.-J. One-Dimensional Copper-Based Heterostructures toward Photo-Driven Reduction of CO2 to Sustainable Fuels and Feedstocks. *J. Mater. Chem. A* **2019**, *7* (15), 8676–8689. https://doi.org/10.1039/C8TA12427B.
(188) Christoforidis, K. C.; Fornasiero, P. Photocatalysis for Hydrogen Production and CO2 Reduction: The Case of Copper-Catalysts. *ChemCatChem* **2019**, *11* (1), 368–382. https://doi.org/10.1002/cctc.201801198.
(189) Shang, L.; Lv, X.; Shen, H.; Shao, Z.; Zheng, G. Selective Carbon Dioxide Electroreduction to Ethylene and Ethanol by Core-Shell Copper/Cuprous Oxide. *J. Colloid Interface Sci.* **2019**, *552*, 426–431. https://doi.org/10.1016/j.jcis.2019.05.073.
(190) Kang, H.-Y.; Nam, D.-H.; Yang, K. D.; Joo, W.; Kwak, H.; Kim, H.-H.; Hong, S.-H.; Nam, K. T.; Joo, Y.-C. Synthetic Mechanism Discovery of Monophase Cuprous Oxide for Record High Photoelectrochemical Conversion of CO_2 to Methanol in Water. *ACS Nano* **2018**, *12* (8), 8187–8196. https://doi.org/10.1021/acsnano.8b03293.
(191) Gao, F.; Liu, X.-J.; Zhang, J.-S.; Song, M.-Z.; Li, N. Photovoltaic Properties of the P-CuO/n-Si Heterojunction Prepared through Reactive Magnetron Sputtering. *J. Appl. Phys.* **2012**, *111* (8), 084507. https://doi.org/10.1063/1.4704382.
(192) Xu, X.; Zhang, M.; Feng, J.; Zhang, M. Shape-Controlled Synthesis of Single-Crystalline Cupric Oxide by Microwave Heating Using an Ionic Liquid. *Mater. Lett.* **2008**, *62* (17–18), 2787–2790. https://doi.org/10.1016/j.matlet.2008.01.046.
(193) Lee, Y. S.; Chua, D.; Brandt, R. E.; Siah, S. C.; Li, J. V.; Mailoa, J. P.; Lee, S. W.; Gordon, R. G.; Buonassisi, T. Atomic Layer Deposited Gallium Oxide Buffer Layer Enables 1.2 V Open-Circuit Voltage in Cuprous Oxide Solar Cells. *Adv. Mater.* **2014**, *26* (27), 4704–4710. https://doi.org/10.1002/adma.201401054.
(194) Asiri, A. M.; Gao, J.; Khan, S. B.; Alamry, K. A.; Marwani, H. M.; Khan, M. S. J.; Adeosun, W. A.; Zakeeruddin, S. M.; Ren, D.; Grätzel, M. Revisiting the Impact of Morphology and Oxidation State of Cu on CO_2 Reduction Using Electrochemical Flow Cell. *J. Phys. Chem. Lett.* **2022**, *13* (1), 345–351. https://doi.org/10.1021/acs.jpclett.1c03957.
(195) Yang, Y.; Xu, D.; Wu, Q.; Diao, P. Cu2O/CuO Bilayered Composite as a High-Efficiency Photocathode for Photoelectrochemical Hydrogen Evolution Reaction. *Sci. Rep.* **2016**, *6* (1), 35158. https://doi.org/10.1038/srep35158.
(196) Aguirre, M. E.; Zhou, R.; Eugene, A. J.; Guzman, M. I.; Grela, M. A. Cu2O/TiO2 Heterostructures for CO2 Reduction through a Direct Z-Scheme: Protecting Cu2O from Photocorrosion. *Appl. Catal. B Environ.* **2017**, *217*, 485–493. https://doi.org/10.1016/j.apcatb.2017.05.058.
(197) Yang, H.-J.; Yang, H.; Hong, Y.-H.; Zhang, P.-Y.; Wang, T.; Chen, L.-N.; Zhang, F.-Y.; Wu, Q.-H.; Tian, N.; Zhou, Z.-Y.; Sun, S.-G. Promoting Ethylene Selectivity from CO_2 Electroreduction on CuO Supported onto CO_2 Capture Materials. *ChemSusChem* **2018**, *11* (5), 881–887. https://doi.org/10.1002/cssc.201702338.
(198) Dias, E. H.; Da Silva, G. T. S. T.; Da Cruz, J. C.; Ribeiro, C. One-Pot Solvothermal Synthesis of Carbon Black-Supported CuO for Catalysis of CO_2 Electroreduction. *ChemElectroChem* **2022**, *9* (11). https://doi.org/10.1002/celc.202200206.

(199) Guzmán, H.; Roldán, D.; Sacco, A.; Castellino, M.; Fontana, M.; Russo, N.; Hernández, S. CuZnAl-Oxide Nanopyramidal Mesoporous Materials for the Electrocatalytic CO2 Reduction to Syngas: Tuning of H2/CO Ratio. *Nanomaterials* **2021**, *11* (11), 3052. https://doi.org/10.3390/nano11113052.
(200) Lu, Y.; Cao, H.; Xu, S.; Feng, W.; Hou, G.; Tang, Y.; Zhang, H.; Zheng, G. CO2 Photoelectroreduction with Enhanced Ethanol Selectivity by High Valence Rhenium-Doped Copper Oxide Composite Catalysts. *J. Colloid Interface Sci.* **2021**, *599*, 497–506. https://doi.org/10.1016/j.jcis.2021.04.087.
(201) Kosugi, T.; Kaneko, S. Novel Spray-Pyrolysis Deposition of Cuprous Oxide Thin Films. *J. Am. Ceram. Soc.* **1998**, *81* (12), 3117–3124. https://doi.org/10.1111/j.1151-2916.1998.tb02746.x.
(202) Pavan, M.; Rühle, S.; Ginsburg, A.; Keller, D. A.; Barad, H.-N.; Sberna, P. M.; Nunes, D.; Martins, R.; Anderson, A. Y.; Zaban, A.; Fortunato, E. TiO2/Cu2O All-Oxide Heterojunction Solar Cells Produced by Spray Pyrolysis. *Sol. Energy Mater. Sol. Cells* **2015**, *132*, 549–556. https://doi.org/10.1016/j.solmat.2014.10.005.
(203) Lee, Y. S.; Heo, J.; Winkler, M. T.; Siah, S. C.; Kim, S. B.; Gordon, R. G.; Buonassisi, T. Nitrogen-Doped Cuprous Oxide as a p-Type Hole-Transporting Layer in Thin-Film Solar Cells. *J. Mater. Chem. A* **2013**, *1* (48), 15416. https://doi.org/10.1039/c3ta13208k.
(204) Ye, F.; Zeng, J.-J.; Cai, X.-M.; Su, X.-Q.; Wang, B.; Wang, H.; Roy, V. A. L.; Tian, X.-Q.; Li, J.-W.; Zhang, D.-P.; Fan, P.; Zhang, J. Doping Cuprous Oxide with Fluorine and Its Band Gap Narrowing. *J. Alloys Compd.* **2017**, *721*, 64–69. https://doi.org/10.1016/j.jallcom.2017.05.272.
(205) Tanaka, H.; Shimakawa, T.; Miyata, T.; Sato, H.; Minami, T. Electrical and Optical Properties of TCO–Cu2O Heterojunction Devices. *Thin Solid Films* **2004**, *469–470*, 80–85. https://doi.org/10.1016/j.tsf.2004.06.180.
(206) Nair, M. T. S.; Guerrero, L.; Arenas, O. L.; Nair, P. K. Chemically Deposited Copper Oxide Thin Films: Structural, Optical and Electrical Characteristics. *Appl. Surf. Sci.* **1999**, *150* (1–4), 143–151. https://doi.org/10.1016/S0169-4332(99)00239-1.
(207) Haldar, R.; Reddy, S. K.; Suresh, V. M.; Mohapatra, S.; Balasubramanian, S.; Maji, T. K. Flexible and Rigid Amine-Functionalized Microporous Frameworks Based on Different Secondary Building Units: Supramolecular Isomerism, Selective CO_2 Capture, and Catalysis. *Chem. - Eur. J.* **2014**, *20* (15), 4347–4356. https://doi.org/10.1002/chem.201303610.
(208) Li, H.-P.; Li, S.-N.; Sun, H.-M.; Hu, M.-C.; Jiang, Y.-C.; Zhai, Q.-G. Tuning the CO_2 and C1/C2 Hydrocarbon Capture and Separation Performance for a Zn-F-Triazolate Framework through Functional Amine Groups. *Cryst. Growth Des.* **2018**, *18* (5), 3229–3235. https://doi.org/10.1021/acs.cgd.8b00389.
(209) Verma, A.; De, D.; Tomar, K.; Bharadwaj, P. K. An Amine Functionalized Metal–Organic Framework as an Effective Catalyst for Conversion of CO_2 and Biginelli Reactions. *Inorg. Chem.* **2017**, *56* (16), 9765–9771. https://doi.org/10.1021/acs.inorgchem.7b01286.
(210) Guo, Z.; Cheng, S.; Cometto, C.; Anxolabéhère-Mallart, E.; Ng, S.-M.; Ko, C.-C.; Liu, G.; Chen, L.; Robert, M.; Lau, T.-C. Highly Efficient and Selective Photocatalytic CO_2 Reduction by Iron and Cobalt Quaterpyridine Complexes. *J. Am. Chem. Soc.* **2016**, *138* (30), 9413–9416. https://doi.org/10.1021/jacs.6b06002.
(211) Leung, J. J.; Warnan, J.; Ly, K. H.; Heidary, N.; Nam, D. H.; Kuehnel, M. F.; Reisner, E. Solar-Driven Reduction of Aqueous CO2 with a Cobalt Bis(Terpyridine)-Based Photocathode. *Nat. Catal.* **2019**, *2* (4), 354–365. https://doi.org/10.1038/s41929-019-0254-2.
(212) Wang, W.; Zhang, J.; Wang, H.; Chen, L.; Bian, Z. Photocatalytic and Electrocatalytic Reduction of CO2 to Methanol by the Homogeneous Pyridine-Based Systems. *Appl. Catal. Gen.* **2016**, *520*, 1–6. https://doi.org/10.1016/j.apcata.2016.04.003.
(213) Bhanja, P.; Modak, A.; Bhaumik, A. Porous Organic Polymers for CO_2 Storage and Conversion Reactions. *ChemCatChem* **2019**, *11* (1), 244–257. https://doi.org/10.1002/cctc.201801046.
(214) Grammatico, D.; Marcasuzaa, P.; Viterisi, A.; Bousquet, A.; Su, B.-L.; Billon, L. Electrode-Modified Block Copoly-Ionic Liquid Boosting the CO_2 Reduction toward CO in Water-Based Media. *Chem. Commun.* **2023**, *59* (16), 2279–2282. https://doi.org/10.1039/D2CC06451K.

(215) Leibler, L. Theory of Microphase Separation in Block Copolymers. *Macromolecules* **1980**, *13* (6), 1602–1617. https://doi.org/10.1021/ma60078a047.
(216) Farrell, R.; Fitzgerald, T.; Borah, D.; Holmes, J.; Morris, M. Chemical Interactions and Their Role in the Microphase Separation of Block Copolymer Thin Films. *Int. J. Mol. Sci.* **2009**, *10* (9), 3671–3712. https://doi.org/10.3390/ijms10093671.
(217) Faustini, M.; Louis, B.; Albouy, P. A.; Kuemmel, M.; Grosso, D. Preparation of Sol–Gel Films by Dip-Coating in Extreme Conditions. *J. Phys. Chem. C* **2010**, *114* (17), 7637–7645. https://doi.org/10.1021/jp9114755.
(218) Satoh, M.; Yoda, E.; Hayashi, T.; Komiyama, J. Potentiometric Titration of Poly(Viny1pyridines) and Hydrophobic Interaction in the Counterion Binding. **1989**, *22* (4).

Annex A - Supplementary Information of Chapter 3

Experimental Section

Materials

Indium thin oxide (ITO)-coated glass substrates with 15Ω were acquired from Xinyan technology Ltd. The copper (II) nitrate ($Cu(NO_3)_2.3H_2O$), Zinc nitrate ($Zn(NO_3)_2.6H_2O$), Cerium (III) nitrate, ($Ce(NO_3)_2.6H_2O$), Silver nitrate ($AgNO_3$) and hydroxypropyl cellulose (Mw ~370,000) were purchase from Sigma-Aldrich and used without further purification.

Substrate Cleaning

The glass-ITO substrates were cleaned in various ultra-sonic baths of 15 min each, being a bath in milli-q water, the second in acetone and the final one in isopropanol. After this cleaning, the substrates are subjected to a UV-ozone 30 minutes treatment right before being used.

Electrodes fabrication via blade coating

Preparation of a solution of DMF and hydroxypropyl cellulose (iPrcel) (best results were shown for 1.396g of iPrcel for 25 ml of DMF in previous studies). The solution was stirred until it reached homogeneity and then $Cu(NO_3)_2$ was dissolved on a small volume of the previous solution, with a concentration of 60 mg/ml. This solution was drop cast onto the ITO substrate using the doctor blade methodology. The films obtained were dried at 80ºC after a small amount of the film was removed from the substrate using DMF in order to have a contact in the electrode. Lastly, the films were annealed at 500ºC for 1 hour, with a slow heating ramp (2 ºC/min) under either air or N_2 atmosphere.

Table A 1 shows the optimum parameters found for the formation of the Cu_xO films. Many iterations of these parameters were tested, and the ones shown have wielded the best results with a high degree of reproducibility. Height of the

blade was tested from 50 to 500 µm, the concentration of hydroxypropyl cellulose was tested in a range from 50 to 100 mg/ml$_{DMF}$ while the amount of $Cu(NO_3)_2.3H_2O$ ranged from 20 to 100 mg/ml$_{DMF}$.

***Table A 1**. Optimised parameters used on the formation of the $Cu(NO_3)_2$ films*

Film	Hydroxypropyl cellulose concentration (mg/ml$_{DMF}$)	$Cu(NO_3)_2.3H_2O$ concentration (mg/ml$_{DMF}$)	Metal dopant wt percentage (%)	Blade Height (µm)	Deposition Temperature (°C)	Annealing Temperature (°C)
Cu_xO	70	60	-	250	70	500
Cu_xO-CeO_2	70	60	2.5/5/7.5/10	250	70	500
Cu_xO-ZnO	70	60	2.5/5/7.5/10	250	70	500
Cu_xO-AgO	70	60	2.5/5/7.5/10	250	70	500

Characterization

Surface Analysis

SEM was conducted with a Hirox SH-3000 microscope with an accelerated voltage of 25kV. A thin layer of gold was deposited on top of the samples to assure their conductivity.

SEM-AES analysis was done using a JEOL JAMP 9500 F Auger spectrometer (JEOL Ltd, Tokyo, Japan) equipped with a Schottky Field Emission gun and a hemi-spherical analyser coupled with a high dynamic multichannel detector. Notably, Auger spatial resolution is about 10-30 nm with a probing depth of about 2-7 nm in the applied analysis conditions. The typical operating pressure was $<2 \times 10^{-7}$ Pa while analysis was performed at 30-60° tilt to prevent any charging effect. Wide AES survey spectra was recorded between 15-2400 eV KE (kinetic energy) with 1 eV step size and a variable dwell time to reach adapted signal to noise ratio. The acquisition mode is CRR (Constant relative resolution) using a relative energy resolution dE/E =

0.5% (low resolution /high sensitivity) or dE/E = 0.1% (high-energy resolution for chemical state analysis) over the kinetic energy range. Auger spectra are obtainable using the EN(E) mode (expressed as the output signal of the electron detector using "true" pulse counting versus kinetic energy) or using dN(E)/dE representation (spectra are differentiated numerically).

Qualitative AES analysis uses peak position and shape regarding to Hanbooks or Jeol data base for elemental identification. Semi quantitative analysis uses peak-to-peak intensity from derivative mode and relative sensitivity factors (elemental RSF) for calculation (expressed in atomic percent). Chemical sate analysis is performed using Jeol "spectra investigator" software for "peak deconvolution" using reference's Jeol data base.

Photoelectron Spectrometry (XPS) measurements were performed on a Thermo K-alpha spectrometer with a 120 mm mean radius Hemispherical Analyzer (HAS) and a microfocussed monochromated radiation (Al Ka,1486.6 eV, microspot continuously variable from 30 to 400 μm diameter) operating under UHV conditions (residual pressure of 1 x 10^{-9} mbar). The X-ray power was functioning at 72 W (12 kV, 6 mA) for a typical 400 μm beam diameter. The spectra were recorded in the constant Pass Energy (PE) mode CAE, both for wide high sensitivity survey spectra (PE = 200 eV) and high energy resolution analyses (PE = 20 eV) for quantitatively resolved chemical analyses. A charge neutralization system was used (low energy electrons) to compensate for charge effects. Spectra were mathematically fitted with Casa XPS software using a least squares algorithm and a non-linear baseline. The fitting peaks of the experimental curves were performed by a combination of Gaussian (70 %) and Lorentzian (30%) distributions. Only core level spectra for the elements with highest photoionization cross section were recorded in order to extract more reliable information.

XRD characterization was executed on a Bruker D2 Phaser powder diffractometer with a Cu Kα radiation source with a wavelength of 1.5406 Å. XRD patterns were recorded in a 10° to 80° 2θ with a 0.021 step and a 0.05 s counting time per step. DIFFRAC.EVA software was used to identify the phases and crystallite sizes.

UV-Vis-NIR absorption spectra were recorded with a double-beam Cary 5000 UV-Vis-NIR spectrophotometer in steps of 200 nm in the range 300–1500 nm using a 0.1 cm thick quartz substrate.

Conductivity measurements were conducted in the 4-probe methodology with a Keithley 6430 Sub-Femtoamp Remote SourceMeter SMU instrument which had a current source between 0.5 fA to 0.105 A and voltage range of 200 µV to 211 V.

Constant potential chronoamperometry

All of electrochemical tests were performed in a 3-electrode single chamber cell with the anode, a platinum wire, contained in a bridge tube. The cell was filled with 40 mL of 0.1 M $KHCO_3$ aqueous solution as electrolyte. The reference electrode was a Ag/AgCl electrode (saturated KCl solution). The pH value of the CO_2 saturated electrolyte was measured to be 6.8. All potentials cited in this work refers versus the Ag/AgCl. The potentials were converted to RHE, according to **Equation A 1**. The overpotential (η) was calculated according to **Equation A 2**[7]. Before constant potential chronoamperometry experiments, the electrolyte was purged with N_2 or CO_2 for 15 min under stirring to exclude air in the solution. A potentiostat PGSTAT 204, regulated via the Metroohm Autolab software, was used to perform the electrochemical testing.

$$E\ (RHE) = E\ (Ag/AgCl) + 0.059 * pH + E_0(Ag/AgCl)$$

Equation A 1

$$\eta = E - E^0$$

Equation A 2

Permanent gases quantification

H_2 and CO were identified and quantified using gas chromatography (GCMS-QP2010-plus, Shimadzu, Japan) equipped with a packed column (ShinCarbon ST, 2m; 0.53 mm, mesh80/100, Restek, USA) for permanent gases separation. Helium (6.0, Alphagaz 2, AirLiquide) was used as carrier gas. A Dielectric-Barrier Discharge Ionisation Detector (BID, Shimadzu) was used to quantify all permanent gases (H_2, CO, Methane, Ethane, ethylene). Sampling from the electrolysis cell's head space was carried *via* proprietary automated-sampling system operating solenoid valves at

timed intervals transferring a sample of the cell's head space to a GC-sample loop (500 uL) followed by the subsequent injection to the GC column.

Quantification of H_2 and CO was carried out by comparison with an external standard calibration curve. The calibration curve was drawn from sampling the head space of the electrolysis cell held in identical conditions of volume (liquid electrolyte) and pressure (head space) containing known molar amounts of standard gases.

Results

Electrochemical behaviour

Figure A 2 *to* ***Figure A 5*** *show the electrochemical behaviour of the Cu_xO in N_2 and CO_2 atmospheres via the linear sweep voltammetry (LSV) characterization technique. The LSVs were performed from 0.6 to -0.8V vs RHE with a sweep of 50 mV/sec. The LSVs were performed at this range mentioned due to the limits of ITO as a substrate, which undergoes reduction at -0.9V vs RHE, changing from a transparent film to a metallic coloured one.*

Figure A 1 shows a cyclovoltammetry (CV) of a blank ITO realised in a saturated Argon atmosphere from 1.6 to -0.75V vs RHE at a scan speed of 100 mV/s. In the LSVs, It is observed little different on current from a N_2 and a CO_2 atmosphere, which could indicate poor activity towards CO_2 reduction or that the hydrogen evolution and the CO_2 reduction are in competition. The delamination the electrodes suffer under electrochemical condition is shown in **Figure A 6**.

In an attempt to avoid the delamination of the film, a thin layer of titanium dioxide (TiO_2) was spin coated at 4000 rpm for 45 seconds in between the ITO and the copper film. This layer was deposited in 3 thickness (20, 50 and 100 nm) and CVs and catalysis were performed on ITO/TiO_2/CuO electrodes, with only a slight improvement on stability (delamination occurring a few minutes later on electrochemical conditions) and showing over 90% hydrogen production. **Figure A 7** shows the CVs of ITO/CuO and ITO/TiO_2/CuO with the different TiO_2 thicknesses. Since no significant change was brought by the addition of TiO_2, the study was not continued.

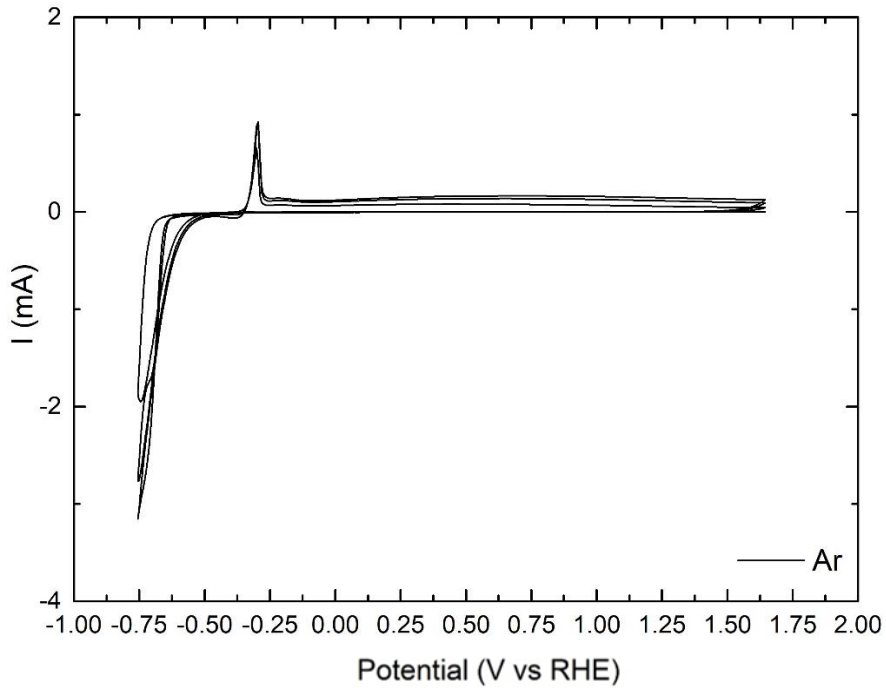

Figure A 1. *CV of a ITO substrate under Argon.*

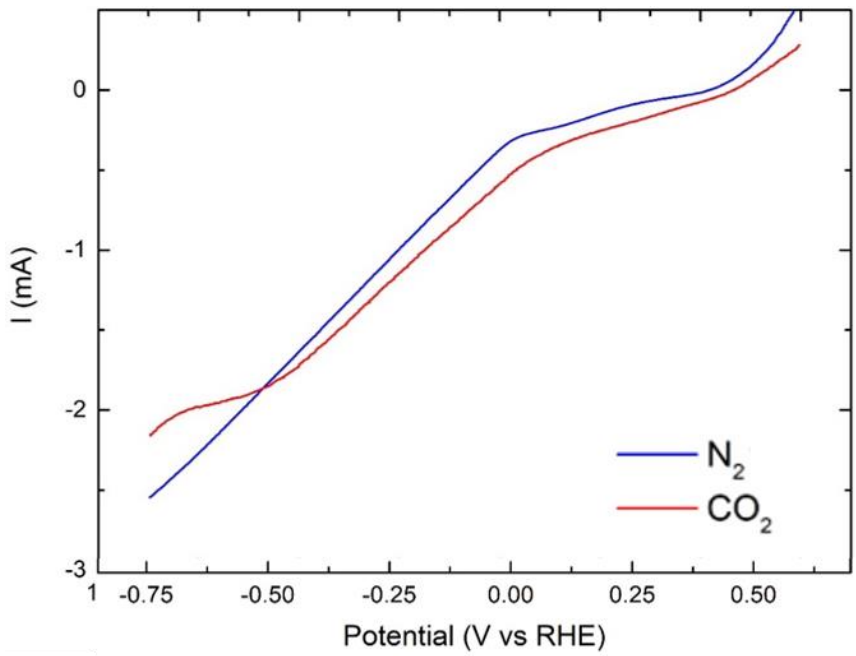

Figure A 2. *LSV of CuO under N_2 (blue) and CO_2 (red).*

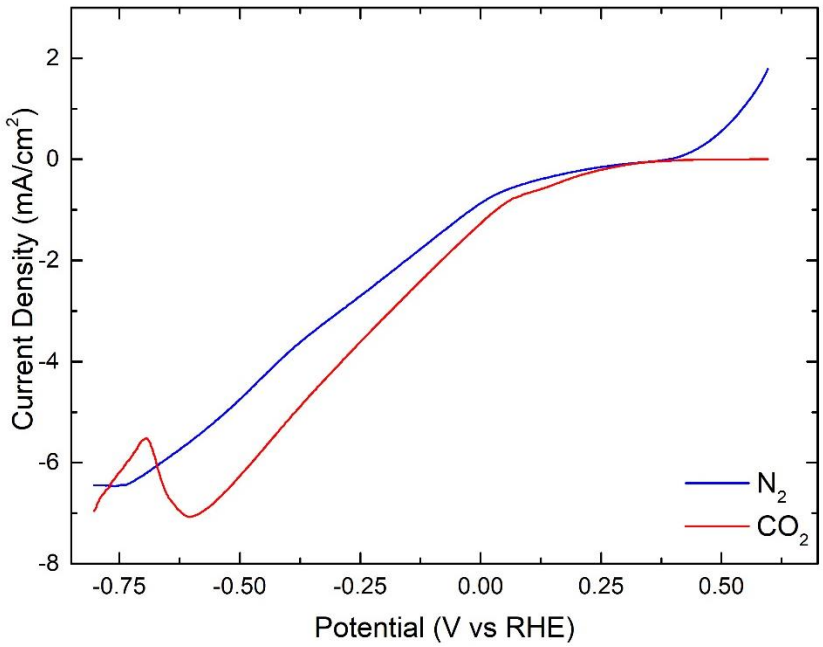

Figure A 3. *LSV of Cu_2O 40 ml/min N_2 under N_2 (red) and CO_2 (blue).*

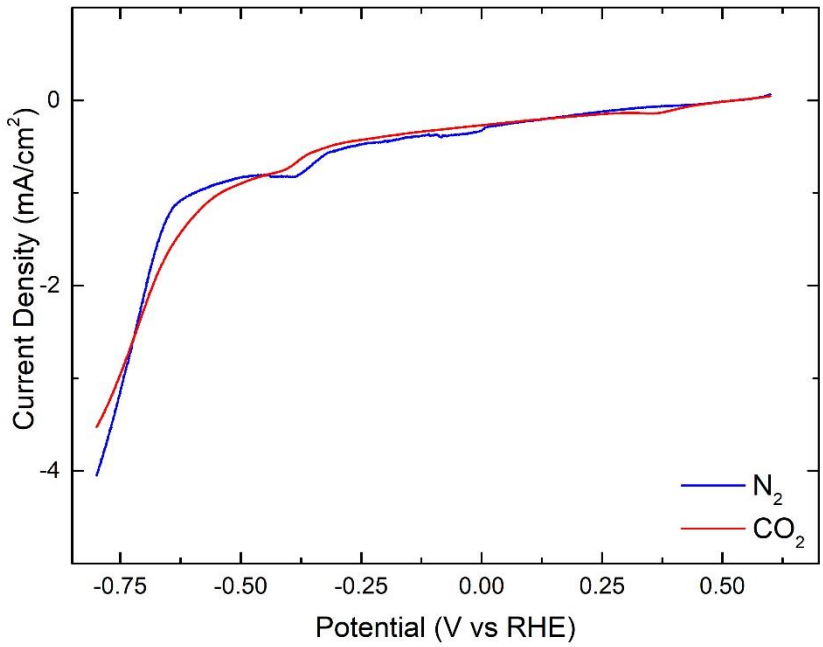

Figure A 4. *LSV of Cu_2O 60 ml/min N_2 under N_2 (red) and CO_2 (blue).*

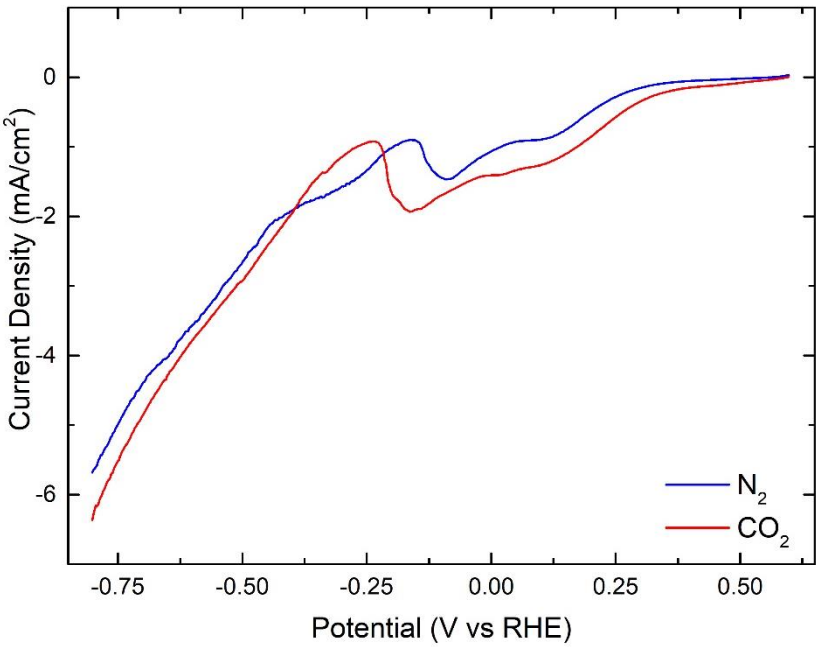

Figure A 5. *LSV of Cu_2O 80 ml/min N_2 under N_2 (red) and CO_2 (blue).*

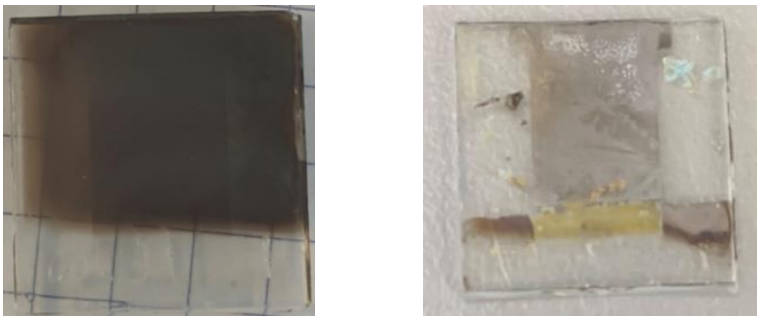

Figure A 6. *CuO electrode before (left) and after (right) a linear sweep voltammetry.*

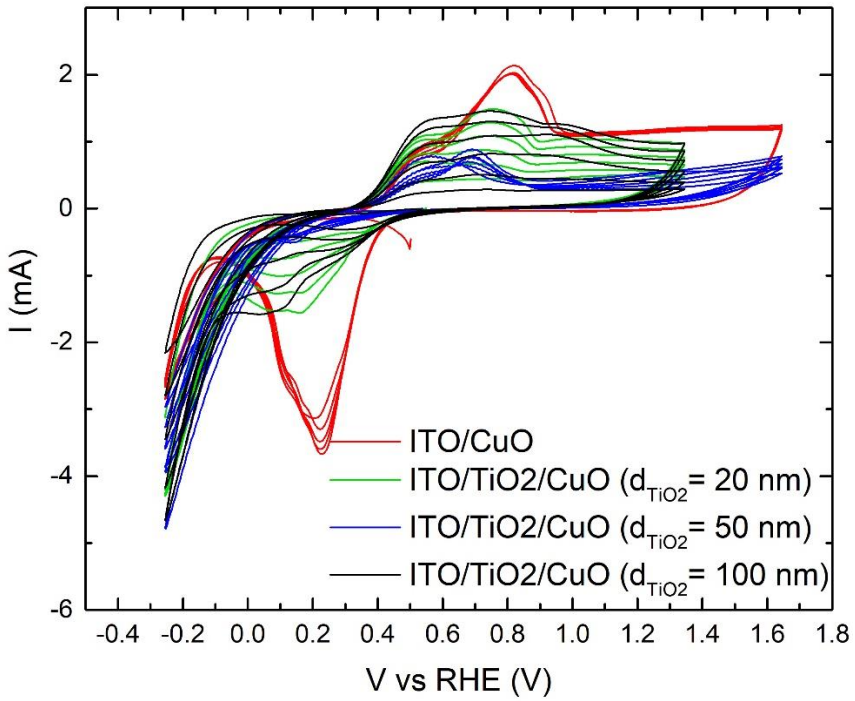

Figure A 7. *CVs of CuO films on a ITO substrate with increasing amount of TiO_2 between the substrate and the metallic oxide.*

UV-Visible Characterization

In order to determine the optical bandgap of the four oxides, the Tauc method was used, plotting the right side of the Tauc equation (**Equation A 3**), where A is a constant known as the band tailing parameter, E_g is the optical bandgap, α is the absorption coefficient and hv is the photon energy, against hv (**Figure A 8.** Tauc plot of CuO. to **Figure A 11**). The band gap was then obtained by calculating the point in which the tangent of the first linear region of the plot crosses the x axis[141].

$$(\alpha h\nu)^2 = A(h\nu - E_g)$$

Equation A 3 – Tauc equation.

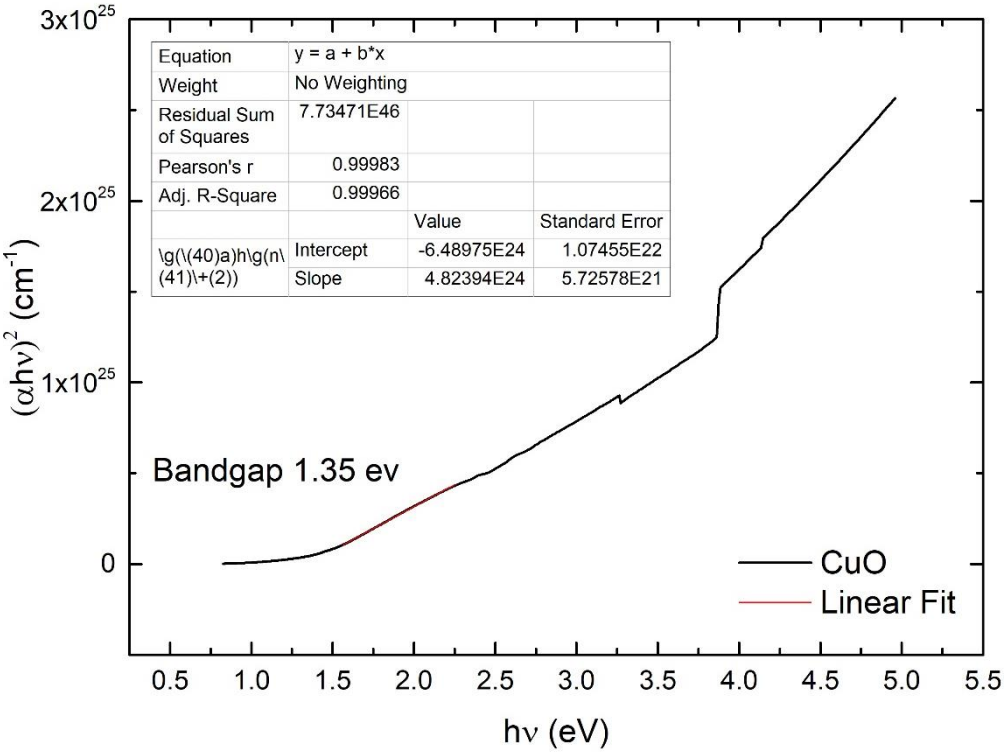

Figure A 8. *Tauc plot of CuO.*

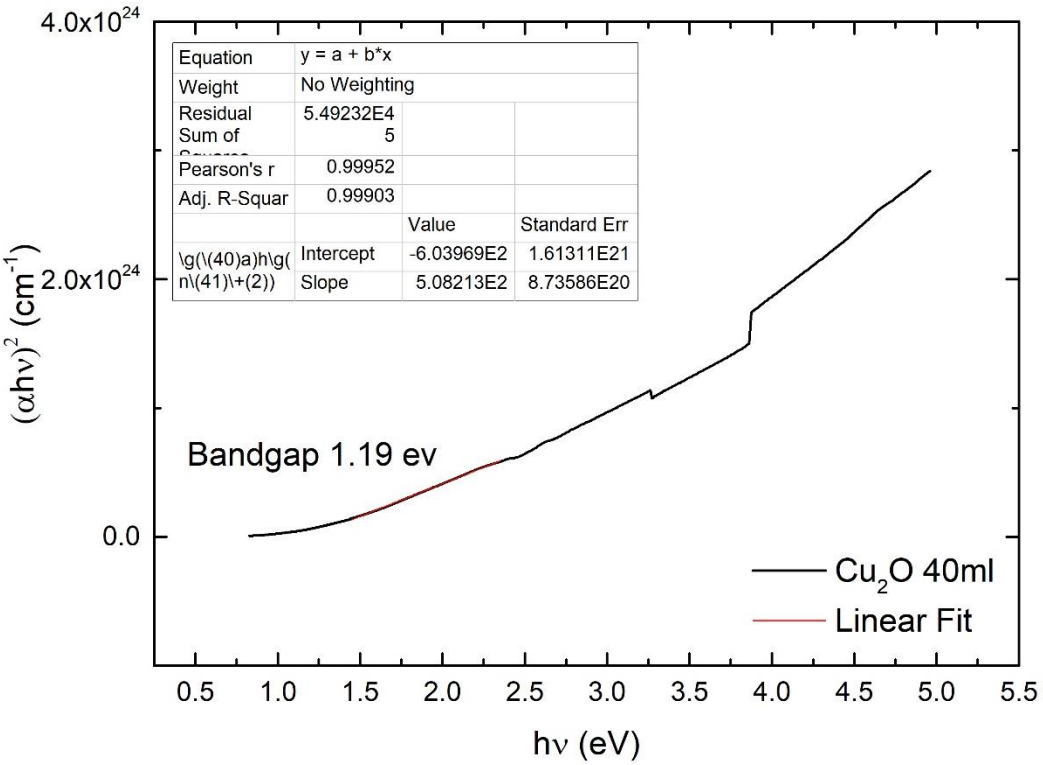

Figure A 9. *Tauc plot for Cu_2O 40 ml/min.*

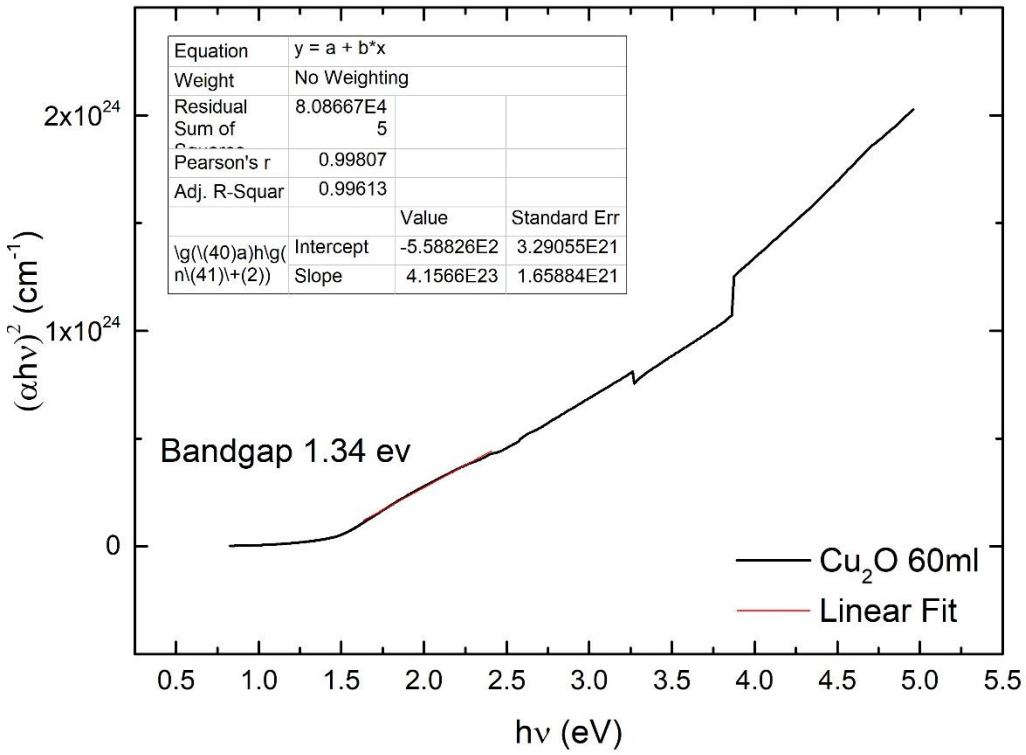

Figure A 10. *Tauc plot for Cu_2O 60 ml/min.*

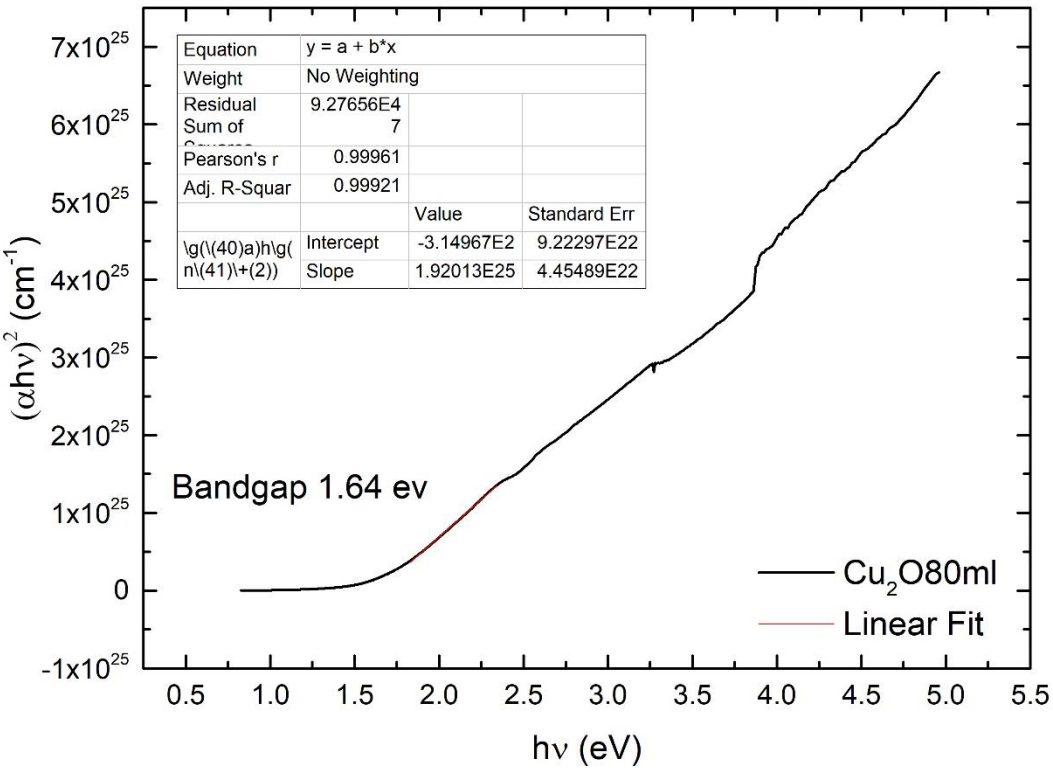

Figure A 11. *Tauc plot for Cu_2O 80 ml/min.*

Conductivity measurement of ITO

Alongside the copper-based films, the conductivity of the ITO as a substrate was also measured, before and after the ITO was exposed to the calcination conditions of the copper oxide (500º C for 1h). The results are presented in **Table A 2**.

***Table A 2**. Conductivity of the ITO substrate before and after calcination at 500º C.*

	Conductivity (S/m)
ITO	44500
Calcined ITO	6302

Annex B - Supplementary Information of Chapter 4

Experimental Section

Materials

Styrene (S ≥ 99 %), Methyl methacrylate and 4VP were purchased from Sigma Aldrich. The BlocBuilder© alkoxyamine (2-methylaminoxypropionic-SG1) That was used as the initiator was kindly provided by Arkema. Methanol, THF, DMF and Chloroform were purchased from Sigma Aldrich. All products where used as received.

Polymer formation

Firstly, a PMMA with 5% PS statistical copolymer was synthesised via bulk polymerization. In a round bottom flask, styrene and MMA were mixed with the initiator with a weight ratio of MMA:Sty:Iniator of 20:2.3:0.140. The flask was sealed using a septum and degassed with nitrogen for 20 minutes. The polymerization was carried out at 90ºC for 3 hours and 30 minutes in an oil bath and then stopped by cooling the flask with water and opening it to the air. The copolymer was isolated by precipitating it in methanol, filtering it and drying it in a vacuum oven.

After, to form the PMMA-*b*-P4VP block copolymer, another bulk polymerization was done, mixing the PMMA fabricated before with 4VP and DMF in a round bottom flask in a weight ratio PMMA:4VP:DMF of 1.15:1:1. The flask was sealed using a septum and degassed with nitrogen for 20 minutes. The polymerization was carried out at 110ºC for 2 hours and 30 minutes in an oil bath and then stopped by cooling the flask with water and opening it to the air. The copolymer was isolated by precipitating it in methanol, filtering it and drying it in a vacuum oven. This final copolymer was characterised by 1H NMR and SEC in THF for determination of its composition.

Honeycomb film formation

Using the breath figure method, honeycomb films were achieved. The copolymer was dissolved in chloroform and drop-casted on the substrate inside of a

hermetically sealed chamber with a controlled humid atmosphere (humidity above 80%). Honeycomb film porosity was changed by changing the concentration of copolymer in solution.

Dip coating deposition

Silver foil substrates were dip coated on a solution of 1% wt of the PMMA-*b*-P4VP copolymer in dichloromethane. The coating thickness was controlled by the withdraw speed of the substrate from the solution. The withdraw speed use was of 10, 100, 500 and a 1000 µm/s to obtain a theoretical thickness of 7, 22, 49 and 100 nm, respectively. **Equation B 1** shows how the theoretical thickness (h_0) was calculated, based on the viscosity (η) and density (ρ) of the solution, on the rate of withdraw (U_0), on the gravitational constant (g) and on the dynamic meniscus curvature, represented by the constant c[217].

$$h_0 = c\left(\frac{\eta U_0}{\rho g}\right)^{\frac{1}{2}}$$

Equation B 1

Characterization

Surface Analysis

AFM imaging was done using a MultiMode 8 Atomic Force Microscope from Bruker in a PeakForce QNM (Quantitative NanoMechanics) mode.

Optical microscopy pictures were taken using a DMLM microscope (LEICA©) equipped with DFC280 camera. Scanning electron microscopy (SEM) images were taken using a Hirox© SH-3000 device.

SEM was conducted with a Hirox SH-3000 microscope with an accelerated voltage of 25kV. A thin layer of gold was deposited on top of the samples to assure their conductivity.

Polymer Characterization

SEC was performed using THF as eluent (flow rate 1.0 mL min−1) at 30 °C. The SEC is equipped with a Viscotek VE 5200 automatic injector, a precolumn and two columns (Styragels HR 5E and 4E (7.8 ft, 300 mm)) and 4 detectors: UV−visible spectrophotometer (Viscotek VE 3210), a Multiangle Light Scattering detector (Wyatt

Heleos II), a viscosimeter (Wyatt Viscostar II) and a refractive index detector (Viscotek VE 3580). Polystyrene standards were used to determine the dispersity of the polymers.

^{1}H NMR characterisation was performed on a Bruker AVANCE 400 MHz using $CDCl_3$ as a solvent at 25ºC.

Results

Optical Imaging

Figure B 1 to **Figure B 6** show the surface morphology and the porosity of the PMMA-*b*-P4VP honeycomb films performed with different copolymer dissolution in chloroform. It is observed, as described in **Chapter 3**, that for 2.5 and 10 mg/ml, the porosity is not uniform at all and then it shows great uniformity at 6 mg/ml and 7mg/ml.

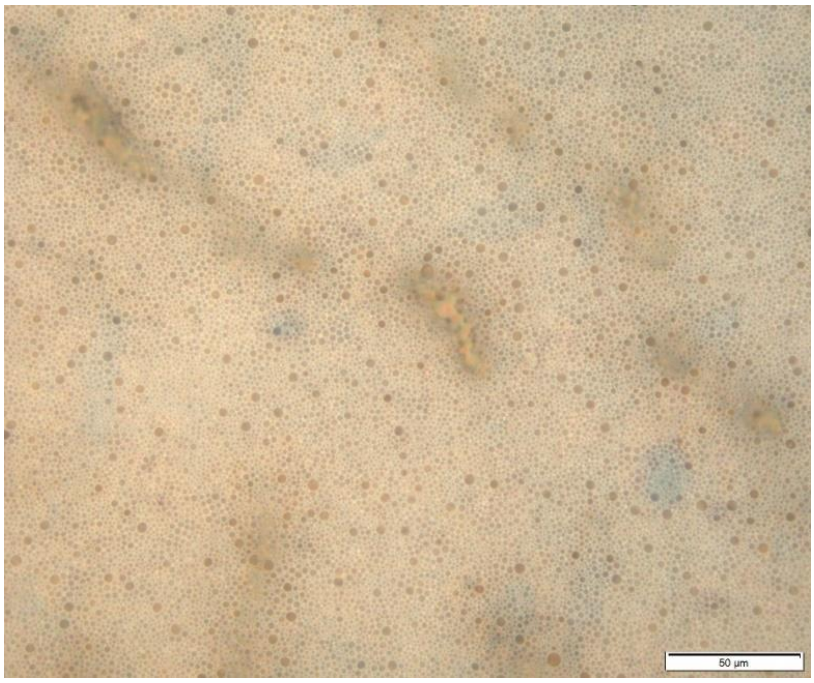

Figure B 1. *Optical imaging of PMMA-b-P4VP prepared from a 2.5 mg/ml concentration in chloroform.*

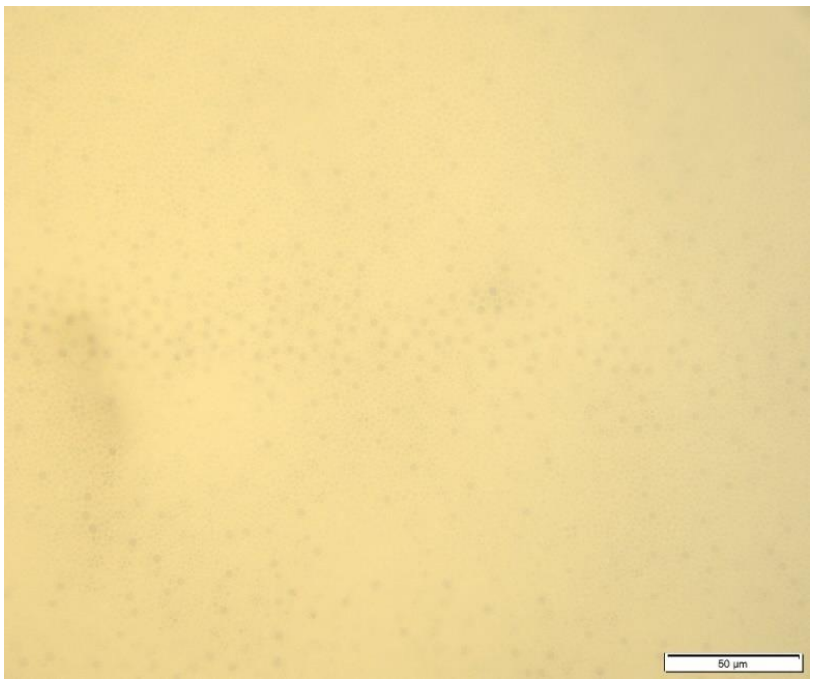

Figure B 2. *Optical imaging of PMMA-b-P4VP prepared from a 2.5 mg/ml concentration in chloroform.*

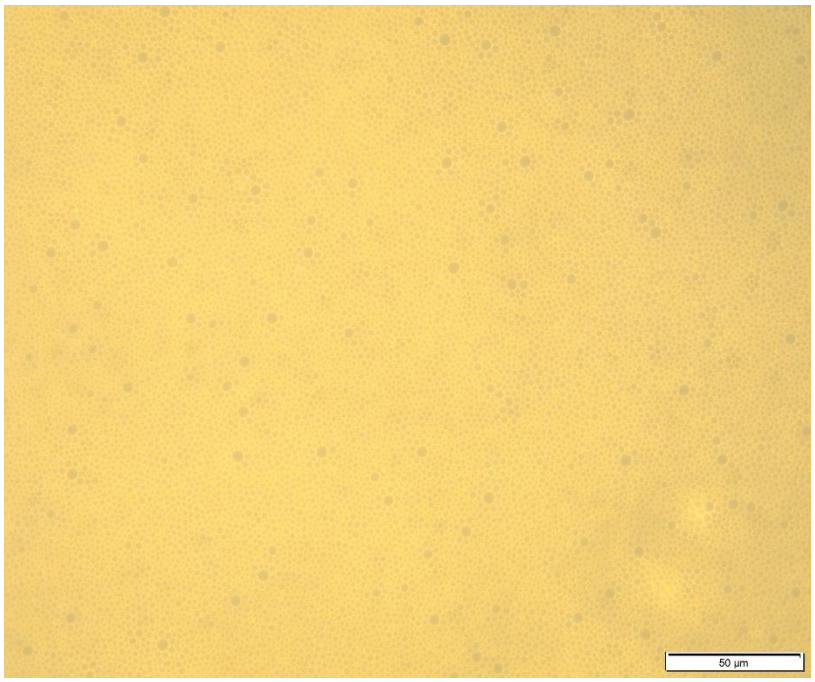

Figure B 3. *Optical imaging of PMMA- b-P4VP prepared from a 5 mg/ml concentration in chloroform.*

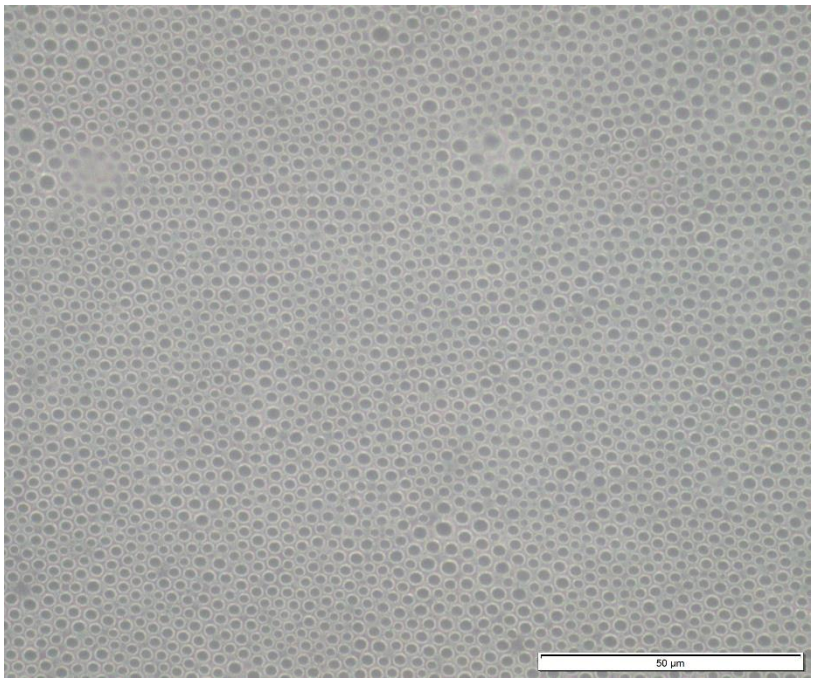

Figure B 4.*Optical imaging of PMMA-b-P4VP prepared from a 6 mg/ml concentration in chloroform.*

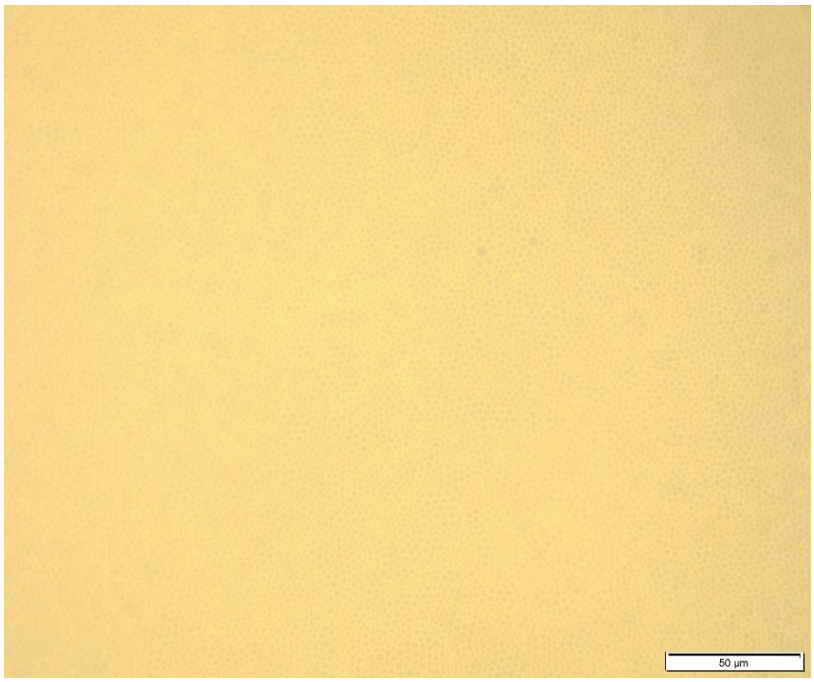

Figure B 5.*Optical imaging of PMMA-b-P4VP prepared from a 7 mg/ml concentration in chloroform.*

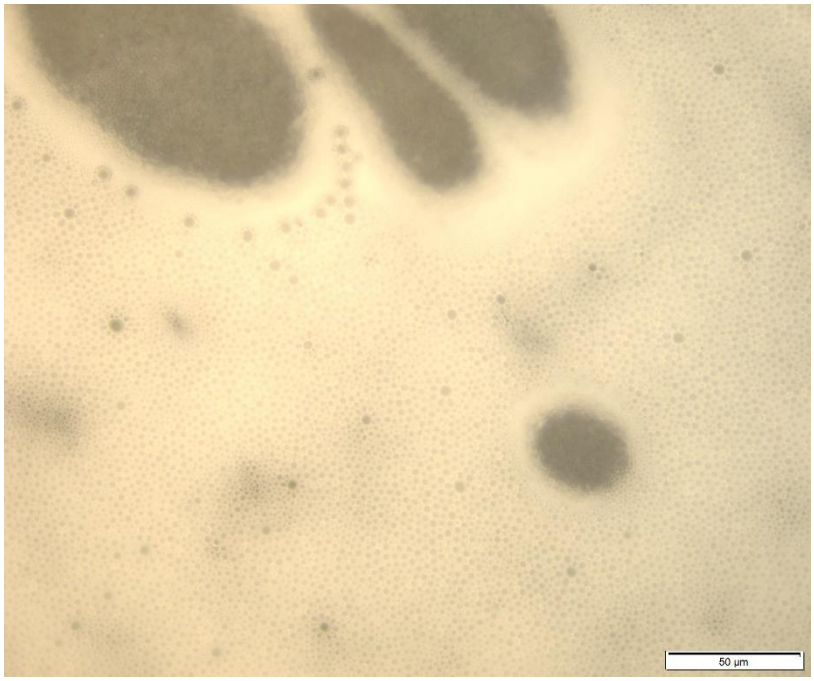

Figure B 6.*Optical imaging of PMMA-b-P4VP prepared from a 10 mg/ml concentration in chloroform.*

Contact Angle measurements

Figure B 7 to **Figure B 12** show the contact angles for different honeycomb films and the change of contact angle with the change of pH. The change in contact angle at pH 2 is due to the protonation of the 4VP chains, causing them to became hydrophilic. Since the pKa of 4VP is around pH 3.5-4.5[218], the droplet at around that pH has a higher contact angle that the one at pH 2 although not as high as the water droplets due to some partial protonation.

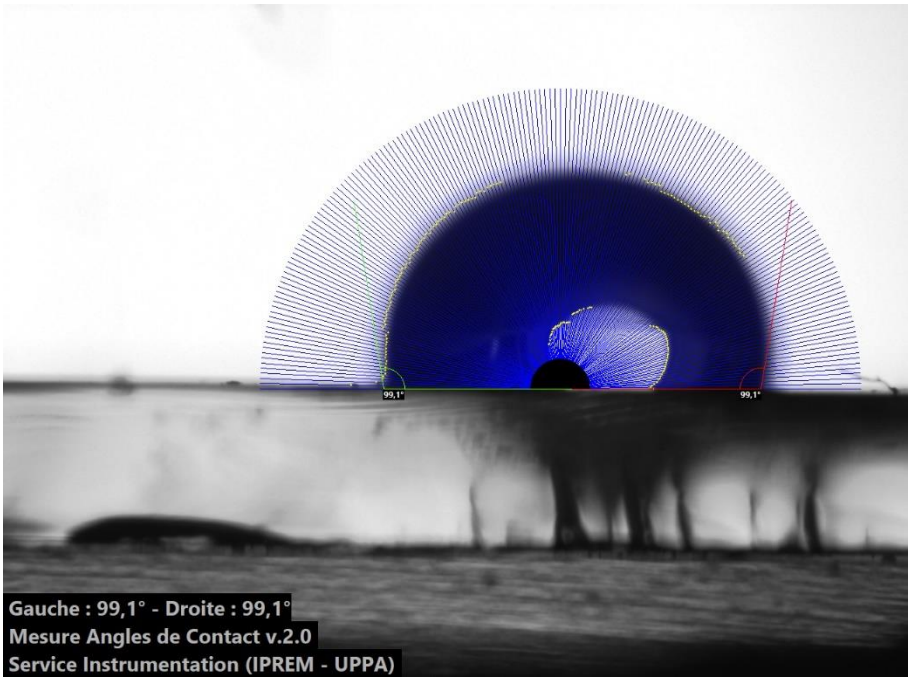

Figure B 7.*Contact angle of PMMA-b-P4VP from a 5 mg/ml concentration in chloroform.*

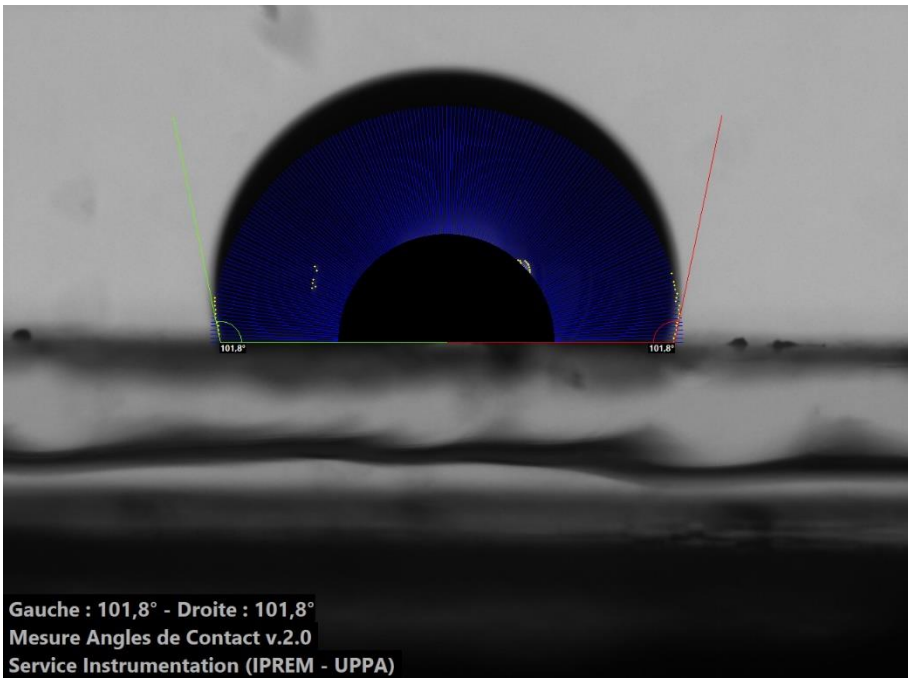

Figure B 8.*Contact angle of PMMA-b-P4VP from a 6 mg/ml concentration in chloroform.*

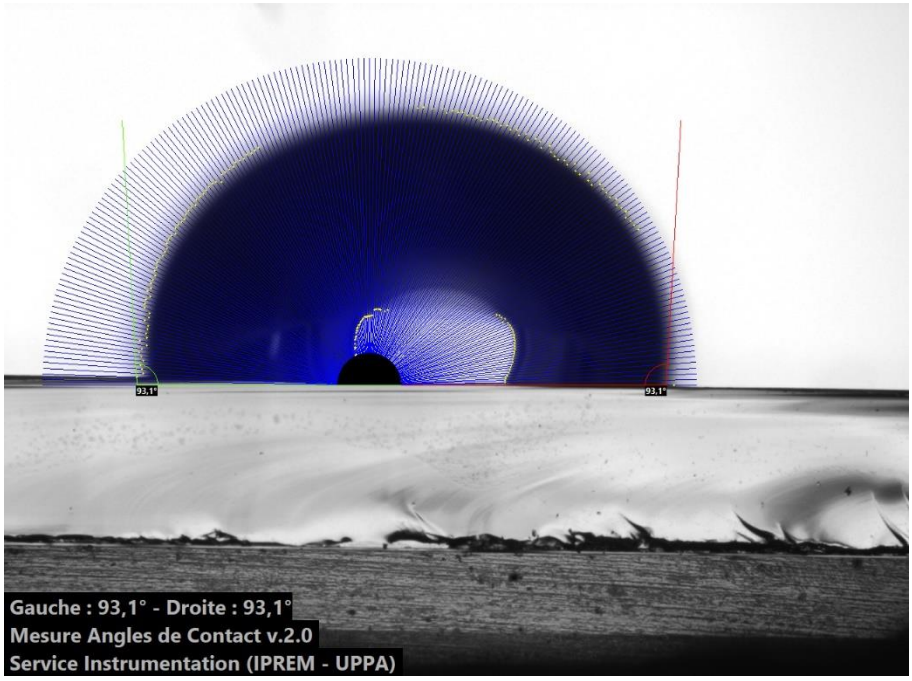

Figure B 9.*Contact angle of PMMA-b-P4VP from a 7 mg/ml concentration in chloroform.*

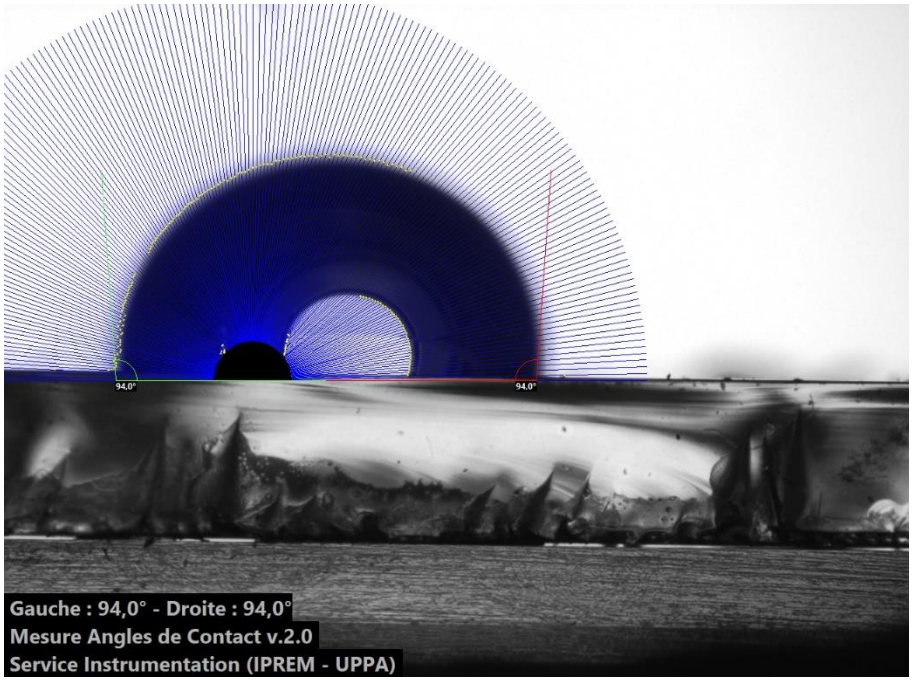

Figure B 10.*Contact angle of PMMA-b-P4VP from a 8 mg/ml concentration in chloroform.*

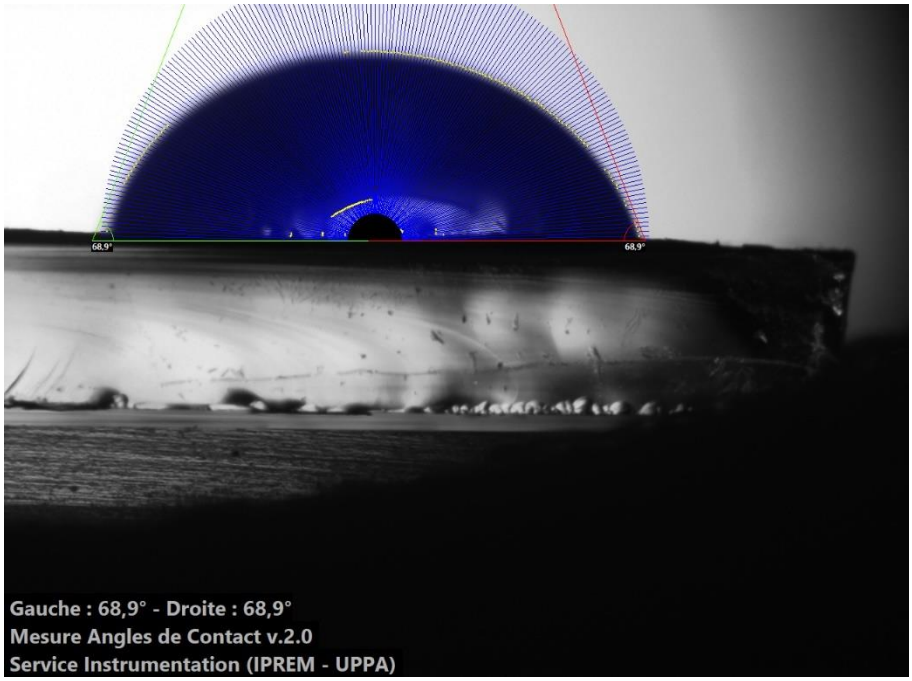

Figure B 11. *Contact angle of PMMA-b-P4VP from a 6 mg/ml concentration in chloroform with a drop of pH 2 potassium buffer solution.*

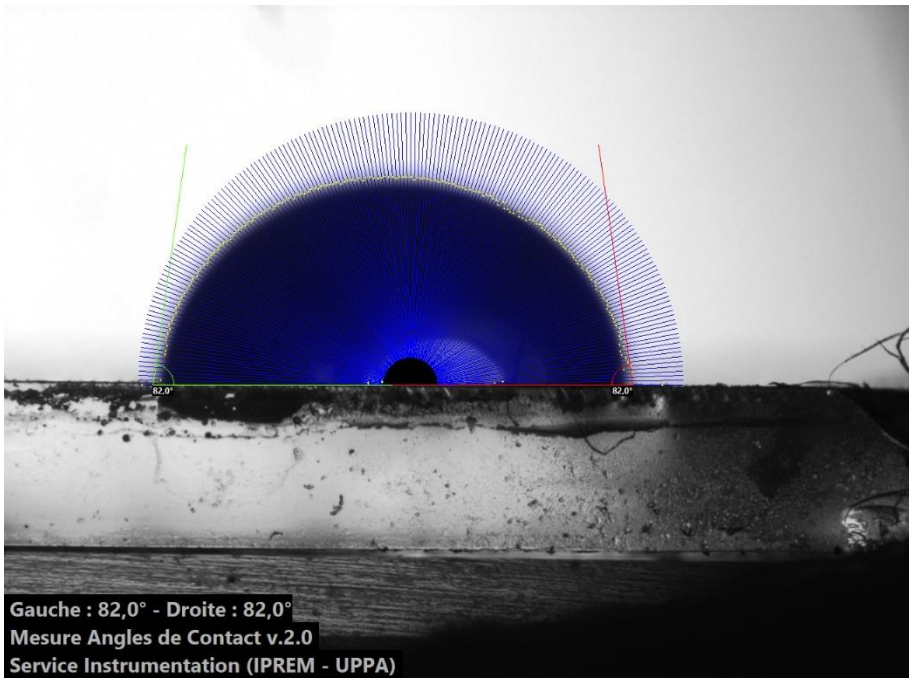

Figure B 12. *Contact angle of PMMA-b-P4VP from a 6 mg/ml concentration in chloroform with a drop of pH 4.14 potassium buffer solution.*

ECOLE DOCTORALE :
École doctorale sciences exactes et leurs applications

LABORATOIRE :
IPREM

CONTACT
(à personnaliser s'il y a lieu)